Centre for Natural Gas
16 March 2022

THE UNIVERSITY OF QUEENSLAND
AUSTRALIA
CREATE CHANGE

Testing the Surat Basin two deposition centre hypothesis: Part A Zircon geochronology

Final report

ANLEC project 7-0320-C326

Kasia Sobczak[1]
Andrew La Croix[2]
Joan Esterle[3]
Phil Hayes[1]
Heinz-Gerd Holl[1]

[1] Centre for Natural Gas, University of Queensland, Brisbane, Qld 4072, Australia
[2] School of Science, University of Waikato, Hamilton 3240, New Zealand
[3] School of Earth and Environmental Sciences, University of Queensland, Brisbane, Qld 4072, Australia

Executive Summary

Carbon capture and storage (CCS) may play an important role in the reduction of atmospheric CO_2 from industrial emissions, within which geological storage is a key technical component requiring detailed subsurface understanding. The Precipice Sandstone in the southern Surat Basin of southeast Queensland is a prime candidate storage reservoir for CCS but gaps in knowledge remain about its geological history, which in part controls the physical and chemical characteristics of the rocks and has implications for safe effective storage. Development of CCS requires demonstration that geological sequestration will be both effective and safe, which in turn needs in-depth knowledge of the characteristics and variability of reservoir and seal rocks.

Presently, the majority of what we know about the Precipice Sandstone is based on wells and outcrop from the northern part of the Surat Basin. In the southern Surat Basin where CCS exploration and development potential is greatest, for example in the Greenhouse Gas Exploration permit EPQ10, our knowledge of the geology is significantly less due to greater burial depth and fewer wells. It has yet to be determined if geological and petrophysical characterization completed in the northern basin is applicable to the south, which required further research to understand Precipice Sandstone deposition and the geochronology of marker horizons.

An important outcome of a recent study of the Precipice Sandstone to Evergreen Formation stratigraphic interval undertaken by the UQ-SDAAP project (2019) was the hypothesis that the Precipice Sandstone may represent a composite sedimentary system fed by multiple source terranes depositing sediment into two depocentres – one in the north and one in the south. The implications of this hypothesis would be that the work done in the EPQ7 tenement (northern sub-basin) may be of limited application to understanding the EPQ10 tenement (southern sub-basin) as they may consist of strata with differing petrophysical, sedimentological, and geochemical properties.

This project ('Part A'), along with a parallel project ('Part B'; ANLEC R&D Project 7-0320-C330), directly tested the two depocentre hypothesis by using two different but complementary approaches. Herein, we examined the mineral composition and sediment provenance of the Precipice Sandstone by integrating mineralogical analysis (10 samples from 5 wells), CA-TIMS zircon dating (2 samples from 2 wells), detrital zircon geochronology (29 samples from 7 wells), and palaeoflow analysis (8 wells), with the sedimentology and stratigraphy of all cored wells across the basin, including the new West Moonie 1 well drilled in 2020. The focus of the parallel project was to investigate potential correlations between quartz overgrowth geochemistry and the diagenetic conditions during quartz precipitation.

Overall, the study did not find evidence to support the two depocentre hypothesis. From a sediment provenance perspective, this implies that the data previously collected and analysed from the EPQ7 tenement may be a partial analogue for the West Moonie 1 well and EPQ10. The exception to this is for wells on the southern portion of the basin intersecting the top part of the Precipice Sandstone (J10-TS1 interval) where some differences were noted in the sandstone compositions and detrital zircon age spectra which may indicate different sediment sources.

The overall conclusions that are derived from the results and analysis in Part A include:

- Palaeoflow during deposition of the Precipice Sandstone to Evergreen Formation succession did not differ significantly between the northern and southern parts of the basin, and flow directions corroborate previous work. The main blocky sandstone facies exhibited the general southerly flow, but this transitioned upwards to dispersed but northerly flow directions as the TS1 boundary was approached. The stratigraphic position of this transition varied between wells; its causes are, as yet, unresolved.
- There is no significant difference in sandstone composition between the northern and southern regions of the Surat Basin, except for an interval in the upper part of the Precipice Sandstone (J10-TS1 interval) where wells in the south (including West Moonie 1) differ from wells in the north.

- The Precipice Sandstone (J10-TS1 interval) is sourced by material from the craton interior, whereas sediments in the Evergreen Formation (TS1-MFS1 interval) are characterised by mixed continental block to quartzose recycled orogen provenance.
- The complex age patterns of zircons indicate that more than one source terrane contributed sediment into the basin through the depositional history of the Precipice Sandstone and Evergreen Formation, including recycled sedimentary and metasedimentary basement rocks, plutonic and volcanic basement rocks, and contemporaneous volcanic rocks.
- A northwest sediment source from the Thomson Orogen (Nebine Metamorphics, combined units of the Anakie Inlier, and Charters Towers Province) supplied detrital material to deposit the Precipice Sandstone (J10-TS1 interval). The contribution from these blocks decreased towards the end of the Precipice Sandstone deposition and sediment was then mostly sourced from the central Thomson Orogen and Roma Shelf to the west during deposition of the Evergreen Formation (TS1-J30 interval). Significant sediment input from the New England Orogen to the east and south of the Surat Basin is also evident from the detrital zircon age spectra, as well as material recycled from the underlying Bowen Basin succession. No substantial sediment was contributed from the Lachlan Orogen.
- Absolute age dating combined with existing palynostratigraphy places the Evergreen Formation in the middle Pliensbachian to the topmost Toarcian, and by relation the Precipice Sandstone into the Lower Jurassic Sinemurian to Pliensbachian. The new precise depositional age data also hint at a diachronicity across the northwest-northeast section of the basin, but this requires additional dating to corroborate.

The main conclusions of Part B, which are compatible with these results, are (Delle Piane and Bourdet, 2022):

- The main reservoir interval in West Wandoan 1 which is situated in the northern part of the Surat Basin has a similar mineralogy to that intersected in West Moonie 1 in the southern part of the basin. Both are quartzarenites, with an overwhelming dominance of monocrystalline quartz.
- The diagenesis of both wells was similar, resulting in widespread quartz overgrowths with minor kaolinite and siderite cements.
- The amount of diagenetic quartz varies little between the two wells, on average ca. 10%. This and the temperature of homogenization derived from fluid inclusion analysis suggest similar maximum burial depths at the two well locations.
- A common crystalline source of the sediment is inferred based on the striking similarity in trace element concentrations in detrital quartz grains.
- During diagenesis, quartz cement precipitated in a temperature range of ca. 60 – 115°C from fluids with low solute content, low salinity (< 30000 ppm NaCl equivalent) and with strong contribution of meteoric water.

Together these two studies have provided strong evidence for a consistent depositional and burial history across the Surat Basin, which ultimately suggests that previous studies of the reservoir and seal characteristics in the EPQ7 tenement should be applicable to developing the EPQ10 tenement for carbon geostorage.

Acknowledgements

The authors wish to acknowledge financial assistance provided through Australian National Low Emissions Coal Research and Development. ANLEC R&D is supported by Low Emission Technology Australia (LETA) and the Australian Government through the Department of Industry, Science, Energy and Resources.

We thank and acknowledge: Nick Hall and Rob Heath from CTSCo for providing access to the West Moonie 1 core; Grant Dawson and Sue Golding for their assistance with sampling; Stratum Reservoir (Adrian Savill, Thanawat Khumtong and Keith Window) and Exploration Data Centre staff (Chris Hansen and Berny Parkes) for their technical support; Gang Xia at UQ for thin section preparation; staff at Geotrack International for sample crushing and mineral separation; Jim Crowley at Boise State University Isotope Geology Laboratory for performing CA-TIMS analysis; Charlotte Allen, Erica Porter and Karine Harumi Moromizato at CARF (QUT) for assistance with LA-ICP-MS dating; the AuScope National Argon Map project, with Marnie Forster and Davood Vasegh at ANU for providing funding and organising Ar-Ar analysis, and Hayden Dalton at the University of Melbourne for performing the analysis; Rachael Ciesiolka for sharing her geochronology data; and finally Elizabeth Alcantarino of UQ-CNG for ongoing administrative support.

Contents

List of Figures

1. Introduction

This final report documents a geochronology study of well core samples of the Precipice Sandstone of the Surat Basin in southeast Queensland. The study was completed by the University of Queensland Centre for Natural Gas (UQ-CNG) for ANLEC R&D under project 07-0320-C326.

1.1 Context

Carbon capture and storage (CCS) for Low Emission Coal Technology consists of three key elements: capture; transmission; and geological storage of CO_2. Of these, geological storage requires detailed technical characterisation of the storage reservoir and the seal rock. The Lower Jurassic Precipice Sandstone in Queensland's southern Surat Basin, targeted by CTSCo, has considerable potential as a storage reservoir but the understanding of the geology of the basin is still growing. Developing CCS through feasibility and environmental permitting requires demonstration that geological sequestration will be both effective and safe, which in turn needs in-depth knowledge of reservoir and seal rock characteristics and their variability.

Isopach maps of the Precipice Sandstone show two distinct areas of thick sediment accumulation in the north (EPQ7 tenement area; maximum thickness ~140-160 m) and south (EPQ10 tenement area; maximum thickness ~120-140 m) of the Surat Basin (Figure 1). These two areas are separated by an east-west oriented structure or palaeotopographic high where the formation thickness is significantly less (<50 m). The thickness variation predominantly occurs within the lower Precipice Sandstone "blocky sandstone", while the upper Precipice Sandstone, which consists of stacked fining- and coarsening-upward successions, shows a relatively more consistent thickness across the basin. Based on the thickness variability in the lower Precipice Sandstone, the hypothesis has emerged that the Precipice Sandstone may have been deposited in two separate sub-basins (i.e., northern and southern sub-basins) potentially fed by different source regions (c.f. La Croix et al., 2019b; 2020). Differences in sediment source areas may cause different reservoir behaviours, particularly because of differences in the characteristic porosity depth trends and different porosity-to-permeability transforms being representative for each of the two sub-basins. Alternatively, the two topographic lows may have been filled with sediment transported from the same source region, until the topography became less pronounced across the basin as the sedimentation of the upper Precipice Sandstone continued. The level of knowledge of the Precipice Sandstone storage reservoir is less well-developed in the southern Surat Basin than in the north, primarily due to lack of outcrop, sparse well data, little core material and a limited 2D seismic dataset. The acquisition of new data from the EPQ10 tenement by CTSCo provides an opportunity to test the two depocentre hypothesis and alternative models.

If the two sub-basin hypothesis is correct, the implication is that previous analysis done in the EPQ7 tenement (northern sub-basin) may have limited application to understanding and modelling of the EPQ10 tenement (southern sub-basin). If the provenance of the southern sub-basin differs from the north, and any difference in sourcing is matched by significant differences in mineralogical compositions or the nature of cements, porosity-depth trends, reservoir reactivity, and other petrophysical and composition parameters used in reservoir and geochemical models may need to be reconsidered. This project will use detrital geochronology and palaeocurrent analysis to unravel differences or similarities in sediment provenance for the Precipice Sandstone and Evergreen Formation between the north and south Surat Basin. The work builds on previous ANLEC projects concerned with outcrop analogues (Bianchi et al., 2017). The project is complementary to an ongoing UQ study investigating the regional hydrogeology of the southern Surat Basin (CI's Harald Hoffman, Sue Golding and Phil Hayes), and the concurrent ANLEC project 7-0320-C330 investigating the post-depositional diagenetic mechanisms in the north and south parts of the basin (CI Claudio Delle Piane, CSIRO).

Local understanding of the Evergreen Formation seal overlying the Precipice Sandstone reservoir is also vital to ensure long term CO_2 containment. Current conceptualizations of the Precipice Sandstone geology include a "transition zone" separating the reservoir from the seal. Owing to a historical lack of core data in the southern part of the Surat Basin, an assumption has been made that the EPQ10 tenement will be similar. If the depositional conditions are shown to have been different, the nature of such a transition zone cannot be assumed to be equivalent to that of the EPQ7 location and its character may require further investigation.

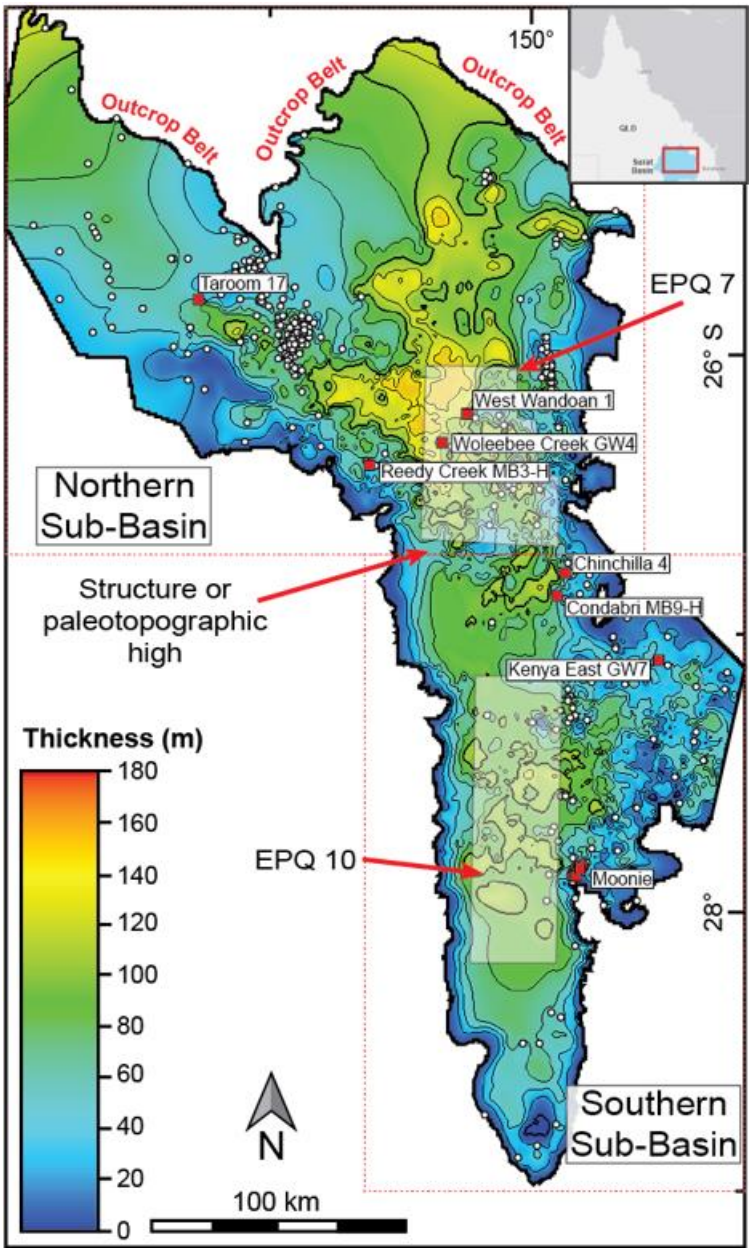

Figure 1 Lateral extent and thickness of the lower Precipice Sandstone in the Surat Basin, modified after La Croix et al. (2020).
Wells shown on the map were analysed as part of the UQ-SDAAP project. (J10-TS1 of UQ-SDAAP terminology; Wang et al., 2019).

1.2 Geological background

The Surat Basin is a large basin that extends from Queensland into New South Wales and straddles the boundary between three major building blocks of the Tasmanides – the New England, Thomson, and Lachlan orogens (Figure 2). The Surat Basin unconformably overlies the Permian-Triassic Bowen Basin succession and has been broadly described as an intracratonic basin but the driving mechanism for the basin formation remains a matter of debate (e.g., Green, 1997; Hoffmann et al., 2009; Cook and Draper, 2013). The rate of crustal subsidence decreased significantly with the initiation of the Surat Basin, compared to the underlying Bowen Basin, and was overall very slow throughout the deposition in the Surat Basin (Totterdell et al., 1991). Flanked by the largely time-equivalent Eromanga and Clarence-Moreton basins, the Surat Basin forms part of the Great Australian Superbasin (Bradshaw and Yeung, 1990; Veevers, 2001) forms part of the Great Artisan Basin and hosts significant artesian and sub-artesian groundwater resources (e.g., Green, 1997; Cook and

Draper, 2013). Both the Surat Basin and the underlying Bowen Basin have long been targeted for conventional oil and gas as well as, more recently, coal seam gas. Over the last decade, the Surat Basin has also been considered a potential CCS target (Hodgkinson et al., 2010; Bradshaw et al., 2011; Farquhar et al., 2013; Hodgkinson and Grigorescu, 2013; Pearce et al., 2015; Bianchi et al., 2019)

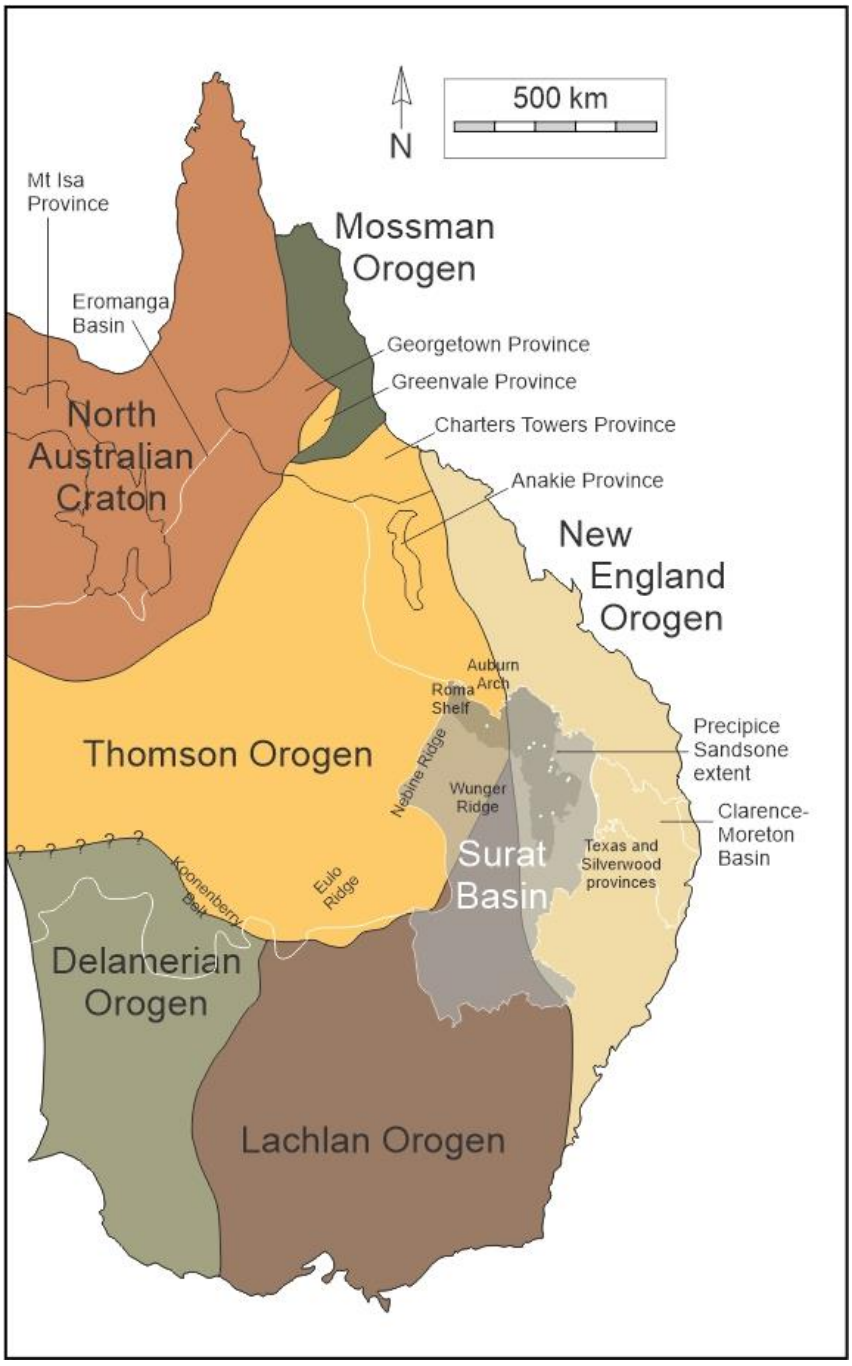

Figure 2. The five orogens comprising the Tasmanides, along with the North Australian Craton and the location of the Surat Basin study area. Modified after Glen et al., 2005; Cross et al., 2018.

The Precipice Sandstone is the oldest stratigraphic unit in the Surat Basin (Figure 3) and Great Artesian Basin. The formation outcrops in a narrow belt along the northern margin of the basin and extends southward into the subsurface with the thickest strata located in the Mimosa Syncline (Figure 1 and Figure 4). The basal Surat Basin stratal succession generally reflects the structure and remnant topography of the Bowen Basin and the Precipice Sandstone, as well as lower parts of the overlying Evergreen Formation, are clearly

compartmentalised filling in the underlying topographic relief. The maximum thickness of the Precipice Sandstone as observed in drill core is 139 m (Woleebee Creek GW4, axial part of the Mimosa Syncline, Figure 4) and the maximum thickness of the Evergreen Formation is 307 m (Chinchilla 4; Figure 4). The Precipice Sandstone is absent on the Kumbarilla Ridge and Nebine Ridge. By the time the deposition of the Hutton Sandstone began, sedimentation across the basin had become more uniform in thickness (Exon, 1976; Cook and Draper, 2013).

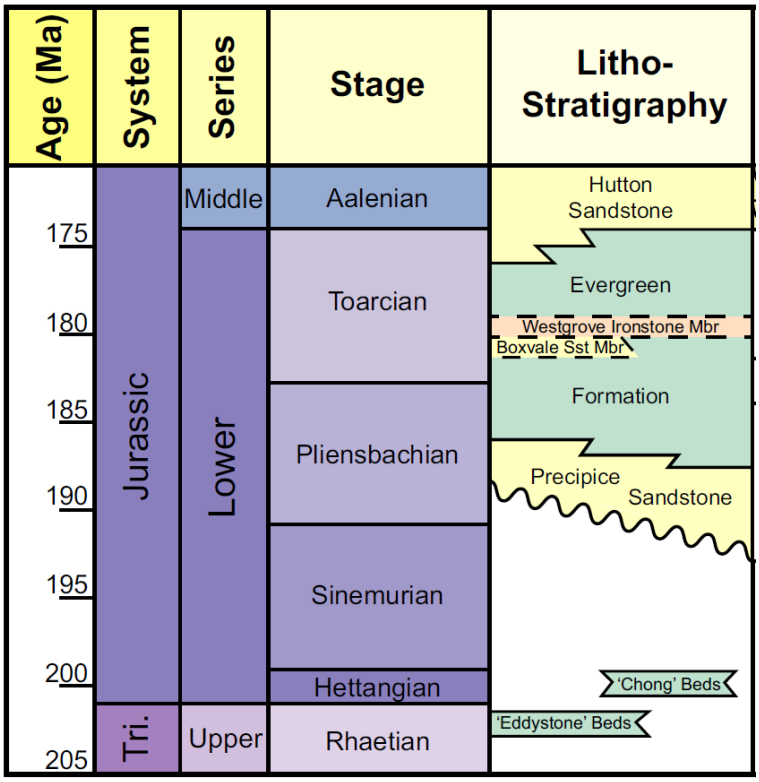

Figure 3. Stratigraphic units of the Lower Jurassic in the Surat Basin. Modified after La Croix et al. (2020). The lithostratigraphy is after McKellar (1998).

Sedimentation throughout the Surat Basin succession shows a distinct cyclicity associated with base-level fluctuations driven by eustatic sea-level changes (Exon, 1976; Exon and Burger, 1981; Jones and Patrick, 1981; Green, 1997). Six major cyclothems have been distinguished, typically with coarse-grained and relatively mature quartz-rich sandstones at the base, fining upwards into more labile siltstone, mudstone and coal. Each cycle is believed to represent an evolution of depositional environment from braided streams, through meandering streams, swamps, lakes and deltas, terminating at sea level highstand; thus, the cycles meet the definition of transgressive-regressive sequences (TR sequences) of Embry and Johannessen (1992). The Precipice-Evergreen succession forms the first sedimentary cycle of Exon (1976) and the Supersequence J of Totterdell and Krassay (1995), Hoffmann et al. (2009) and Totterdell et al. (2009). It is dominated by coarse-grained, thick-bedded, blocky sandstone in the basal part (lower Precipice Sandstone) and follows an overall fining upward trend, gradually transitioning into the fine-grained sandstones and mudstones of the Evergreen Formation. Sandstone compositions are strongly quartzose in the lower Precipice Sandstone and become more labile and mineralogically heterogenous upsection (Farquhar et al., 2013). The succession has traditionally been interpreted as high-energy braided river system deposits, transitioning up-section through a meandering fluvial system to a lacustrine environment (e.g., Exon, 1976; Green, 1997; Ziolkowski et al., 2015). Recently, a subtle shallow marine influence on the sedimentation in the upper Precipice Sandstone and Evergreen Formation has also been demonstrated based on microfossils, trace fossils and sedimentary structures (e.g., Bianchi et. al., 2018; Martin et al., 2018; La Croix et al., 2019a; 2020). In view of these new observations, the authors suggest that the succession represents a braided fluvial environment, evolving into

meandering rivers, and transitioning into deltaic and coastline settings as the system is being transgressed. The transgressive shoreline and marine connection are believed to have been located to the northeast of the Surat Basin where repeated marine incursions occurred (Martin, 1980; Bianchi et. al., 2018).

An Early Jurassic (Sinemurian to early Pliensbachian) age was assigned to the Precipice Sandstone based on palynofloral assemblages (APJ1-APJ2.2 palynostratigraphic zones of Price et al. 1985; Price 1997; and C. torrosa zone of Helby et al., 1987), as well as sparse diagnostic foraminifera (Martin et al., 2018). The Evergreen Formation has been assigned to APJ2.2-APJ3.2 palynostratigraphic zones, indicating late Sinemurian or Pliensbachian to Toarcian age (Price, 1997). The coarse-grained, erosive character of the Precipice Sandstone hinders the preservation of any syn-depositional tuff layers, making absolute age dating challenging. A single unpublished CA-TIMS tuff date from the middle of the Evergreen Formation places the unit at 184.71±0.21 Ma (Pliensbachian; Ciesiolka, 2019). A maximum depositional age is also available from detrital zircon dating of a sandstone outcropping on the north-eastern margin of the Surat Basin (50 km east of Taroom), which dates the topmost Evergreen Formation at 176.6±2.0 Ma (Todd et al., 2019). The underlying Moolayember Formation is believed to be Middle Triassic (APT3 zone; Price, 1997).

Little sedimentary provenance data have been published on the Precipice Sandstone and virtually no provenance data exist for the southern part of the basin. The few existing palaeocurrent datasets from east of the Roma Shelf area, the outcrop belt along the northern margin of the basin, and a few locations across the Mimosa Syncline indicate sediment transport towards the south and south-east for the lower Precipice Sandstone and a shift to northward directions in the upper Precipice Sandstone (Sell et al., 1972; Exon, 1976; Martin, 1980; Green, 1997; Cook and Draper, 2013; Bianchi et al., 2016; 2017; 2018; La Croix et al., 2020). The overall quartzose nature of the Precipice Sandstone, especially the lower part, suggests a dominant cratonic-type provenance, while some volcanic influence on sedimentation is evident from lithic fragments and plagioclase that become more abundant up-section. Various potential source terranes have been proposed for the northern areas of the basin, mainly based on palaeocurrent data, sandstone compositions and geographic proximity. Martin (1977; 1980) suggested sediment sourcing from the Willyama Supergroup (Broken Hill Province) based on a cluster of retrograde metamorphism ages between 521 and 460 Ma from K-Ar dating of mica (Vernon, 1969). This provenance was contested by Wiltshire (1989) who instead proposed sourcing from an unspecified terrane north-east of the Eromanga Basin, which was also the source for the Clematis Sandstone of the Bowen Basin. La Croix et al. (2020) proposed that there were multiple sediment source areas for the upper Precipice Sandstone and Evergreen Formation, with the Wunger Ridge and Roma Shelf to the west providing sediment to the western side of the basin and the Moonie–Goondiwindi Fault System as well as the New England Orogen providing sediment to the east ern side of the basin. A third south-eastern source is believed to have contributed sediment with increasing proportions through time. Several authors recognised some sediment contribution from the New England Orogen and active continental margin to the east (Martin, 1980; Wiltshire, 1989; Ciesiolka, 2019). Significant sediment contribution from the Auburn Arch and Nebine Ridge has been considered unlikely as these blocks are not believed to have been elevated at the time of deposition (Exon, 1976; Martin, 1980).

A recent unpublished detrital zircon geochronology dataset for the Precipice Sandstone and lower Evergreen Formation by Ciesiolka (2019; see fig. 13) revealed a complex age pattern that is overall dominated by 500-600 Ma, 1000-1200 Ma and 1500-1750 Ma age populations, with variable proportions of younger ages (~185-500 Ma). Based on the 500-650 Ma population referred to as Pacific-Gondwana ages (Ireland et al., 1994; 1998; Sircombe, 1999; Veevers et al., 2006; 2008), and the 900-1200 Ma population referred to as Grenvillian ages (e.g., Kay et al., 1996; McLennan et al., 2001), general sourcing from the Thomson-Delamerian Orogen was interpreted. The Anakie Block and Machattie Beds of the Thomson Orogen are potential specific sources. The 1500-1750 Ma population suggests additional sediment contribution from the Georgetown, Mount Isa and/or Arunta blocks. ~320 Ma ages are believed to reflect sourcing from the New England Orogen and the youngest populations have an unresolved source. Any significant sediment input from the Gawler Craton and the areas south of the Eromanga Basin is unlikely based on the sparsity of Palaeoproterozoic and Archean ages. This dataset is reprocessed and re-examined as part of this study.

1.3 Project objectives, novelty of research, and expected outcomes

This project will combine existing and new core data to address the knowledge gap on the sedimentology and provenance of the basal formations of the Surat Basin, which is poorly constrained especially in the southern areas. The main research aim is to characterise the sediment provenance of the main fluvial facies comprising the Precipice Sandstone. This will be achieved through U-Pb detrital zircon dating and palaeocurrent analysis, with accessory petrographic analysis of the sandstones, to characterise the types of sediment sourcing. New detrital zircon data will be compared to existing published age signatures of potential source terranes across the Tasmanides, which will allow constraining the location of probable source terranes. Additionally, applying geochronological methods will allow estimating depositional ages, adding resolution to the stratigraphic framework of the Surat Basin thus far based solely on palynology. Where possible, this approach will be extended to the transition into the overlying Evergreen Formation seal. This study will represent the first comprehensive provenance analysis of the basal part of the Surat Basin succession, and the obtained radiometric dates will be some of the first absolute depositional ages reported so far.

Detailed sedimentological description and analysis of the newly acquired West Moonie 1 well in the EPQ10 tenement will improve the understanding of the reservoir and seal quality in the most prospective CO_2 storage location within the basin and reduce uncertainty of the reservoir models used to predict flow and containment behaviour in the area. A rigorous comparison of results between the new well with cores analysed as part of the UQ-SDAAP project (Figure 1) and other publicly available data, will reveal any regional variations in petrographic characteristics and sediment sourcing. These variations will provide a guide as to whether the Precipice Sandstone should be considered laterally continuous or as two separate northern and southern depositional systems, thus testing the two depocentre hypothesis. If the two areas do differ, this might affect the reservoir properties reliant on mineralogical composition, and the regional connectivity affecting flow and containment at a basin scale. This study will inform the validity of extrapolation of static and dynamic reservoir properties and seal quality across the basin and will, in turn, help guide future exploration work.

1.4 Structure of this Report

This report provides an overview of the project background and research objectives and outlines the sampling strategy and methodology selected to address the research aims. It then presents the results obtained from each analytical method, followed by an extensive discussion that integrates all new and existing datasets to constrain the provenance of the Precipice-Evergreen succession. Interpretations include characterisation of the sediment source terranes and implications for basin development. The two depocentre hypothesis is then evaluated based on the new findings. The key points of the report are summarised in the Conclusions section. Recommendations for future research have been provided to ANLEC in a separate document. Additional relevant datasets and details of the analytical methods are provided in appendices.

2. Methods

2.1 Well selection, sampling, and sample preparation

A comprehensive analysis of five wells including the newly acquired West Moonie 1 well comprised the main data set for this study. Data reviews by UQ-SDAAP project along with the GSQ Open Data Portal were used to identify the wells of interest. Considering the limited number of cores with sufficient stratigraphic coverage through the Precipice-Evergreen interval within the Surat Basin the following wells were chosen for analysis: Chinchilla 4, Kenya East GW7, Moonie 34, and Taroom 17. Additionally, geochronological data from West Wandoan 1 and Tipton 153 obtained by Ciesiolka (2019; Appendix A) were incorporated into this project. These gave the best possible spatial coverage of the Surat Basin in both the northern and southern hypothesised depocentres (wells marked in red in Figure 4).

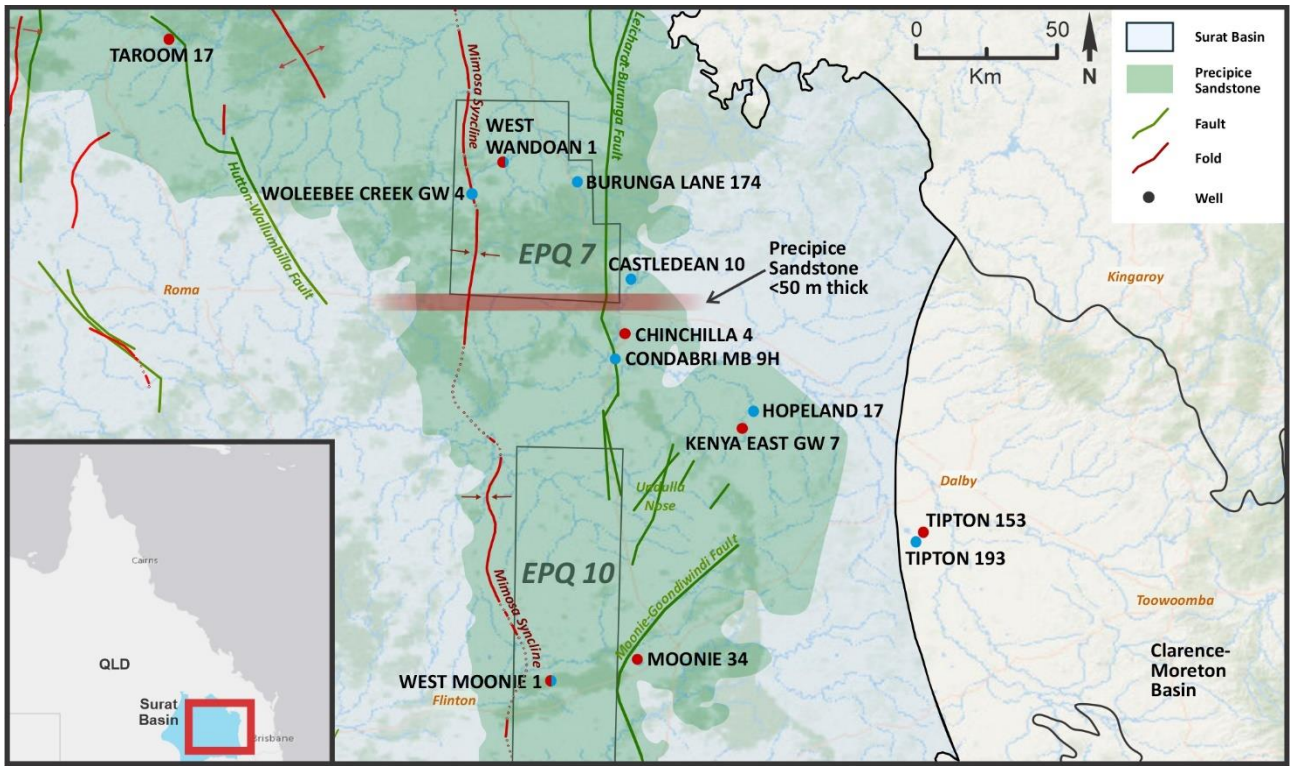

Figure 4. Location of wells used for this study together with the outlines of CTSCo Greenhouse Gas exploration tenements.
Cored wells selected for laboratory analyses are shown in red, and wells selected for image log palaeocurrent analysis are shown in blue.

The stratigraphic logs, sample depths and relevant stratigraphic boundaries are shown in Figure 5, and full sample details are provided in Table 1. A total of 46 samples from the five wells were collected, including 29 samples for detrital geochronology. The samples were collected from coarse-grained (medium- to coarse-grained sandstone), fluvial channel facies to ensure sampling of the material that was transported from the source region into the basin by rivers. Intervals with visible detrital muscovite grains were favoured. Laser Ablation Inductively Coupled Plasma Mass Spectrometry (LA-ICP-MS) detrital zircon dating was performed on all 29 samples, and out of this sample set, 14 samples that contained moderate to high numbers of detrital muscovite grains were also selected for $^{40}Ar/^{39}Ar$ mica dating. Thin sections of each geochronology sample were also analysed for petrography. Thirteen additional samples were collected for petrography only, mainly from medium-grained sandstones to ensure consistency during point counting.

Four tuff horizons were sampled from the Chinchilla 4, Kenya East GW7 and West Moonie 1 wells. The tuffs were shipped to the Boise State University Isotope Geology Laboratory (Idaho, US) to assess their suitability for CA-TIMS dating of primary volcanic zircons to obtain high-precision depositional ages.

Finally, eight wells with available image log datasets were selected for palaeocurrent analysis. Two of these were the West Wandoan 1 and West Moonie 1 for direct comparison of the EPQ7 and EPQ10.

For consistency of communication and integration with previous studies undertaken by UQ, the sequence stratigraphic framework and terminology presented in Wang et al. (2019) and La Croix et al. (2019b) is used (Figure 6). In that framework, the “lower Precipice Sandstone” (often informally referred to as the “blocky sandstone”) falls within the J10-TS1 interval, the “upper Precipice Sandstone” is contained within the TS1-MFS1 interval, and the rest of the Evergreen Formation resides within the MFS1-J30 interval.

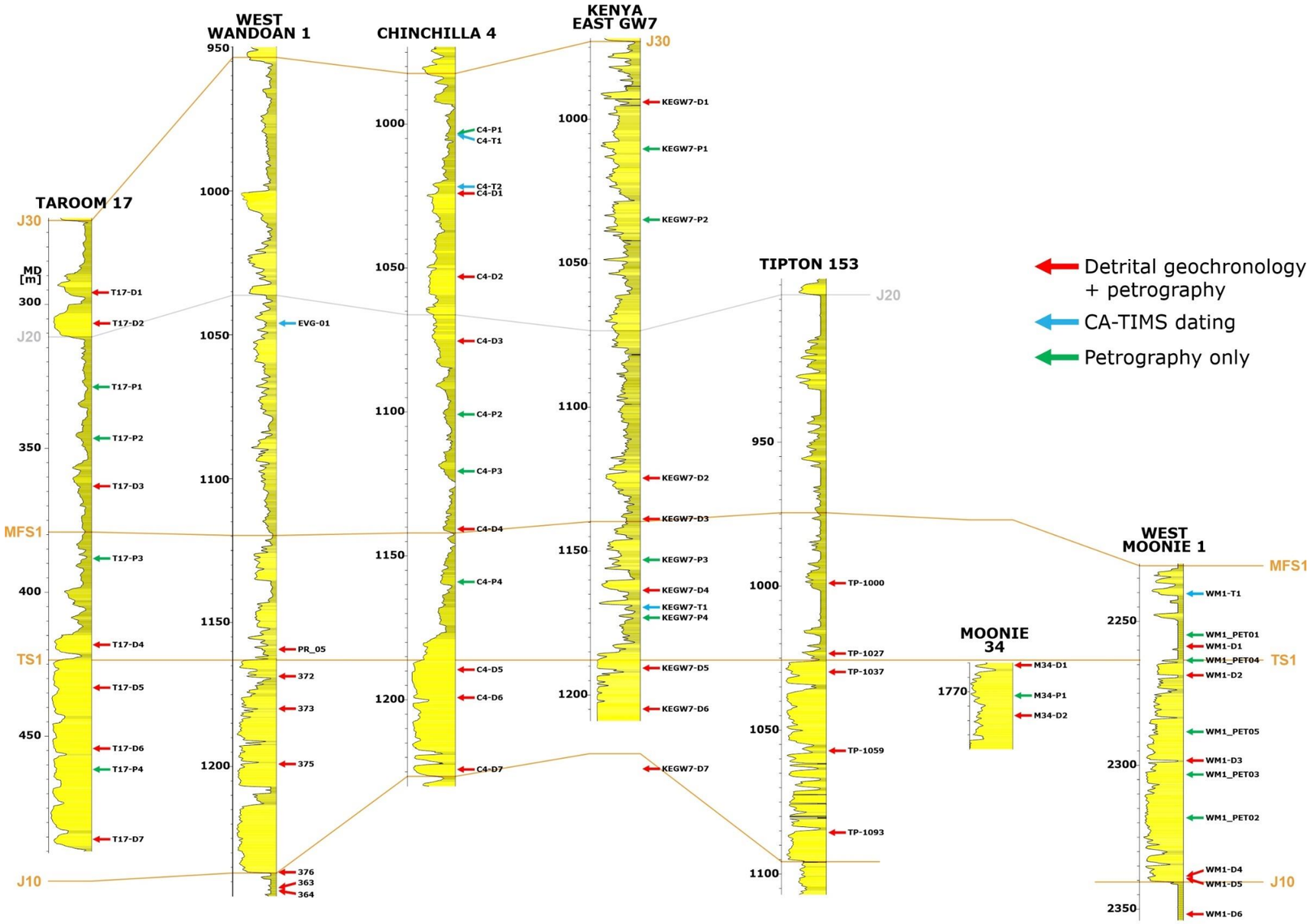

Figure 5. Cross-section showing the samples analysed in this study by well with the section flattened on the TS1 stratigraphic surface.
Samples from Tipton 153 and West Wandoan 1 are from Ciesiolka (2019) and petrography from West Moonie 1 from CTSCo (unpublished report).

Table 1. Details of core samples analysed in this study. DZ – detrital zircon dating.

Well	Sample ID	Depth from [m]	Depth to [m]	Analysis type	Lithology	Stratigraphic position
Chinchilla 4	C4-P1	1003.1	1003.05	Petrography	Sandstone	MFS1-J30
Chinchilla 4	C4-T1	1003.45	1003.4	CA-TIMS	Tuff	MFS1-J30
Chinchilla 4	C4-T2	1022.1	1022.05	CA-TIMS	Tuff	MFS1-J30
Chinchilla 4	C4-D1	1024.45	1023.85	DZ + petrography	Medium-grained quartz sandstone	MFS1-J30
Chinchilla 4	C4-D2	1052.9	1053.5	DZ + petrography	Medium-grained quartz-lithic sandstone	MFS1-J30
Chinchilla 4	C4-D3	1075.65	1075.05	DZ + petrography	Medium-grained quartz sandstone	MFS1-J30
Chinchilla 4	C4-P2	1100.8	1100.75	Petrography	Sandstone	MFS1-J30
Chinchilla 4	C4-P3	1120.55	1120.5	Petrography	Sandstone	MFS1-J30
Chinchilla 4	C4-D4	1140.65	1140.05	DZ + petrography	Medium-grained quartz sandstone	MFS1-J30
Chinchilla 4	C4-P4	1158.6	1158.55	Petrography	Sandstone	TS1-MFS1
Chinchilla 4	C4-D5	1189.65	1189.1	DZ + petrography	Medium- to coarse-grained quartz sandstone	J10-TS1
Chinchilla 4	C4-D6	1199.45	1198.85	DZ + petrography	Coarse- to v. coarse-grained quartz sandstone	J10-TS1
Chinchilla 4	C4-D7	1224.4	1223.9	DZ + petrography	Medium- to coarse-grained quartz sandstone	J10-TS1
Kenya East GW7	KEGW7-D1	994.3	993.9	DZ + petrography	Sandstone	MFS1-J30
Kenya East GW7	KEGW7-P1	1010.3	1010	Petrography	Fine- to medium-grained lithic sandstone	MFS1-J30
Kenya East GW7	KEGW7-P2	1035	1034.95	Petrography	Sandstone	MFS1-J30
Kenya East GW7	KEGW7-D2	1125	1124.7	DZ + petrography	Medium-grained quartz sandstone	MFS1-J30
Kenya East GW7	KEGW7-D3	1139	1138.7	DZ + petrography	Medium-grained quartz sandstone	MFS1-J30
Kenya East GW7	KEGW7-P3	1153	1153.05	Petrography	Sandstone	TS1-MFS1
Kenya East GW7	KEGW7-D4	1163.8	1163.5	DZ + petrography	Medium-grained quartz sandstone	TS1-MFS1
Kenya East GW7	KEGW7-T1	1169.64	1169.53	CA-TIMS	Tuff	TS1-MFS1
Kenya East GW7	KEGW7-P4	1173.2	1173.25	Petrography	Sandstone	TS1-MFS1
Kenya East GW7	KEGW7-D5	1190.7	1190.4	DZ + petrography	Medium-grained quartz sandstone	J10-TS1
Kenya East GW7	KEGW7-D6	1205	1204.7	DZ + petrography	Medium- to coarse-grained quartz sandstone	J10-TS1
Kenya East GW7	KEGW7-D7	1226	1225.7	DZ + petrography	Medium- to coarse-grained quartz sandstone	J10-TS1
Moonie 34	M34-D1	1760.55	1760.2	DZ + petrography	Coarse-grained quartz sandstone	J10-TS1
Moonie 34	M34-P1	1771.35	1771.3	Petrography	Sandstone	J10-TS1
Moonie 34	M34-D2	1777.8	1777.45	DZ + petrography	Coarse- to v. coarse-grained quartz sandstone	J10-TS1
Taroom 17	T17-D1	295.6	295	DZ + petrography	Fine- to medium-grained quartz sandstone	MFS1-J30
Taroom 17	T17-D2	307.35	306.75	DZ + petrography	Medium-grained quartz sandstone	MFS1-J30
Taroom 17	T17-P1	328.45	328.4	Petrography	Sandstone	MFS1-J30
Taroom 17	T17-P2	346.8	346.75	Petrography	Sandstone	MFS1-J30
Taroom 17	T17-D3	363.25	362.65	DZ + petrography	Medium-grained quartz sandstone	MFS1-J30
Taroom 17	T17-P3	387.15	387.1	Petrography	Sandstone	TS1-MFS1
Taroom 17	T17-D4	417.85	417.25	DZ + petrography	Medium- to coarse-grained quartz sandstone	TS1-MFS1
Taroom 17	T17-D5	432.75	432.2	DZ + petrography	Medium-grained quartz sandstone	J10-TS1

Taroom 17	T17-D6	454.7	455.3	DZ + petrography	V. coarse-grained quartz sandstone	J10-TS1
Taroom 17	T17-P4	462.05	462	Petrography	Sandstone	J10-TS1
Taroom 17	T17-D7	485.7	485.1	DZ + petrography	V. coarse-grained quartz sandstone	J10-TS1
West Moonie 1	WM1-T1	2240.65	2240.6	CA-TIMS	Tuff	TS1-MFS1
West Moonie 1	WM1-D1	2258.77	2258.67	DZ + petrography	Medium-grained quartz sandstone	TS1-MFS1
West Moonie 1	WM1-D2	2269.5	2269.4	DZ + petrography	Pebbly sandstone	J10-TS1
West Moonie 1	WM1-D3	2298.2	2298.1	DZ + petrography	Coarse-grained quartz sandstone	J10-TS1
West Moonie 1	WM1-D4	2338.6	2338.5	DZ + petrography	Coarse-grained quartz sandstone	J10-TS1
West Moonie 1	WM1-D5	2339.3	2339.2	DZ + petrography	Medium- to coarse-grained lithic sandstone	Below J10
West Moonie 1	WM1-D6	2351.7	2351.6	DZ + petrography	Medium- to coarse-grained lithic sandstone	Below J10

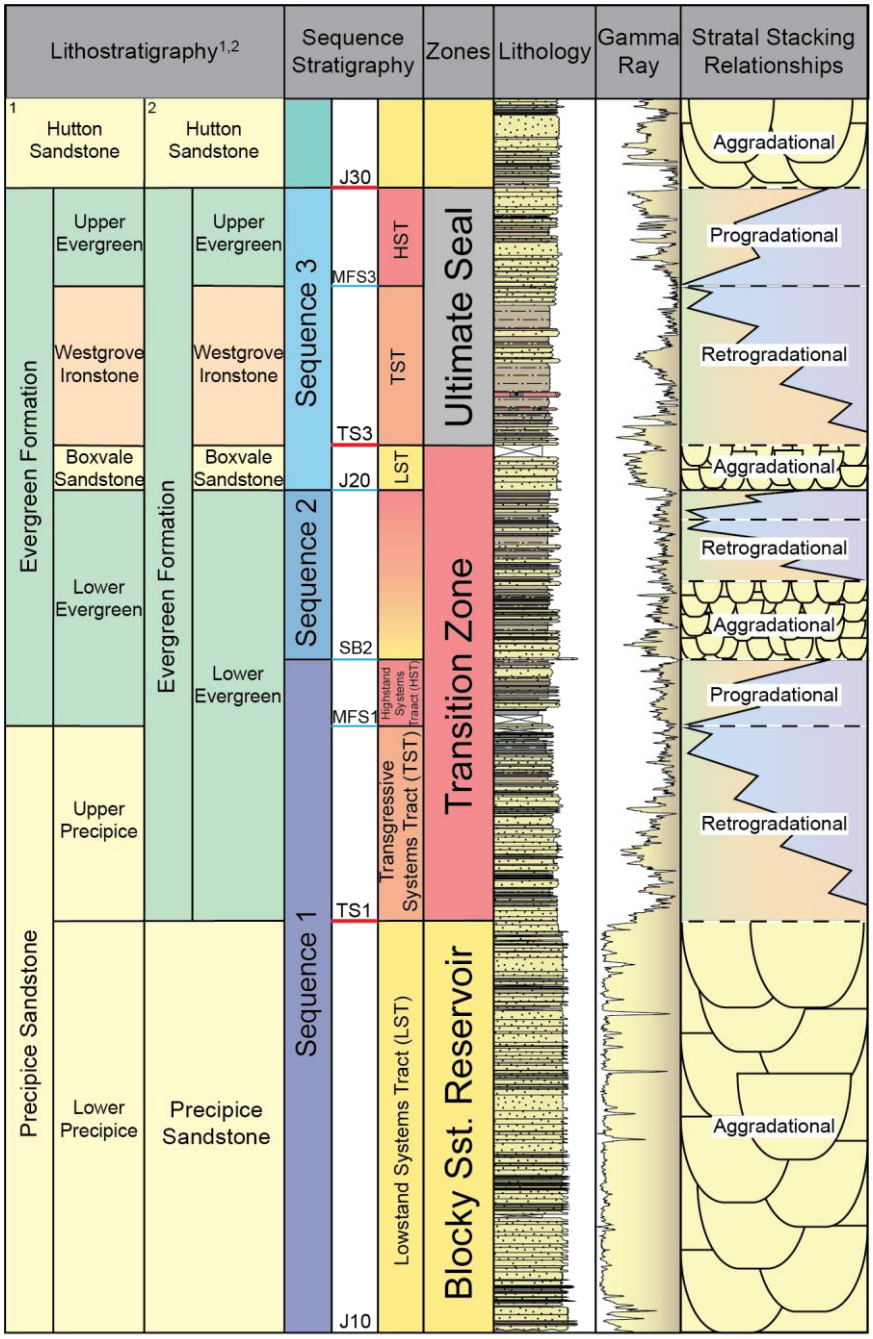

Figure 6. Stratigraphic nomenclature of the Precipice Sandstone and Evergreen Formation. The 'Zones' column refers to the main reservoir modelling intervals discussed herein. Modified after La Croix et al., 2019b.

2.2 Analytical methods

To investigate sediment provenance of the Precipice Sandstone, isotopic dating of zircon and mica were used and supplemented by petrographic description and quantification of mineral composition, grain size, shape and sorting, as well as palaeocurrent analysis from image logs.

Three unique isotopic dating methods are employed: Laser Ablation Inductively Coupled Plasma Mass Spectrometry (LA-ICP-MS) zircon dating, Chemical Abrasion Thermal Ionization Mass Spectrometry (CA-

TIMS) zircon dating and $^{40}Ar/^{39}Ar$ mica dating. This approach will allow two separate research objectives to be addressed: 1) identification of the sediment source terranes (sediment provenance), and 2) constraining the depositional ages of the analysed sedimentary formations (i.e., the age when the sampled formation was laid down). The LA-ICP-MS dating of detrital zircon and $^{40}Ar/^{39}Ar$ dating of detrital mica will both provide information on the sedimentary provenance, while the CA-TIMS dating of volcanic zircon from tuffs will provide the depositional ages. Note that *maximum* depositional ages (MDA) can also be obtained using the LA-ICP-MS method and will be included in this project's outcomes. Ages produced by this technique, however, are imprecise with up to ~5% systematic and instrumental errors, and therefore, where possible, the CA-TIMS technique will be relied upon for constraining high-precision depositional ages of the Precipice-Evergreen succession.

- LA-ICP-MS dating of detrital zircon was used to determine the ages of the sediment source material(s). The U-Pb system in zircon has a high (>900ºC) closure temperature, i.e., the temperature at which the isotopic system becomes shut and the daughter isotope becomes immobile within the crystal lattice (e.g., Dodson, 1973; Carrapa, 2010). This is approximately the temperature of crystallisation from a cooling felsic (high silica content) magma. A U-Pb age of a detrital zircon in a sedimentary rock, therefore, represents the time of the primary magmatic crystallisation of the zircon crystal in the source rock. The detrital zircon age spectra will allow characterisation of bulk sediment source types and specific source terrane(s) by comparing the new age signatures with known ages of potential source terranes from literature. Comparing age spectra from the northern and southern depocentres will determine if the two areas were supplied by different sources. Spatial and temporal trends will be identified.

  Crushing and mineral separation of the 29 core samples selected for detrital geochronology was performed at Geotrack International (VIC) by standard procedures for isotopic dating. Approximately 200 zircon grains per sample were mounted in epoxy, polished and imaged using scanning electron microscopy with a cathodoluminescence detector (SEM-CL). LA-ICP-MS dating was performed at The Central Analytical Research Facility (QUT) and the data were processed using the Iolite software package (Paton et al., 2011). Age spectra are presented as combined kernel density estimates (KDE) and histograms generated in R based IsoplotR (Vermeesch, 2018). KDE is preferred in this study over probability density plots (PDP) as a statistically more robust alternative, unbiased by over-smoothing of imprecise measurements (Vermeesch, 2012). The bandwidth for KDE curves in all samples was set to 20 Ma. All presented ages are concordant within 1σ error. Full methodology details and instrument settings are available in 0. The existing detrital geochronology dataset from Ciesiolka (2019) was reprocessed following the same methodology and incorporated in this study.

  Several statistical approaches exist to calculate maximum depositional ages (MDA) from detrital zircon age suites (e.g., Dickinson and Gehrels, 2009; Coutts et al., 2019; Vermeesch, 2021). Maximum depositional ages represent the age for the youngest sediment source recorded within the detrital age suite of a sample. Therefore, regardless of the method used, it is critical to note that a MDA can commonly be older than the true depositional age of the formation, sometimes considerably (e.g., Dickinson and Gehrels, 2009; Tucker et al., 2013; Coutts et al., 2019; Sharman and Malkowski, 2020). For a MDA to equate to or approximate the true depositional age, a significant proportion of contemporary volcanic material must be present in the sediment. It is also possible, although much less common, for a calculated MDA to be *younger* than the true depositional age. Although such instances have been previously attributed to Pb loss, recent studies suggest that this is an unlikely cause given the low diffusivity of Pb in zircon under P-T conditions typical of sedimentary basins (Copeland, 2020; Vermeesch, 2021). It is more likely that anomalously young ages result from rare instances where analytical uncertainties are incorrectly characterised. In this study, MDAs were calculated using several methods following Dickinson and Gehrels (2009) and Vermeesch (2021), for comparison.

  Multidimensional scaling (MDS) analysis is used to visualise stratigraphic and lateral trends in provenance. This non-metric analysis measures the statistical distance between age distributions in each sample using the Kolmogorov-Smirnov statistic to express the dissimilarity between the plotted samples (Vermeesch,

2013; Vermeesch et al., 2016). The MDS plot serves as a 'map' in which samples with similar age signatures cluster closely together and those with dissimilar signatures plot far apart.

- $^{40}Ar/^{39}Ar$ single fusion dating of detrital mica. This dataset will complement provenance data obtained from U-Pb dating of detrital zircon. Like LA-ICP-MS detrital zircon dating, this dating method will provide absolute ages of the sediment source material(s). However, the $^{40}Ar/^{39}Ar$ system in muscovite is a low closure-temperature isotopic system and thus will provide a younger age for the same rock sample than the high closure-temperature U-Pb system in zircon. This multi-method approach has the potential to provide a further resolution on sediment sourcing and constrain the cooling and exhumation history of the source terrane(s) that may not be recorded by zircon dating alone (e.g., Carrapa, 2010; Haines et al., 2004).

  The analysis is funded by the AuScope National Argon Map project (https://earthsciences.anu.edu.au/research/facilities/auscope-initiative-national-argon-map) and the data will be made available on the National Argon Map, while we retain the intellectual property. The 14 samples selected for 40Ar/39Ar dating have been shipped to the University of Melbourne where the analysis has begun. The first part of the analysis requires all mica grains to be neutron-irradiated, which might take up to 6 months. Therefore, the analysis was not completed in time for the final project report. The opportunity of including 40Ar/39Ar geochronology in the project (at no cost) was identified and approved after the project commenced, and the time required was not accounted for in the project proposal. The results, however, will provide a valuable addition to a later publication on sedimentary provenance.

- CA-TIMS U-Pb zircon dating of syn-depositional tuffs. This technique is used to constrain high-precision depositional ages of the Precipice-Evergreen succession. This will increase the confidence of well-to-well correlations by identifying time-equivalent surfaces.

  Sample crushing and mineral separation were performed at Boise State University Isotope Geology Laboratory by standard procedures. Zircon grains were then mounted in epoxy, polished, imaged on SEM-CL and analysed using LA-ICP-MS in preparation for CA-TIMS dating. Full methodology details and instrument settings are available in 0.

- Petrographic analysis. Core samples were thin-sectioned and analysed using optical microscopy to describe and quantify sediment characteristics such as mineral composition, grain size, shape and sorting, which affect reservoir and seal reactivity and porosity.

  Forty-four polished sandstone thin sections were prepared by standard techniques at the UQ Sample Preparation Laboratory. Optical microscopy was used to characterise sandstone composition, sedimentary texture, overall provenance, and to quantify modal the abundance of detrital grains. Special focus was on any differences between samples from the northern and southern hypothesised depocentres. Our dataset from Chinchilla 4, Kenya East GW7, Moonie 34, Taroom 17 and West Moonie 1 drill cores was complemented by existing data from West Moonie 1 (CTSCo, unpublished report), West Wandoan 1 and Tipton 153 (Ciesiolka, 2019). Sample depths are shown in Figure 5.

  QFL (quartz-feldspar-lithic) compositions of sandstones were determined from point counting by the Gazzi-Dickinson method (Dickinson, 1970; Ingersoll et al., 1984). The technique uses a petrographic microscope to determine the type of mineral grains at >500 randomly selected points in a thin section. As part of this study, point counting was performed on 10 medium-grained sandstone samples from Kenya East GW7, Chinchilla 4 and Tipton 153 core, which are presented together with the previous datasets. Point counts were separated into quartz, feldspar, rock fragments and matrix. Mono- and polycrystalline varieties of quartz were distinguished, and where rock fragment identification was possible, the lithic grains were divided into sedimentary (including chert), metamorphic, volcanic and plutonic. Porosity, accessory minerals such as mica and heavy minerals, authigenic minerals and cements, were not included in the count. Sandstone compositions were plotted on QFL ternary diagrams and classified using the descriptive scheme proposed by Garzanti (2016; 2019; Figure 7).

As a first pass at provenance interpretation, sandstone compositions were additionally plotted on provenance classification diagrams following Dickinson and Suczek (1979) and Dickinson et al. (1983) to provide indications of influences from the continental belt, recycled orogen and magmatic arc on sedimentation. This method was used with caution, rather than as a rigid provenance classification tool, as the accuracy of inferring geodynamic setting from detrital grain modes is limited. Using sandstone petrography as a provenance indicator remains valid as a first pass at provenance characterisation, and as a graphical tool to illustrate mixing of sediment from various end-member source types (Dickinson, 1985; von Eynatten et al., 2003; Dokuz and Tanyolu, 2006; Weltje, 2006; Garzanti, 2016; 2019). This is especially useful where temporal changes in sediment sourcing occur that are likely to be reflected in detrital grain compositions. Specific rock fragment types were recorded during point counting and used to help interpretations, as lithic grains have been shown to contain particularly valuable provenance information (e.g., Garzanti, 2019). Sandstone petrography complements the detrital zircon study for comprehensive provenance analysis.

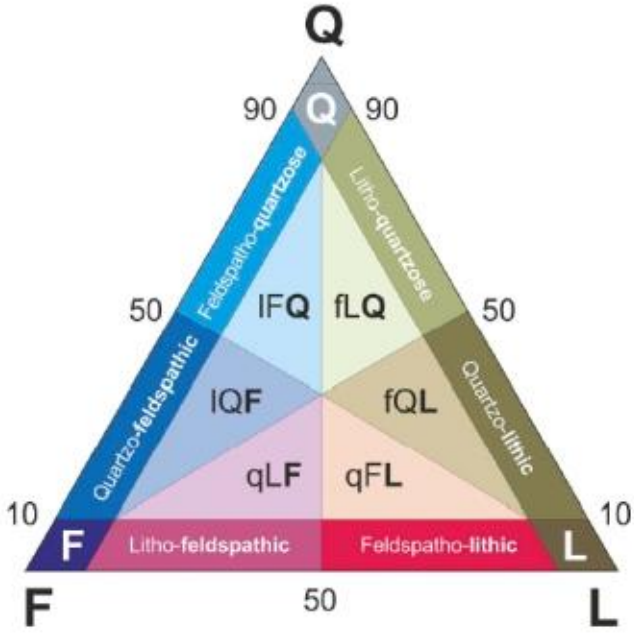

Figure 7. Descriptive petrographic classification for sandstones after Garzanti (2016; 2019). Sandstones are classified according to their main components provided they exceed 10% QFL. According to standard use, the less abundant component goes first, the more abundant last (e.g., litho-feldspatho-quartzose composition translates into Q > F > L > 10%QFL).

- Palaeocurrent analysis was performed to aid the understanding of sediment dispersal patterns and comparison with regional trends, which is critical to identifying potential source terranes. Palaeocurrent directions were obtained from image log datasets in eight wells shown in blue in Figure 4. The West Moonie 1 well was imaged using an FMI (Formation Micro Imager) tool and has a higher resolution than the rest of the wells, which were imaged using a CMI (Compact Microresistivity Imager) tool. Structural bedding and cross-bedding orientations were picked manually using Techlog software (Schlumberger). The results were compared to the limited existing published palaeocurrent data (Martin, 1980; Bianchi et al., 2017; 2018; La Croix et al., 2020).
- Facies analysis of all sampled wells, except for West Moonie 1, was performed for the UQ-SDAAP project. Interpretation of West Moonie 1 lithofacies was originally intended as part of this project, however, full core logging and facies analysis had already been performed by a CTSCo contractor prior to the project commencement. To avoid duplication of effort, the existing West Moonie 1 log was used to support sampling, laboratory analyses and data interpretation in this project.

3. Results

3.1 Petrography

Twenty-six samples were point counted for their mineralogical content. Sandstone mineralogical composition for each sample is presented on QFL diagrams in Figure 8 and detailed point counting results are given in 0. Strata below the J10 surface (Moolayember Formation) typically contain between 50-60% quartz, and the rest of the grain framework is composed of subequal proportions of feldspar (20-25%) and lithic grains (20-25%; Figure 8). The sandstones are matrix-rich with low porosity and are texturally immature with angular to subangular grains and moderate sorting (Figure 9). Fe and Mn cements are common. The lithic grains include chert, metasedimentary and volcaniclastic rock fragments.

The J10-TS1 interval (lower Precipice Sandstone) throughout the study area is characterised by clean quartzose sandstones (all but one analysed sample contain >95% quartz; Figure 8) with little to no matrix and low proportions of cement, resulting in an overall very high porosity. The sandstones are typically coarse- to medium-grained. Monocrystalline quartz grains dominate and show a variety of characteristics, ranging from clear grains displaying parallel extinction, to containing fluid inclusion trails with undulose extinction. Where cement is present, it is typically composed of kaolinite and siderite. Thin authigenic quartz overgrowths are rare and do not significantly impact the porosity. The textural maturity is typically moderate, with subrounded to subangular clasts and moderate sorting (Figure 10). These units vary between structureless and faintly cross-laminated on the thin section scale. Rare lithic grains are mainly chert and volcaniclastic rock fragments. Accessory minerals are also rare and include detrital muscovite, zircon and rutile.

Quartz is also the dominant grain type in the TS1-MFS1 interval (upper Precipice Sandstone), but this part of the formation shows a much wider range of compositions, varying from feldspatho-litho-quartzose through litho-feldspatho-quartzose to quartzose (Figure 8. QFL classification of samples in this study after Garzanti (2016; 2019). Grain size is, on average, finer than in the lower Precipice Sandstone and varies from medium- to very fine-grained. The sandstones vary between structureless and cross-laminated and show poor to moderate textural maturity. This unit is characterised by much higher proportions of matrix and cement and lower porosity compared to the quartzose sandstones of the lower Precipice Sandstone. Pressure dissolution features are observed at some quartz grain boundaries, which were absent in the underlying section, and authigenic quartz overgrowths are more common. Various types of cements are present such as authigenic clay minerals (typically kaolinite), calcite, and less common and more localised, siderite and Fe oxides. Kaolinite and calcite typically occur as pore-filling cements, while siderite and oxides are pore-lining. Both mono- and polycrystalline quartz varieties are present. Feldspar grains include plagioclase and alkali varieties (both orthoclase and microcline), but plagioclase is more common. The feldspar clasts are typically sericitised, but unaltered grains are also present. Lithic fragments are dominated by chert and metasedimentary rocks, with less common volcanic, volcaniclastic, fine-grained siliciclastic and high-grade metamorphic rock fragments. Plutonic rock fragments are very rare. Among accessory minerals, mica is the most abundant, with rare zircon, rutile and glauconite also present. In contrast to the underlying section, both muscovite and biotite mica groups are observed.

Sandstones of the MFS1-J30 interval (Evergreen Formation) have feldspatho-litho-quartzose compositions (Figure 8). Grain size varies from medium- to very fine-grained but the overall fining-upward trend continues throughout the J10-J30 succession. The Evergreen Formation sandstones are matrix-rich and show variable sorting and moderate to poor rounding (Figure 12). Various types of cement are present, typically clay minerals and calcite, resulting in low porosities. Less commonly, siderite is observed, often showing characteristic rhomboidal crystals. Clay minerals are overall more common than in the Precipice Sandstone. Feldspar grains are dominated by plagioclase, but alkali feldspars are also present. Feldspar alteration is common. Lithic grains include chert, andesitic volcanic, volcaniclastic, metasedimentary and other metamorphic rock fragments. Accessory minerals include muscovite, biotite, rare glauconite, zircon, rutile and opaque minerals.

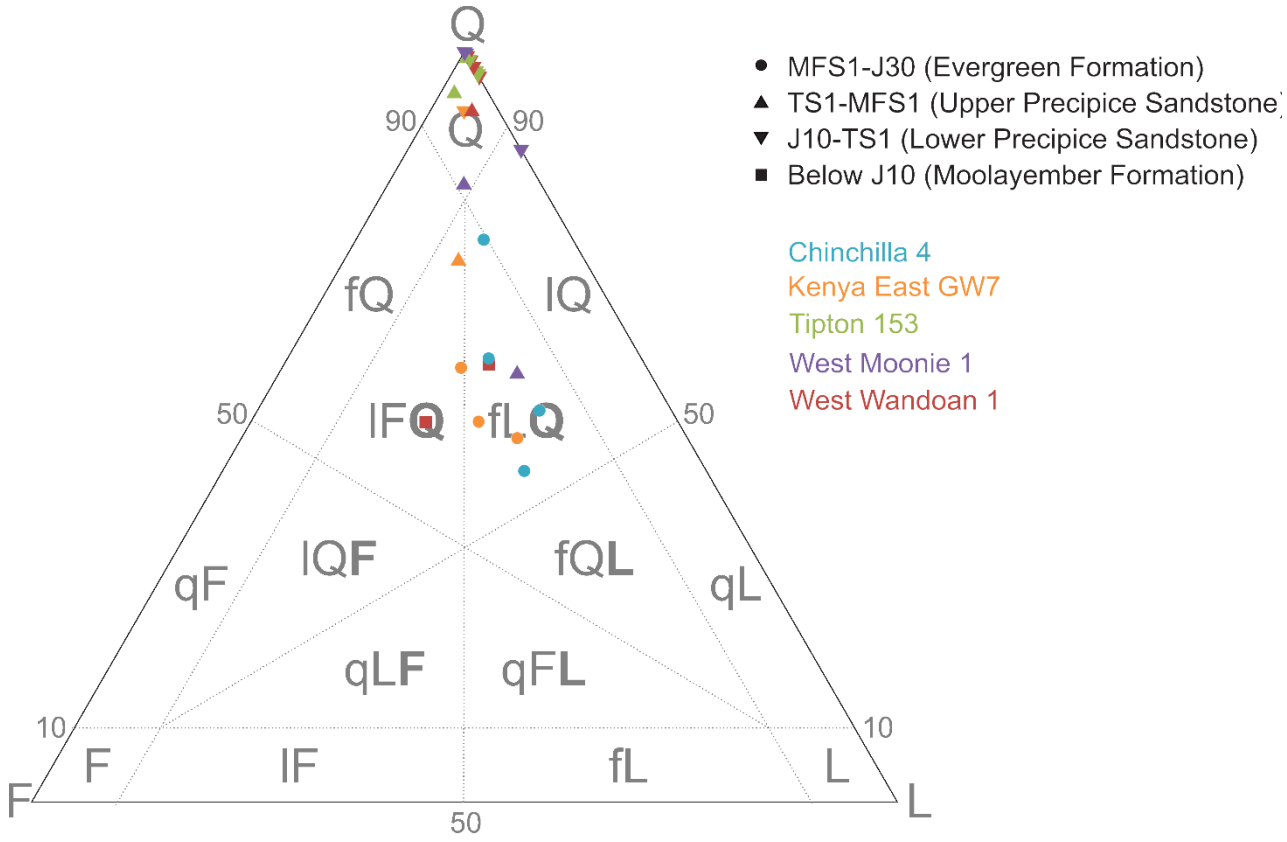

Figure 8. QFL classification of samples in this study after Garzanti (2016; 2019).

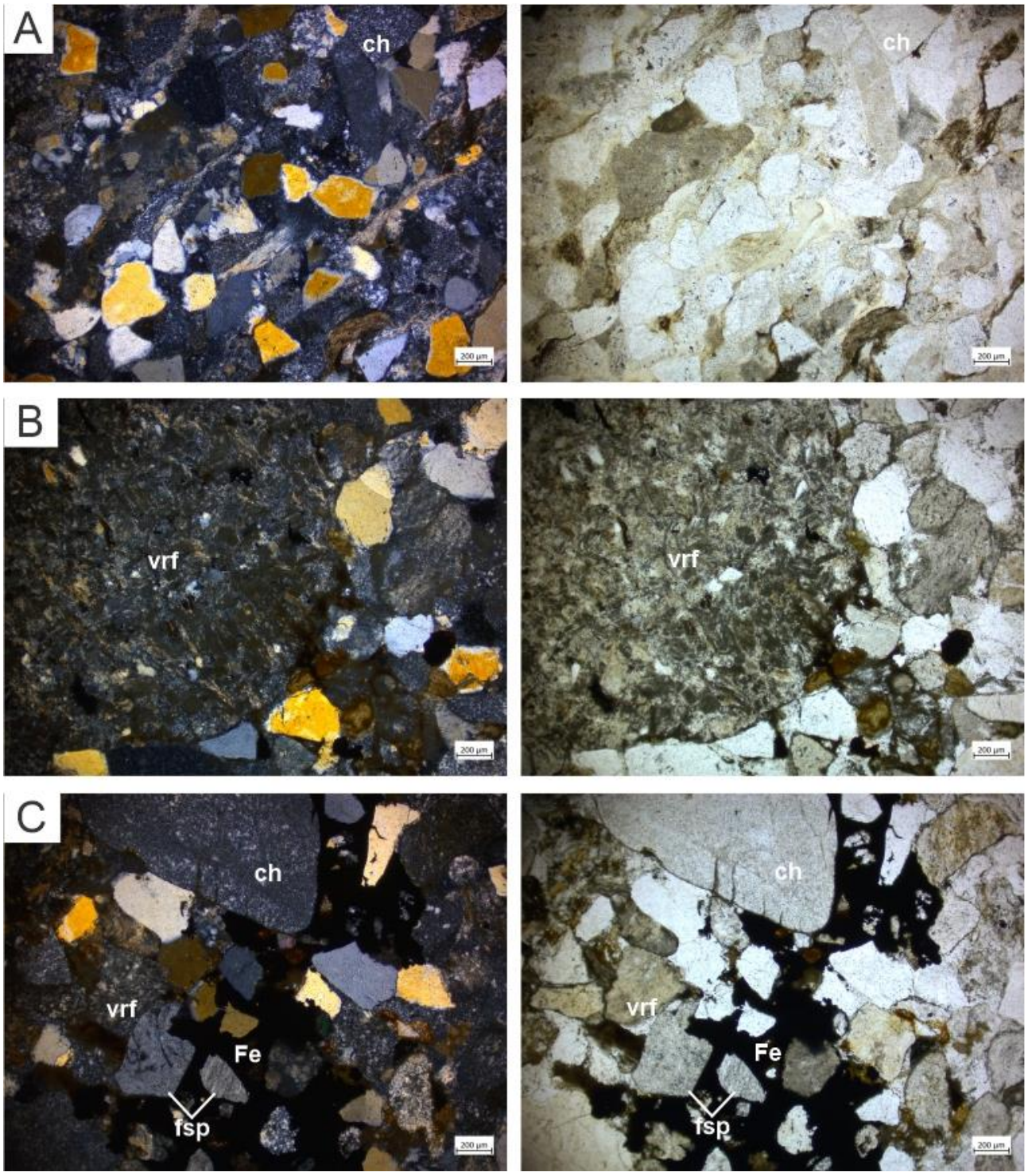

Figure 9. Microphotographs of the Moolayember Formation (below J10 surface). Cross-polarised light images are on the left, plane-polarised images are on the right.
A) Litho-quartzose sandstone. Sample WM1-D5 (West Moonie 1, 2339.3-2339.2 m). B) Volcaniclastic fragment (unwelded, with glass shards) in feldspatho-litho-quartzose sandstone. Sample WM1-D6 (West Moonie 1, 2351.7-2351.6 m). C) Fe oxide cementation. Sample WM1-D6. ch – chert, Fe – iron oxide, fsp – feldspar, vrf – volcanic rock fragment.

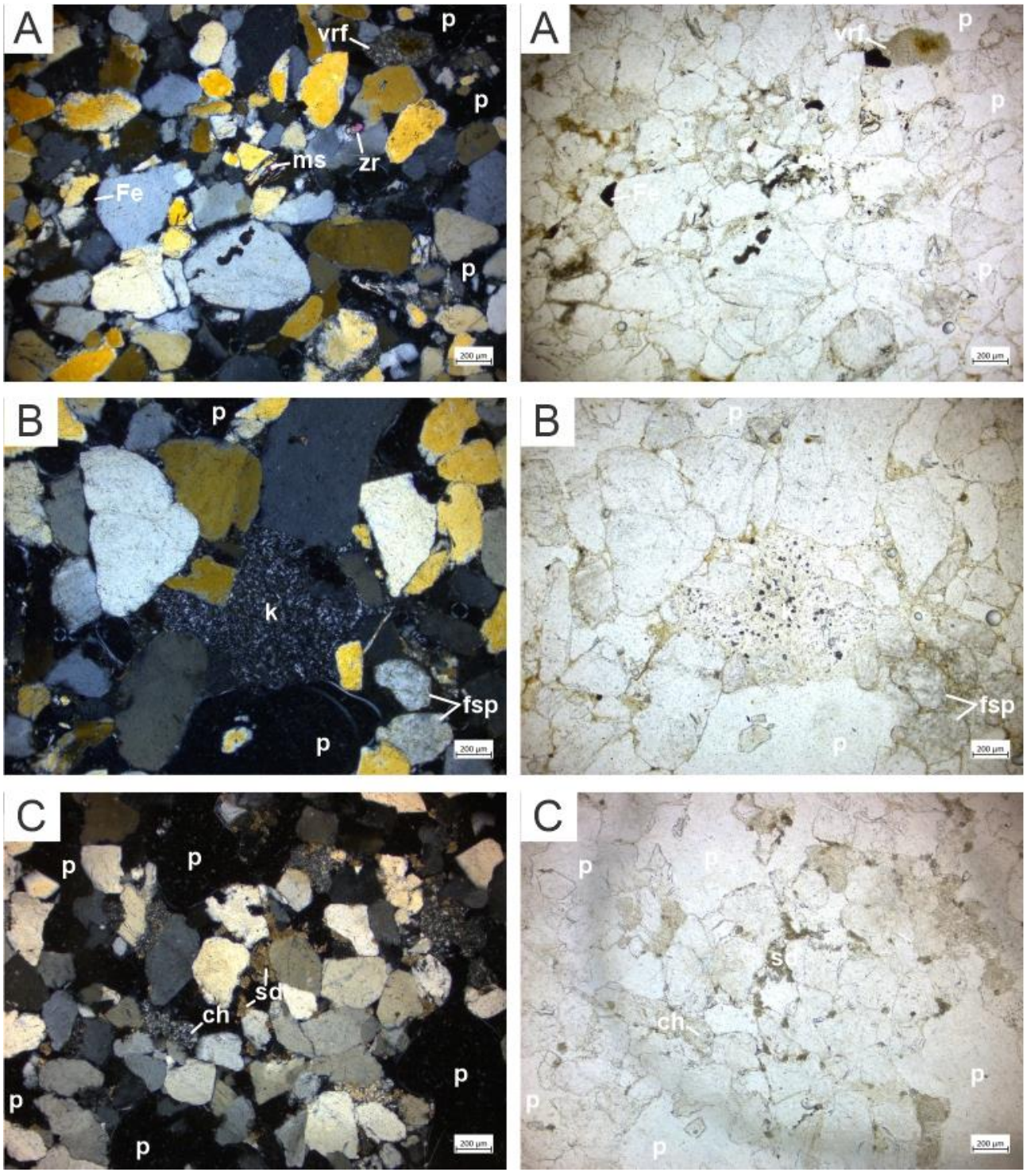

Figure 10. Microphotographs of quartzose sandstones from the lower Precipice Sandstone (J10-TS1). Cross-polarised light images are on the left, plane-polarised images are on the right.
A) Note the detrital muscovite and zircon grains. Sample C4-D5 (Chinchilla 4, 1189.65 - 1189.1 m). B) Note kaolinitic cement in the centre of the photograph. Sample C4-D6 (Chinchilla 4, 1199.45 - 1198.85 m). C) Note high porosity and sparse cementation by siderite. Sample KEGW7-D5 (Kenya East GW7, 1190.7 - 1190.4 m). ch – chert, Fe – iron oxide, fsp – feldspar, k – kaolinite, ms – muscovite, p – porosity, sd – siderite, vrf – volcanic rock fragment, zr – zircon.

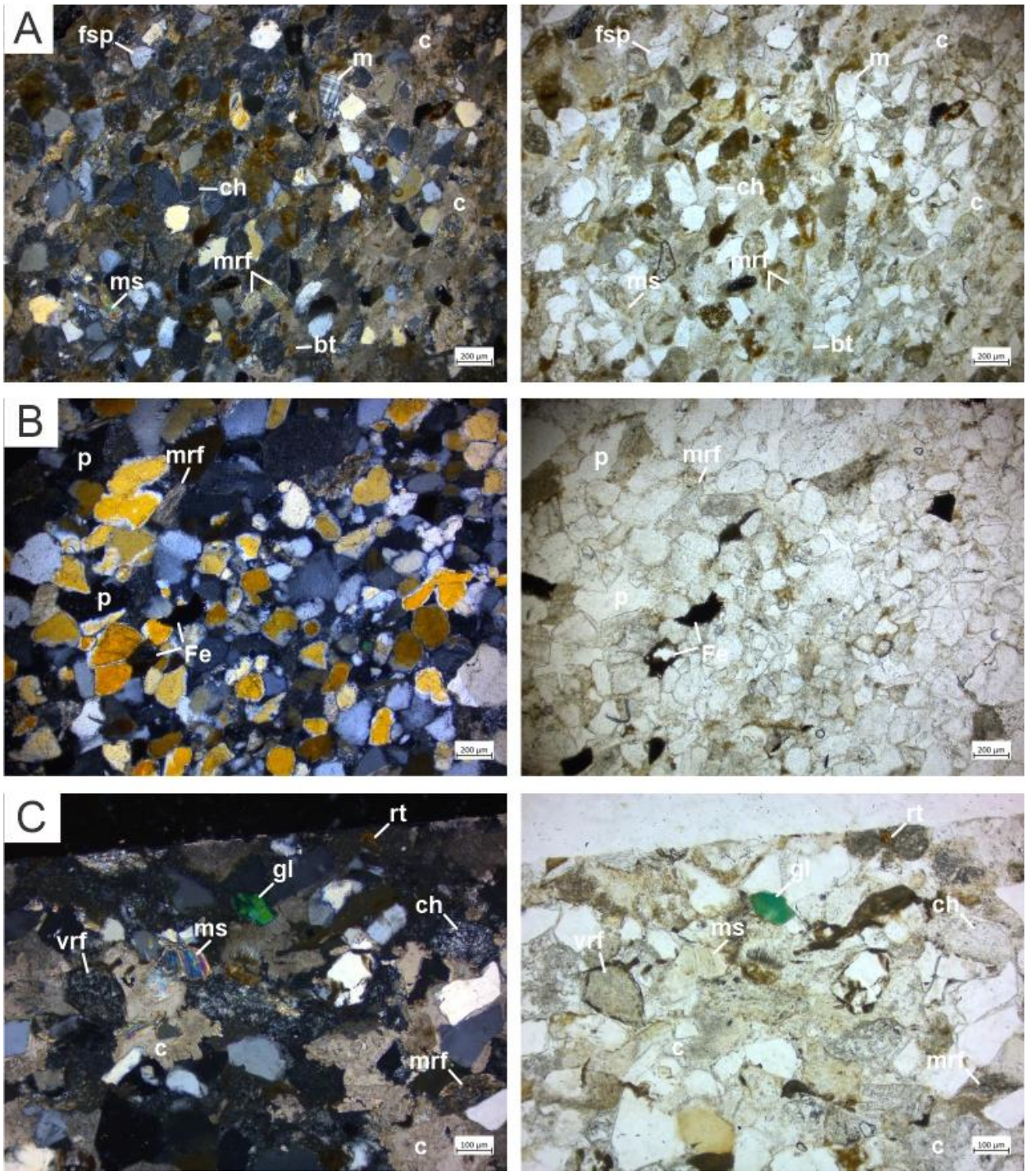

Figure 11. Microphotograph of the upper Precipice Sandstone (TS1-MFS1). Cross-polarised light images are on the left, plane-polarised images are on the right.
Notes: A) Feldspatho-litho-quartzose sandstone. Note the high proportion of matrix and calcitic cementation. Sample KEGW7-P4 (Kenya East GW7, 1173.2 - 1173.25 m). B) Quartzose sandstone. Note higher proportion of matrix compared to quartzose sandstones from the lower Precipice Sandstone. Sample WM1-D2 (West Moonie 1, 2269.5 - 2269.4 m). C) Feldspatho-litho-quartzose sandstone. Note calcitic cementation, Fe oxide rims and a glauconite grain in the top of the photograph. Sample C4-P4 (Chinchilla 4, 1158.6 - 1158.55 m). bt – biotite, c – calcite, ch – chert, Fe – iron oxide, fsp – feldspar, gl – glauconite, m – microcline, mrf – metamorphic rock fragment, ms – muscovite, p – porosity, rt – rutile, vrf – volcanic rock fragment.

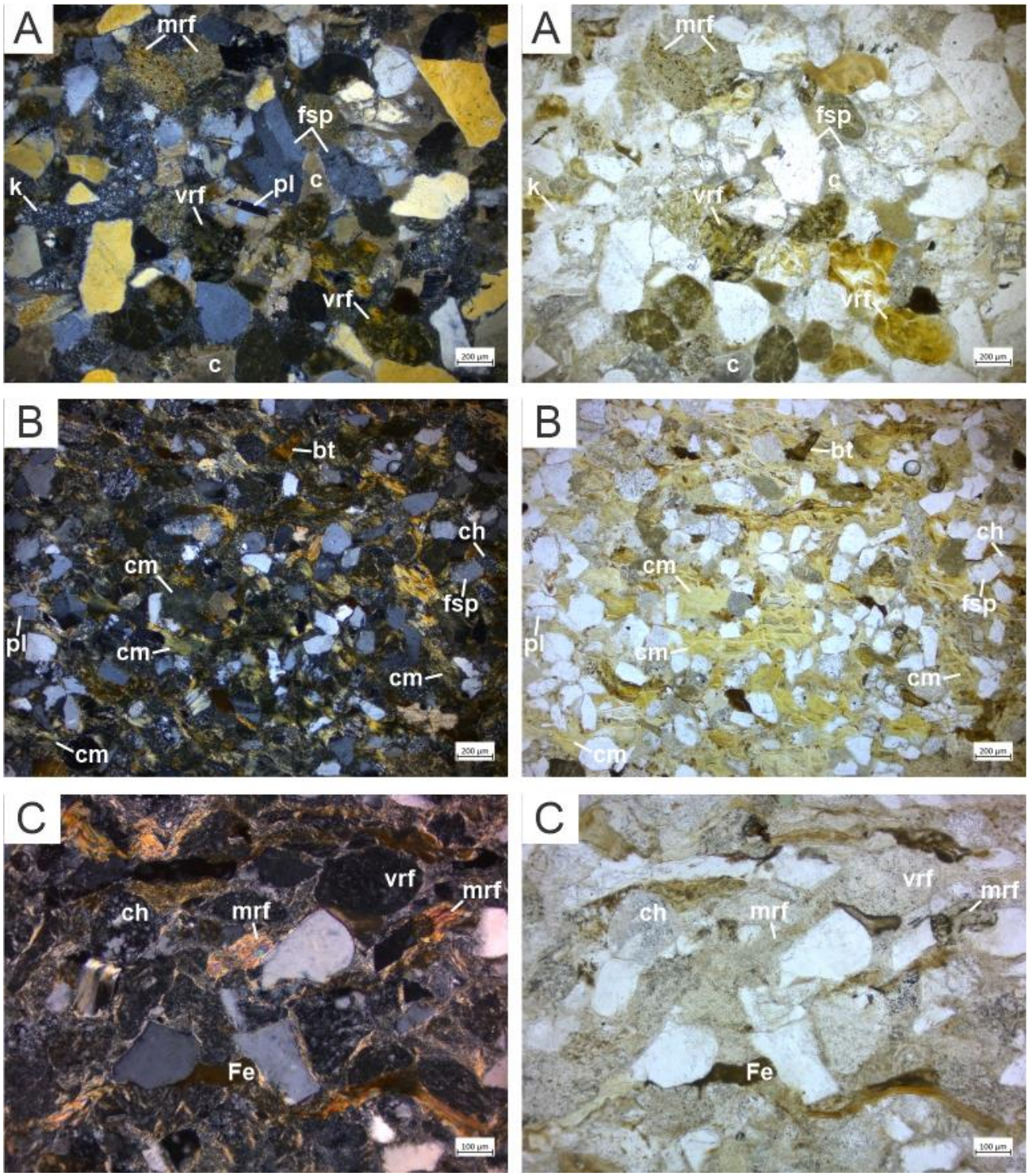

Figure 12. Microphotographs of the Evergreen Formation (MFS1-J30). Cross-polarised light images are on the left, plane-polarised images are on the right.
Notes:A) Feldspatho-litho-quartzose sandstone. Note variable clast rounding. Sample C4-D1 (Chinchilla 4, 1024.45 - 1023.85 m). B) Feldspatho-litho-quartzose sandstone. Note clay mineral cementation. Sample KEGW7-D1 (Kenya East GW7, 994.3 – 993.9 m). C) Feldspatho-litho-quartzose sandstone. Note high proportion of matrix. Sample T17-P1 (Taroom 17, 328.45 - 328.4 m). bt – biotite, c – calcite, ch – chert, cm – clay minerals, Fe – iron oxide, fsp – feldspar, k – kaolinite, mrf – metamorphic rock fragment, pl – plagioclase, vrf – volcanic rock fragment.

3.2 Palaeocurrent analysis

Image log analysis reveals a relatively uniform southward palaeocurrent trend for the lower part of the J10-TS1 interval in six out of eight analysed wells (Figure 13). Trends in West Moonie 1 are more south-westerly than those to the north but there are no nearby wells to corroborate any major shifts to the depositional system. Within the J10-TS1 interval, the clear southward-directed flow pattern in these wells gradually gives way (as one gets higher in the sequence) to more variable palaeocurrent directions. In the upper part of the J10-TS1 interval, a northerly palaeocurrent component is recognisable in all wells but in most of them, it is not dominant. Otherwise, no consistent palaeoflow trend across the study area is apparent for the top part of the J10-TS1 interval. The palaeocurrent reversal occurs at different depths and stratigraphic levels in each well; the change does not appear to correspond to a specific grain size change or well log motif (Figure 14) and requires further study, not only in the Surat but adjacent Jurassic basins. The depths and thicknesses of the interval showing southerly directions versus the interval showing a spread of directions are listed in Table 2. Palaeocurrent directions above TS1 also lack a consistent pattern and vary significantly across the study area (Figure 13).

The two easternmost wells (Hopeland 17 and Tipton 193; Figure 4.) deviate from the southward palaeocurrent pattern for the lower part of the J10-TS1 interval. In Hopeland 17, the entire J10-TS1 interval shows a broad spread of component directions, overall oriented towards the northeast (Figure 13). Above TS1, the pattern becomes more erratic, with no dominant trend. In Tipton 193, easterly to south-easterly trends can be distinguished for the J10-TS1 interval, with a wide spread of component directions. Above TS1, the trend shifts to the northwest and becomes more confined.

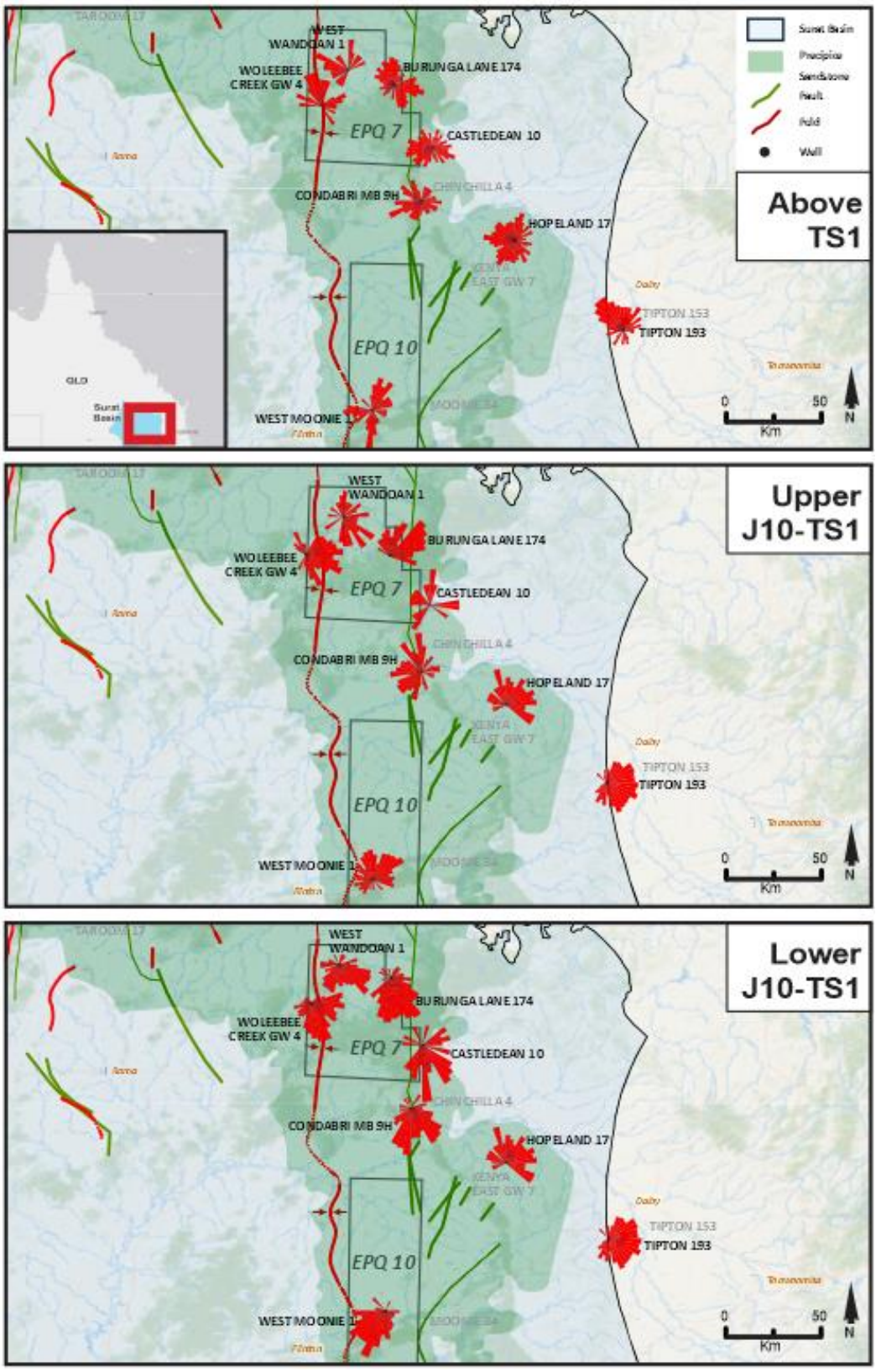

Figure 13. Palaeocurrent patterns determined from image logs for the Precipice Sandstone. For depths of lower and upper J10-TS1 in each well referred to in this figure, see Figure 14. Note that the thinning of the Precipice Sandstone marked in Figure 4 is located east-west along the southern boundary of EPQ7.

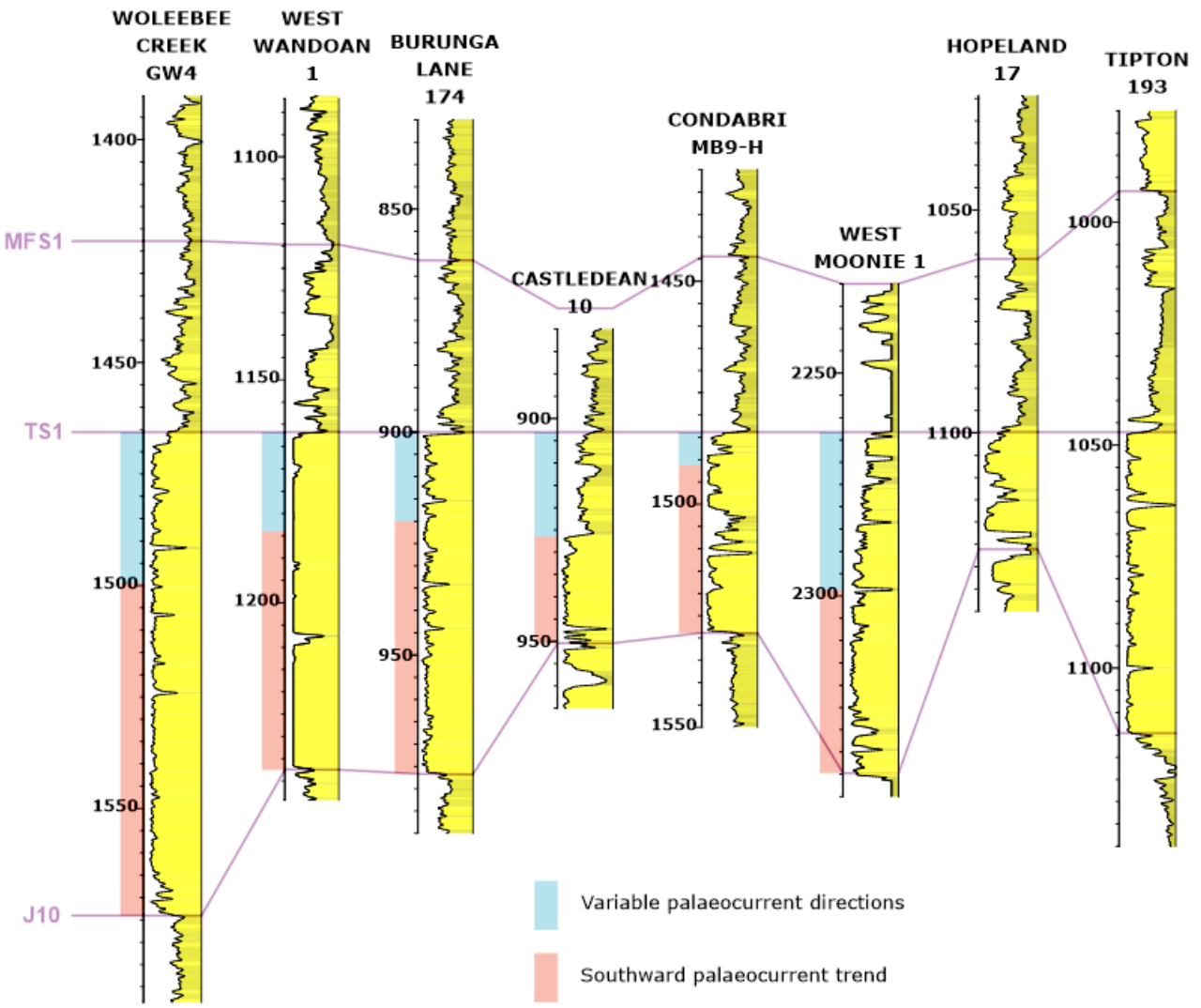

Figure 14. NW to SE oriented cross-section showing wells selected for image log analysis next to the palaeocurrent pattern reversals from each relevant well. Cross-section is flattened on the TS1 surface.

Table 2. Depth and thicknesses of the "blocky sandstone" (J10-TS1) interval showing depth at which a switch in palaeocurrents from southward directed to dispersed occurs.

Well	J10 depth [m]	TS1 depth [m]	J10-TS1 thickness [m]	Depth of palaeocurrent pattern shift [m]	Lower interval thickness [m]	Upper interval thickness [m]
Burunga Lane 174	976.5	900.7	75.8	920	56.5	19.3
Castledean 10	950.1	903.1	23.8	926.3	23.8	23.2
Condabri MB9H	1528.5	1484.1	44.4	1491.3	37.22	31.5
Hopeland 17	1126.8	1100	26.8	n/a	n/a	n/a
Tipton 193	1114.9	1047.1	67.8	n/a	n/a	n/a

West Moonie 1	2340.7	2263	77.7	2299	41.7	36
West Wandoan 1	1237.3	1161.8	75.6	1184	53.3	22.2
Woleebee Creek GW4	1574.1	1465.5	108.6	1499.3	74.8	33.8

3.3 LA-ICP-MS detrital zircon dating

A total of 4314 concordant ages were obtained from 29 samples as part of this study, and West Wandoan 1 and Tipton 153 data from Ciesiolka (2019) were reprocessed and integrated into the dataset for a total of 6754 ages. Detrital age spectra for individual samples are presented on stratigraphic logs in Figure 15. As natural variations in age distributions can be present even within the same stratigraphic unit (e.g., Shaanan et al., 2017; 2019), results from multiple stratigraphically related samples were merged into composite samples to produce a more reliable detrital age signature for each formation (Figure 16).

The detrital zircon age data yielded ages ranging from Early Jurassic (Toarcian) to Palaeoarchean. Eight age populations can be distinguished in the overall age dataset:

- Early Jurassic (175-201 Ma; mainly present above TS1) – 3%
- Permian-Triassic (240-266 Ma) – 6%
- Carboniferous (300-329 Ma) – 4%
- Late Ordovician (450-455 Ma; only present between J10-TS1) – 0.3%
- Pacific-Gondwana ages (~500-650 Ma) – 21%
- Grenvillian ages (~900-1200 Ma) – 22%
- Mesoproterozoic (~1450-1600 Ma) – 7%
- Palaeoproterozoic (~1700-1800 Ma) – 5%

The percentage values are the proportions of each population in the whole dataset for the J10-J30 interval (excluding the four Moolayember Formation samples). The wide spread of detrital ages is consistent with variable zircon grain morphology, ranging from euhedral to well-rounded, and from equant (i.e., length-to-width ratio <<2) to acicular (length-to-width ratio >>2; Figure 17). The degree of rounding increases with zircon age and the acicular morphologies are typically associated with younger ages, especially the Early Jurassic and Permian-Triassic populations. Older grains typically have equant morphologies.

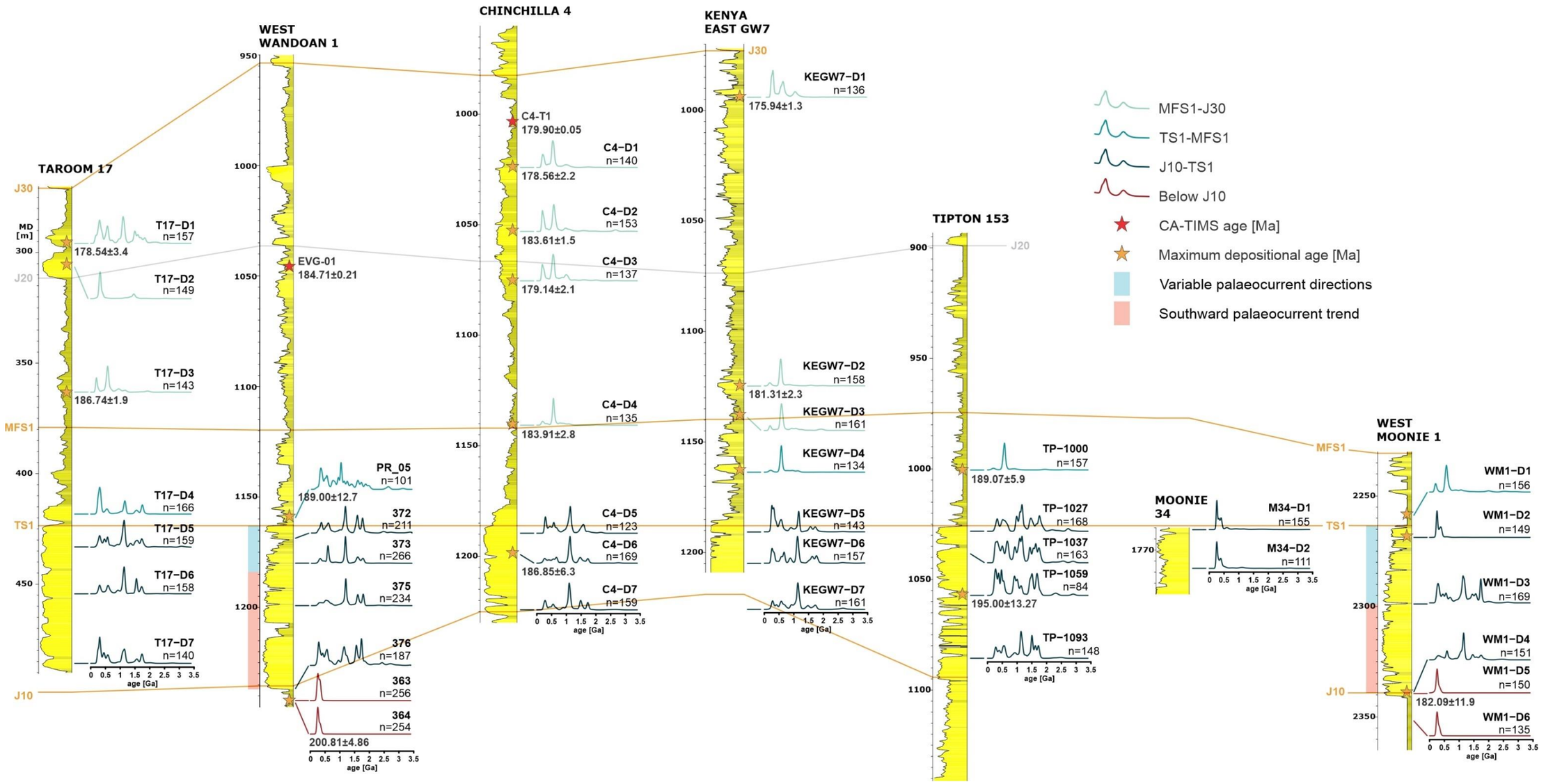

Figure 15. NW to SE oriented cross-section showing U-Pb detrital zircon age spectra (KDE), maximum depositional ages, and CA-TIMS tuff ages. The cross-section is flattened on the TS1 stratigraphic surface. Depths are in measured depth (MD). The MDAs from detrital zircon samples were calculated using maximum likelihood age and youngest single grain methods.

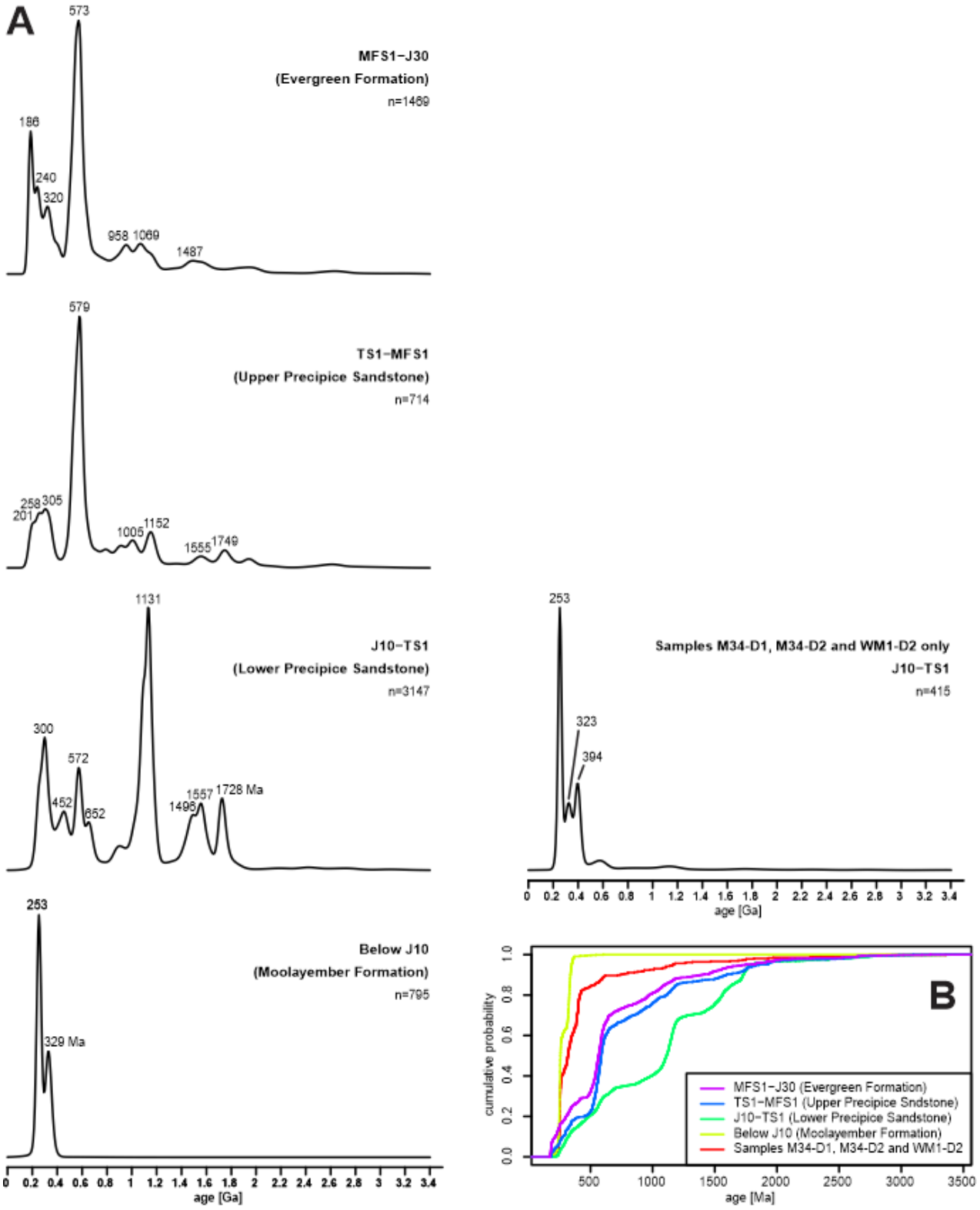

Figure 16. Combined KDEs (A) and CADs (B) for all the detrital zircon analyses arranged by stratigraphic formation (oldest at the bottom). Samples M34-D1, M34-D2 and WM1-D2 were plotted separately on the right as they are outliers.

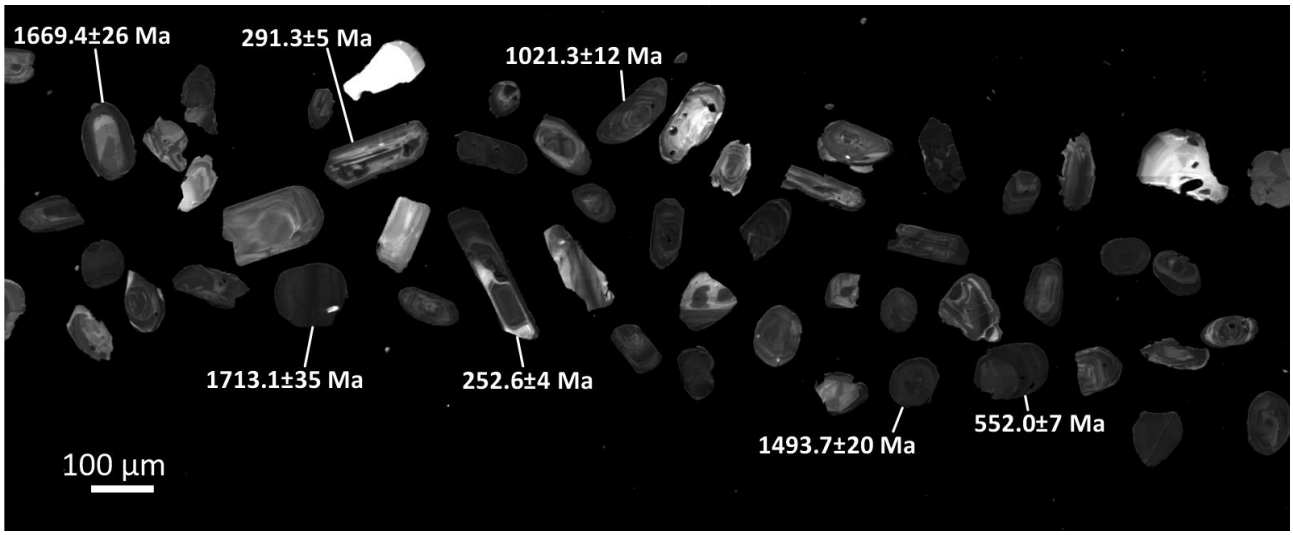

Figure 17. Example SEM-CL images of detrital zircon grains from sample C4-D7 showing variable grain morphology and rounding.

The dataset reveals noticeable stratigraphy-dependent changes in age signatures across the interval of interest, yet relatively few lateral differences among the studied locations in the basin. The Moolayember Formation shows a simple age pattern with only the Permian-Triassic (dominant) and Carboniferous populations present (Figure 16). Above the J10 surface, an abrupt change is observed into a complex age pattern where all the age populations listed above, except for the youngest, form prominent peaks. In most wells, the J10-TS1 interval is dominated by Grenvillian ages (900-1200 Ma), with prominent Permian-Triassic, Carboniferous and Pacific Gondwana populations, and the other populations forming smaller age peaks. Subtle and gradual changes in age signatures can be distinguished within the Precipice-Evergreen interval. Above the TS1 surface, the Pacific Gondwana population becomes dominant, whereas the rest of the ages, especially the Grenvillian population, become less prominent. A small Early Jurassic peak appears that was absent in the interval below. The MFS1-J30 interval is still dominated by the Pacific Gondwana population, with even fewer older ages and a larger proportion of Early Jurassic ages. The youngest age population in this interval consists of younger ages than in the underlying section (peaking at 186 Ma versus 201 Ma). A characteristic feature of the succession as a whole is that it is nearly devoid of any grains older than ~1800 Ma.

The detrital zircon patterns for a given stratigraphic interval are very similar across the study area, with the lowermost section of the J10-TS1 interval, as well as the whole TS1-J30 interval, showing uniform age distributions in both the northern and southern hypothesised depocentre (Figure 15). One notable difference in terms of regional variations is observed in the upper section of the J10-TS1 interval, where the age distributions in the south (Moonie 34 and West Moonie 1; Figure 4) differ from the rest of the basin. In the south, the section just below TS1 is characterised by a dominant Permian-Triassic peak, a smaller Carboniferous peak and a lack of virtually any ages older than ~400 Ma – an age signature characteristic of the Moolayember Formation (Figure 16). In contrast to the Moolayember Formation, however, this sample group shows an additional distinct Early-Middle Devonian (389-399 Ma) population that is not recognised in any other samples in this study. As evident in West Moonie 1 (representing the southern potential depocentre), the change in detrital age pattern occurs as the palaeocurrent trend transitions from southward to northward. In contrast, in the north, the shift in palaeocurrent directions discussed in Section 3.2 is not accompanied by any changes in detrital ages, based on the West Wandoan 1 data (Figure 18). Alternative hypotheses to explain this peculiar trend are changes in depositional environment between the south and north, or the reactivation of faults in the south which does not affect the north in the same way. Above the TS1 surface, the age pattern variations do not show any distinct area-dependent trends.

The stratigraphic and lateral trends in provenance are illustrated on the multidimensional scaling plot (MDS; Figure 19). Moolayember Formation samples form a tight cluster on the right, as do the J10-TS1 interval samples on the top left, except the outlier samples mentioned above from the southern depocentre just below the TS1 surface (samples M34-D1, M34-D2 and WM1-D2). The MFS1-J30 samples also form a cluster, although not as distinct. Samples from the TS1-MFS1 interval in between show relatively little affinity to each other, with some plotting within the J10-TS1 cluster and some within the MFS1-J30 cluster. Other outliers include two topmost samples from Taroom 17 that plot closer to the J10-TS1 cluster rather than to the stratigraphically related samples from the MFS1-J30 interval.

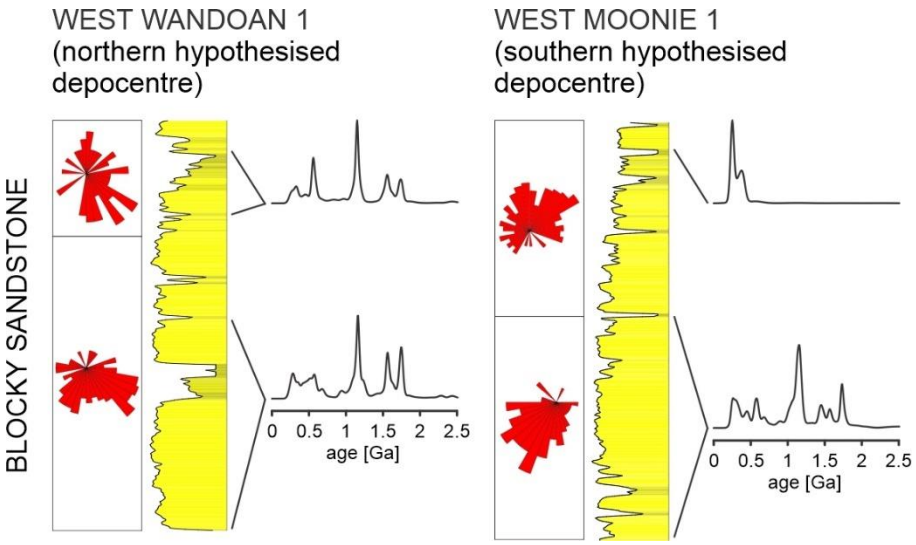

Figure 18. Detrital age distributions and palaeocurrent patterns in the J10-TS1 interval compared for West Wandoan 1 (northern hypothesised depocentre) and West Moonie 1 (southern depocentre). These are the only two wells in the study with both core and image log data available.

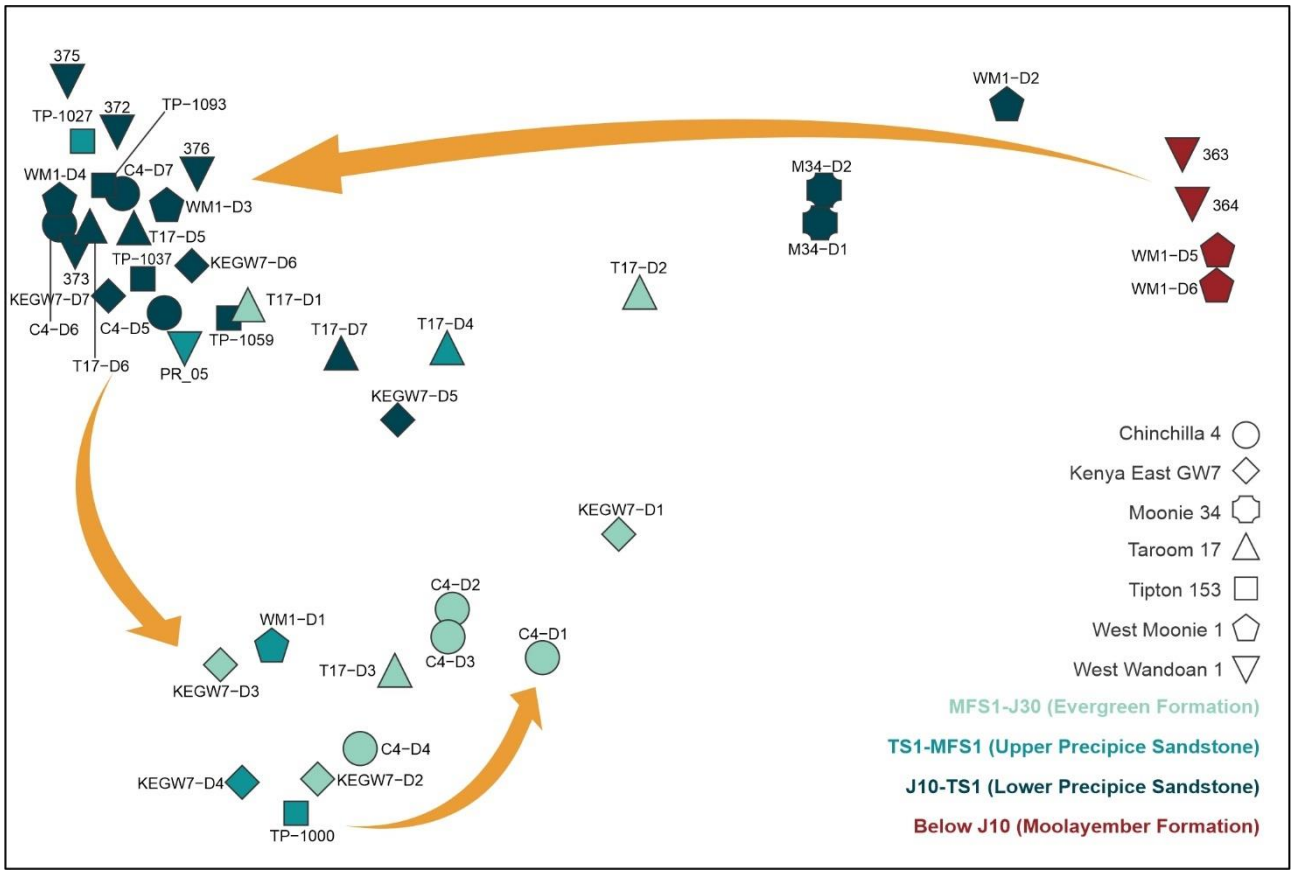

Figure 19. Multidimensional scaling plot of detrital zircon analyses.

3.4 CA-TIMS dating of tuffs

Three of the four tuffs sampled were regarded as unsuitable for CA-TIMS dating based on preparatory SEM-CL imaging and LA-ICP-MS analysis. Sample KEGW7-T1 yielded no zircon, and samples WM1-T1 and C4-T2 yielded small numbers of zircon grains that were confirmed to be detrital (i.e., recycled from older rocks and, therefore, decoupled from the true depositional age), based on rounded grain morphologies and LA-ICP-MS ages older than Jurassic. This indicates that the three sampled horizons are either heavily recycled ignimbrites or non-volcanic mudstones misidentified as tuffs. The remaining sample C4-T1 (Figure 20), collected ~18 m below the J30 surface in Chinchilla 4 (Figure 15), was confirmed to be tuffaceous. The sample contained >90% syn-depositional volcanic zircon grains, as confirmed by elongated and sharply faceted morphology and bright CL response (Figure 21), as well as preliminary LA-ICP-MS dating of 58 grains that yielded dates from 192±9 to 172±8 Ma. Seven grains were selected for CA-TIMS dating, out of which one grain was interpreted as inherited, and six grains yielded age-equivalent dates (i.e., probability of fit >0.05) with a weighted mean of 179.90±0.05 Ma (Toarcian; error is given at 2σ). This age is considered a high-quality, precise depositional age.

Additionally, an existing CA-TIMS date from Ciesiolka (2019) is incorporated into the dataset. The EVG-01 tuff sample, collected from a coarsening upward succession in the middle of the MFS1-J30 interval in West Wandoan 1 (Figure 15), contained a small number of small zircon grains. Four grains were dated, out of which three grains produced a weighted mean age of 184.71±0.21 Ma (Pliensbachian).

Figure 20. Tuff sample C4-T1 from Chinchilla 4 at 1003.45 m dated at 179.90±0.05 Ma.

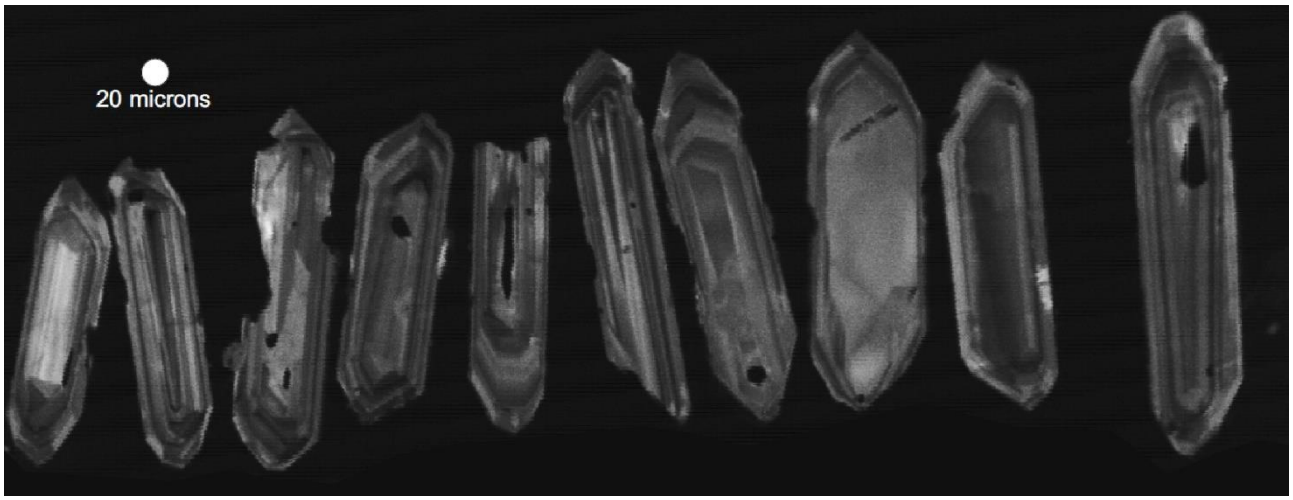

Figure 21. SEM-CL image of volcanic zircons in tuff sample C4-T1.

3.5 Maximum depositional ages from detrital zircon samples

Three methods commonly used over the last decade (Dickinson and Gehrels, 2009), as well as a new method proposed by Vermeesch (2021), are used to calculate maximum depositional ages (MDA) from detrital zircon age suites:

1. Youngest single grain age (YSG; Dickinson and Gehrels, 2009),
2. Weighted mean age of the youngest cluster of 2 or more grain ages overlapping at 1σ uncertainty (YC1σ(2+); Dickinson and Gehrels, 2009),
3. Weighted mean age of the youngest cluster of 3 or more grain ages overlapping at 2σ uncertainty (YC2σ(3+); Dickinson and Gehrels, 2009),
4. Maximum likelihood age (MLA) algorithm (Vermeesch, 2021). The MLA ages are calculated and visualised using radial plots generated in IsoplotR (Figure 22; 0; Vermeesch, 2018). A radial plot is a graphical device designed to visualise datasets with unequal uncertainties.

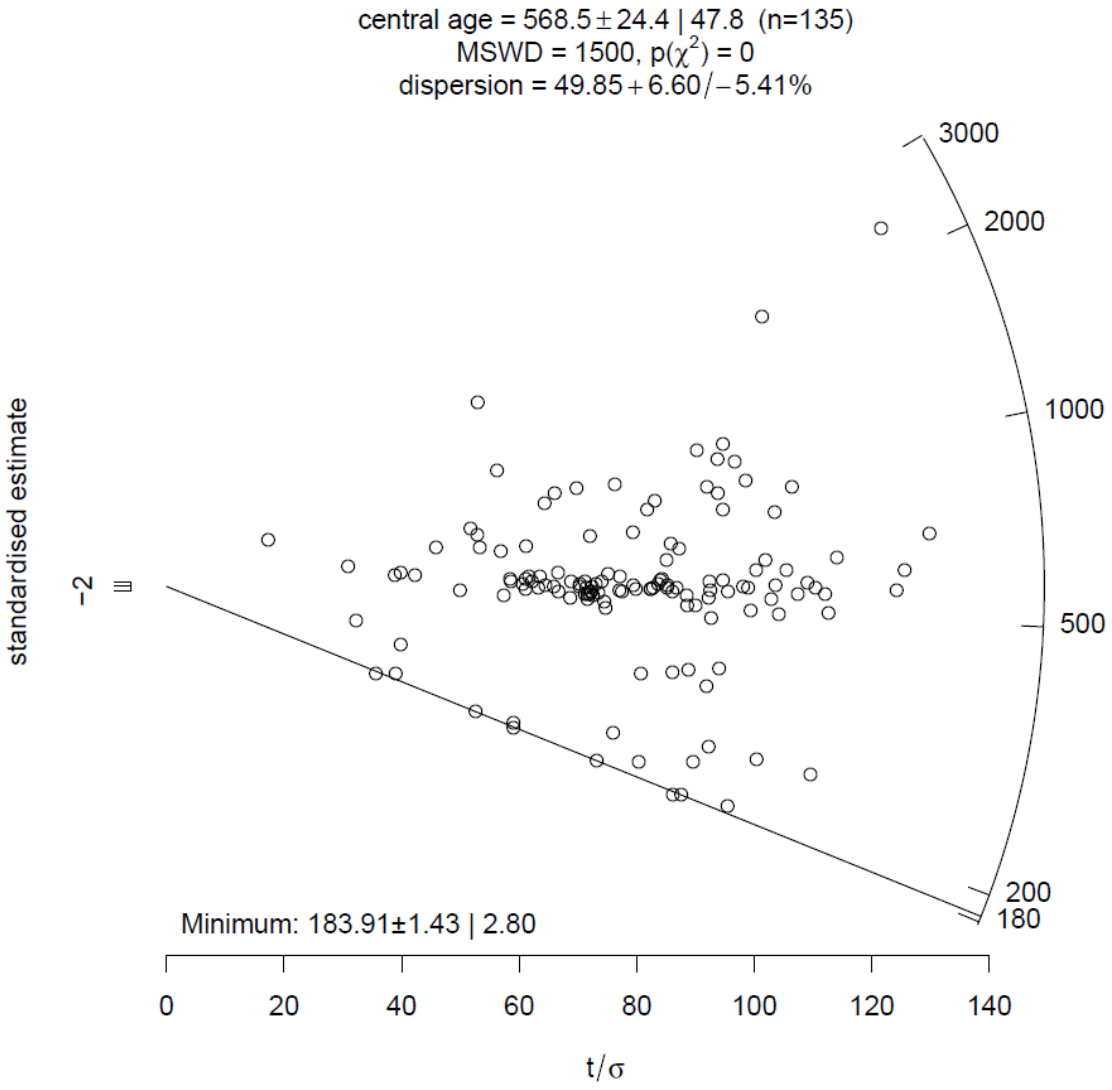

Figure 22. Example of a radial plot (sample C4-D4) used to visualise detrital age distributions and calculate MDA using the MLA algorithm (Vermeesch, 2021). Plot was generated in IsoplotR (Vermeesch, 2018). Uncertainties are given at both 1σ and 2σ.

The YSG method is based on a single data point with high geological and analytical uncertainty and, therefore, should be used with caution. On the other hand, this method has the potential to identify a population of young ages that is too small to be detected when using more conservative methods (e.g., Tucker et al., 2013).

All MDAs are compiled in Table 3 and the radial plots for all samples are shown in 0. Youngest single grain ages are listed for all samples to provide a sense of whether a given sample contains any syn-depositional age component. Based on previous age constraints for the Precipice Sandstone (Price, 1997; McKellar, 1998; Ciesiolka, 2019), ages younger than ~190 Ma and ~201 Ma are considered as approximately syn-depositional for the sections above and below TS1, respectively. Of the forty-one samples analysed, twenty-two did not contain the young component based on YSG ages and, therefore, will not produce meaningful depositional ages (Table 3). In five out of the remaining nineteen samples, the syn-depositional component is present, but the number of young grains is insufficient to be reflected in MDAs calculated using the more conservative

methods, producing MLA ages significantly decoupled from the YSG. Only the remaining fifteen samples, mostly from the MFS1-J30 interval, have the potential to produce statistically robust and geologically meaningful MDAs (marked in blue in Table 3). Maximum depositional ages from the MLA algorithm are favoured over the other methods because they are the most consistent with previous age constraints and the new CA-TIMS date in Chinchilla 4. These ages are graphically illustrated in Figure 15.

The MDAs plotted in Figure 15. range from 200.81±4.86 (Triassic-Jurassic boundary) for the Moolayember Formation to 175.94±1.3 Ma (Toarcian) for the interval close to J30. Within uncertainty, the ages obey the law of superposition in each well, except for sample C4-D2 that yielded an anomalously old age. The J10-TS1 interval dates between the Sinemurian and Pliensbachian and TS1-MFS1 interval yields a Pliensbachian age based on two available MDAs in each interval. The age of the MFS1-J30 interval is constrained based on seven data points and falls within the middle Pliensbachian to topmost Toarcian.

Table 3. Maximum depositional age [Ma] constraints for detrital zircon samples in this study. MLA – maximum likelihood age (Vermeesch, 2021), YSG – youngest single grain age, YC – youngest cluster (Dickinson and Gehrels, 2009). Samples containing syn-depositional age component are shown in bold and samples with MDAs that are believed to be geologically meaningful are additionally shown in blue text.

Stratigraphic interval	Well	Sample	YSG (2σ)	MLA	YC1σ (n=2+)	YC2σ (n=3+)
MFS1-J30	**Chinchilla 4**	**C4-D1**	**175.38±4.2**	**178.56±2.2**	**176.06±1.3 (n=2)**	**177.48±1.9 (n=4)**
MFS1-J30	**Chinchilla 4**	**C4-D2**	**176.31±10**	**183.61±1.5**	**180.43±1.3 (n=6)**	**182.44±1.6 (n=15)**
MFS1-J30	**Chinchilla 4**	**C4-D3**	**170.22±9**	**179.14±2.1**	**–**	**175.88±2.6 (n=7)**
MFS1-J30	**Chinchilla 4**	**C4-D4**	**177.56±10**	**183.91±2.8**	**180.83±1.9 (n=2)**	**182.87±2.2 (n=6)**
J10-TS1	Chinchilla 4	C4-D5	263.74±4.5	n/a	n/a	n/a
J10-TS1	**Chinchilla 4**	**C4-D6**	**184.05±6.9**	**186.85±6.3**	**–**	**–**
J10-TS1	Chinchilla 4	C4-D7	235.16±7.5	n/a	n/a	n/a
MFS1-J30	**Kenya East GW7**	**KEGW7-D1**	**170.91±3.9**	**175.94±1.3**	**171.37±1.6 (n=2)**	**172.34±2.4 (n=4)**
MFS1-J30	**Kenya East GW7**	**KEGW7-D2**	**175.83±7.1**	**181.31±2.3**	**177.54±2.1 (n=3)**	**177.52±4 (n=3)**
MFS1-J30	**Kenya East GW7**	**KEGW7-D3**	**183.78±24.4**	**193.96±7.5**	**188.99±4 (n=8)**	**192.49±6.9 (n=11)**
TS1-MFS1	**Kenya East GW7**	**KEGW7-D4**	**185.92±4.9**	**190.16±2.5**	**–**	**–**
J10-TS1	Kenya East GW7	KEGW7-D5	212.12±8.3	n/a	n/a	n/a
J10-TS1	Kenya East GW7	KEGW7-D6	240.86±8.2	n/a	n/a	n/a
J10-TS1	Kenya East GW7	KEGW7-D7	206±24.2	n/a	n/a	n/a
J10-TS1	Moonie 34	M34-D1	215.81±8.7	n/a	n/a	n/a

J10-TS1	Moonie 34	M34-D2	228.36±11.1	n/a	n/a	n/a
MFS1-J30	Taroom 17	T17-D1	175.71±8.6	178.54±3.4	177.45±1.5 (n=5)	177.45±2.9 (n=5)
MFS1-J30	Taroom 17	T17-D2	179.35±24.8	220.68±14.5	–	–
MFS1-J30	Taroom 17	T17-D3	182.52±5.7	186.74±1.9	184.24±1.3 (n=5)	185.13±2 (n=10)
TS1-MFS1	Taroom 17	T17-D4	210.71±7.8	n/a	n/a	n/a
J10-TS1	Taroom 17	T17-D5	211.66±7.3	n/a	n/a	n/a
J10-TS1	Taroom 17	T17-D6	252.14±7.1	n/a	n/a	n/a
J10-TS1	Taroom 17	T17-D7	230.48±5.4	n/a	n/a	n/a
TS1-MFS1	West Moonie 1	WM1-D1	183.05±24.5	196.09±7.4	185.99±4 (n=8)	188.57±7.2 (n=10)
J10-TS1	West Moonie 1	WM1-D2	184.42±5.6	191.78±6	–	–
J10-TS1	West Moonie 1	WM1-D3	227.97±3.8	n/a	n/a	n/a
J10-TS1	West Moonie 1	WM1-D4	221.13±6.7	n/a	n/a	n/a
Below J10	West Moonie 1	WM1-D5	177.23±22.2	182.09±11.9	181.4±4.9 (n=5)	183.17±8.8 (n=6)
Below J10	West Moonie 1	WM1-D6	219.37±7.1	n/a	n/a	n/a
TS1-MFS1	West Wandoan 1	PR_05	189.19±12	189.00±12.7	–	–
J10-TS1	West Wandoan 1	372	239.9±1.3	n/a	n/a	n/a
J10-TS1	West Wandoan 1	373	231.8±0.7	n/a	n/a	n/a
J10-TS1	West Wandoan 1	375	232±2.4	n/a	n/a	n/a
J10-TS1	West Wandoan 1	376	229.1±1	n/a	n/a	n/a
Below J10	West Wandoan 1	363	217.7±1.5	n/a	n/a	n/a
Below J10	West Wandoan 1	364	183.5±4.4	200.81±4.9	–	–
TS1-MFS1	Tipton 153	TP-1000	181±13	189.07±5.89	183.11±3.65 (n=3)	186.05±5.5 (n=5)
TS1-MFS1	Tipton 153	TP-1027	261.98±14	n/a	n/a	n/a
J10-TS1	Tipton 153	TP-1037	238.46±19	n/a	n/a	n/a
J10-TS1	Tipton 153	TP-1059	194.7±12	195.00±13.27	–	–
J10-TS1	Tipton 153	TP-1093	244.82±10.9	n/a	n/a	n/a

4. Discussion

Detailed sedimentary provenance analysis has been undertaken to aid the assessment of the Precipice Sandstone as a potential CCS reservoir, and the Evergreen Formation as an intraformational seal. The following discussion integrates all datasets to constrain the sourcing and source-to-sink pathways for the lower section of the Surat Basin succession. Particular focus is on identifying any differences between the southern part of the basin where the proposed injection site is located, with the relatively well-studied areas in the north (Figure 1).

4.1 Depositional ages and stratigraphic uncertainty

Despite the multitude of efforts to constrain the stratigraphy of the Precipice Sandstone and Evergreen Formation over the past decades, our data suggest that there is a level of detail concealed within the strata that we cannot yet fully explain. The most common approach has been to consider the interval in terms of lithostratigraphy, establishing “equivalency” of units based on bulk lithological characteristics (Exon, 1976; Gray, 1968; Green, 1997; Mollan et al., 1972; Rigby and Kanstler, 1987). The problematic aspect of the lithostratigraphic approach is that it may not always reflect the age relationships between strata, and potentially results in correlation of time-transgressive sedimentary packages across the basin. This is most clearly demonstrated by the differences between the various published lithostratigraphic columns (e.g., Exon, 1976; McKellar, 1998; Mollan et al., 1972). To overcome the problems with depositional ages, others have used palynostratigraphy to give relative age constraints and demonstrate equivalency of the Precipice-Evergreen interval across parts of the basin (Evans, 1965; 1966; McKellar, 1992; Price, 1997; Reiser and Williams, 1969). Unfortunately, palynostratigraphic zones are of low resolution, often a few million years long, and when compared against the Surat Basin lithostratigraphy, suggest it is diachronous (see data contained within La Croix et al., 2019c).

Most recently, studies have focused on applying sequence stratigraphy, establishing equivalency between strata based on facies stacking patterns and associated shifts in depositional environments controlled by external forcing (i.e., sediment supply, accommodation space) (Hoffmann et al., 2009; Martin et al., 2018; Wang et al., 2019). The problem with the sequence stratigraphic approach is that, in the absence of distinctive seismic reflectors or core material, determining synchronicity of deposition between different parts of the basin based on wireline logs alone, is challenging. These issues are compounded by the fact that sequence stratigraphic packages are known to be spatially variable across vast areas (Gani, 2017), and therefore, differing depositional patterns may be observed in time-equivalent strata due to phase differences in sediment supply versus accommodation (Ainsworth et al., 2020), inherent autogenic processes (Strong and Paola, 2008), or structural controls (Schultz et al., 2020).

So far, no single stratigraphic method has been able to fit every dataset perfectly, such as palynology, seismic, well logs, and in the present study, palaeocurrent analysis and geochronology. Indeed, our palaeocurrent analysis and especially geochronology results suggest we have not yet reconciled the 4-dimensional (3 spatial dimensions plus 1 time dimension) nature of the stratigraphy of the Precipice Sandstone and Evergreen Formation, and variability within and transitions between. The implication of the stratigraphic uncertainty is that comparing sediment transport pathways and sediment provenance between different parts of the basin requires assumptions about equivalency between rock packages and, at present, these cannot be tied to precise geochronological ages that fit all wells in the basin. Nonetheless, our results show that, in general, the sequence stratigraphy put forth by the UQ-SDAAP project is a valid means to compare across such large areas.

Resolving the Precipice-Evergreen stratigraphy using absolute age dating is further complicated by the approach being contingent on the presence of syn-depositional volcanic input into the basin. In geological

settings with persistent proximal volcanism, commonly interbedded tuff horizons provide opportunities for precise age dating and MDAs obtained from detrital geochronology on sandstones can provide robust estimations of depositional ages (e.g., Rainbird et al., 2001; Tucker et al., 2013; Foley et al., 2021b). In this study, chronostratigraphy is only of limited application because of the sparsity of tuff horizons in the Evergreen Formation and their absence in the Precipice Sandstone. The succession is dominated by basement-derived material (see Section 4.3), with reduced volcanic influence, resulting in a low proportion of syn-depositional volcanic zircons in the sandstones. This makes it difficult to capture the young age component despite a large number of analyses per sample.

Nevertheless, the depositional ages from CA-TIMS tuff dating and MDAs from detrital zircon ages obtained in this study and by Ciesiolka (2019) represent significant progress and add resolution to the Surat Basin stratigraphic framework. This is the first geochronological dataset reported for the Precipice Sandstone and some of the first data available for the Evergreen Formation (after an MDA presented by Todd et al., 2019). The ages for the J10-MFS1 interval align with previous broad age constraints from biostratigraphy (Price, 1997) placing the Precipice Sandstone in the Sinemurian to Pliensbachian. The age of the Evergreen Formation is constrained from the middle Pliensbachian to the topmost Toarcian (at least 186.7±1.9-175.9± 1.3 Ma; Figure 15). It could not be verified whether the deposition occurred at the same time in the northern and southern hypothesized depocentres due to the lack of age dating opportunities in either West Moonie 1 or Moonie 34 cores. In the northern part of the study area, the spatial variations in both the CA-TIMS dates and MDAs reveal a diachronicity across the northwest-northeast cross-section. The deposition appears to have occurred earlier in the northwest (Taroom 17 and West Wandoan 1), with the MFS1 surface older than 186.7±1.9 Ma and the TS1 surface dating at approximately 189±12.7 Ma, although the latter date has a large uncertainty. On the eastern side of the Leichhardt-Burunga Fault (Chinchilla 4 and Kenya East GW7; Figure 4), one age from the middle of the blocky sandstone indicates deposition at approximately 186.9±6.3 Ma while the MFS1 surface is only ~183.9±2.8 Ma old. In Tipton 153 at the Surat and Clarence-Moreton Basin boundary, the MDAs are again older, comparable to the northwest. The data reveal that the story is a little more complicated than the general notion that the Precipice Sandstone gradually youngs westward. One potential cause for this depositional age trend may have been topographic relief. If the area around the Undulla Nose formed a topographic high relative to the Mimosa Syncline and Roma Shelf to the west, as well as to the western flank of the Clarence-Moreton Basin to the east, sediment would have been deposited in these areas first. It is also possible that depositional topography was dynamic, and responding to movement on structures within the basin, but this is difficult to constrain with current data.

Given that previous palynostratigraphy places the underlying Moolayember Formation in the Middle Triassic (~247-239 Ma), the MDAs obtained in this study (200.8±4.9 in West Wandoan 1 and 184.1±11.9 in West Moonie 1) are anomalously young, even considering the uncertainties. Based on these two dates, it is likely that the sandstones directly underneath the Precipice Sandstone are, in fact, Eddystone or Chong beds (Price et al., 1985; McKellar, 1998; Green, 1997; Fergusson and Henderson, 2013) and belong to the Surat Basin rather than the Bowen Basin sequence. The interpretation of these two isolated anomalous ages remains unconfirmed at this stage and requires collecting more data from this stratigraphic interval at different locations.

The lack of multiple CA-TIMS dates within one drill core precludes precise estimation of depositional rates.

4.2 Palaeocurrent data

Palaeocurrent patterns in the Precipice Sandstone do not show significant differences between the northern and southern hypothesised depocentres, although it must be noted that image logs were available in only one well in the south (West Moonie 1). The consistent southerly trend observed in the lower section of the J10-TS1 interval and the appearance of a northerly component up-section (Figure 13) are similar to the palaeocurrent patterns reported from outcrop along the northern margin of the basin (Martin, 1980; Bianchi et al., 2018).

Palaeocurrent patterns presented in this study, however, show a much wider dispersal of directions, with easterly, southerly, and south-westerly components present in addition to the northerly trend reported previously for the upper part of the Precipice. Our findings also indicate that the palaeoflow reversal occurs within the J10-TS1 interval rather than above TS1. Further, the stratigraphic position of the reversal is not consistent across the basin with regards to specific changes in grain size or well log motif.

The broadening of dispersal directions is consistent with increasing sinuosity of a river system up-section, possibly in response to rising base level and lowering depositional gradient, as suggested by previous studies (Bianchi et al., 2018; Martin et al., 2018; La Croix et al., 2020). However, such a shift would not cause a regionally persistent reversal in flow direction from south to north. Increasing tidal influence accompanying a base level rise and backstepping the river mouths to estuarine conditions could account for such a change (Bianchi et al., 2018), except one would expect a stronger bimodality in the palaeocurrent directions, and perhaps increased occurrence of suspension fall out or mud drapes as occurs above TS1 that was also accompanied by brackish to marine indicators (Martin et al., 2018). Observations from the top of the blocky sandstone outcropping in Carnarvon Gorge show interference ripples, and thin wavy bedding in the top few metres reminiscent of sandy tidal flats that transition to more open water conditions and deposition of finer-grained suspended load sediments within distributaries and estuaries as MFS1 is approached (after La Croix et al., 2019b, and as illustrated in Figure 6). However, the regional nature of this palaeocurrent reversal would suggest basin-scale transgression well into the southern interior.

Other mechanisms for such a reversal would be a shift in depositional dip to the north, but this would require accompanying uplift in the south of the basin. This should be accompanied by increased sediment influx, and this is not supported by any shift in grain size or change in provenance based on the sandstone petrography and zircon geochronology obtained in this study. The possibility of local movement on the bordering fault systems is possible, but this would shift sediment further basinward rather than towards the north. More information might be gleaned from the two easternmost wells (Hopeland 17 and Tipton 153) that show different sediment transport patterns, which is most likely influenced by their position closer to the eastern boundary of the basin and related to syn-depositional uplift of the New England Orogen and inversion of older fault systems. However, the stratigraphic interval in the Hopeland 17 well is significantly reduced, if not incomplete, and already shows a northward flow direction, so could be correlative with the upper part of the unit. The Tipton 193 well shows a full complement of the blocky Precipice Sandstone, but with a broader dispersal of southerly and northerly flow directions in the lower and upper parts of the J10-TS1 sequence. Although not well constrained, this might suggest rising base levels influenced the south-eastern margin of the basin prior to the interior, and this is at odds, and not well constrained with the age dating. The Tipton 193 well also sits at the boundary to the Clarence Moreton Basin, and the thickness of the interpreted Precipice Sandstone here begs further investigation into the subsurface equivalents to the east.

4.3 Sedimentary provenance

4.3.1 Sandstone compositions

Stratigraphy-dependent variations in sandstone compositions are apparent within individual wells and between wells. The Moolayember Formation is characterised by immature, lithic- and feldspar-rich sandstones in both West Wandoan 1 and West Moonie 1 wells. The lowest section of the Precipice Sandstone (J10-TS1) is uniformly quartz-rich and relatively texturally mature across the study area. In addition to the high quartz content, high compositional maturity is indicated by the virtual lack of feldspars and the precipitation of kaolinite as a product of feldspar weathering. The TS1-MFS1 interval varies in compositions and textural maturity but it is overall more feldspathic and micaceous, and less porous with more authigenic clay minerals present than in the underlying section. The MFS1-J30 interval in the north and east of the study area is characterised by litho-feldspatho-quartzose sandstone compositions. An increase in mineralogical complexity compared to the

underlying Precipice Sandstone is apparent, corroborating the previous petrographic study by Farquhar et al. (2013). Petrography of the MFS1-J30 interval in the southern part of the study area is unknown, as this interval was not cored in either of the wells in the south.

Throughout most of the stratigraphic intervals available for comparison, no significant contrast in sandstone compositions was observed between the northern and southern hypothesised depocentre. An important exception where the lithologies in the south do differ from the north, is the interval just below the TS1 surface (i.e., top of blocky sandstone). In contrast with the clean, quartzose sandstones in the north (West Wandoan 1, Chinchilla 4, etc), the Moonie 34 and West Moonie 1 sandstones from the same interval are less texturally mature and contain more matrix and lithic fragments, including volcanic and volcaniclastic rock fragments (Figure 23). This difference is reflected in detrital zircon signatures and strongly suggests a different sediment provenance.

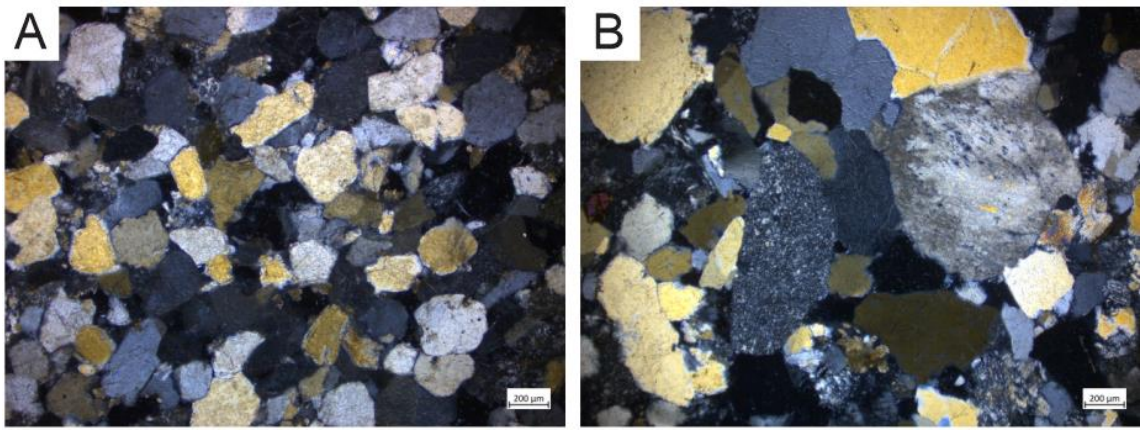

Figure 23. Example microphotographs from the lower Precipice Sandstone just below TS1 surface, compared for the northern (A) and southern (B) hypothesized depocentres.
Notes: A) Medium-grained quartzose sandstone. Sample KEGW-D5. B) Medium- to very coarse-grained, poorly sorted litho-quartzose sandstone. Sample WM1-D2. Both images were taken under cross-polarised light.

Plots of provenance classification following Dickinson and Suczek (1979) and Dickinson et al. (1983) show that the J10-TS1 interval has a craton interior provenance for the bulk of the blocky sandstone (Figure 24), except for the zone just below TS1 in the southern depocentre mentioned above. The lower quartz content in sandstones from this section likely indicates mixed provenance, however, QFL percentages for those samples were not quantified. The quartzose compositions of the lower Precipice Sandstone are in stark contrast with the underlying Moolayember Formation and mark a pronounced shift in sediment provenance across the J10 sequence boundary (base-Surat unconformity). The source of sandstones within the TS1-MFS1 interval varies between continental block and quartzose recycled orogen, while the compositions above MFS1 reflect a mixed provenance. Although some of the samples from the MFS1-J30 interval are of recycled orogen source, the relatively low textural maturity and the presence of feldspar in the grain frameworks indicate only limited sediment recycling. The overall low textural and moderate compositional maturity of this interval, and some of the samples from the TS1-MFS1 interval, suggest shorter sediment transport distances and predominance of a proximal source, compared to the sediment grains below TS1, which are characterised by moderate textural and high compositional maturity, indicating longer transport and more distal sourcing.

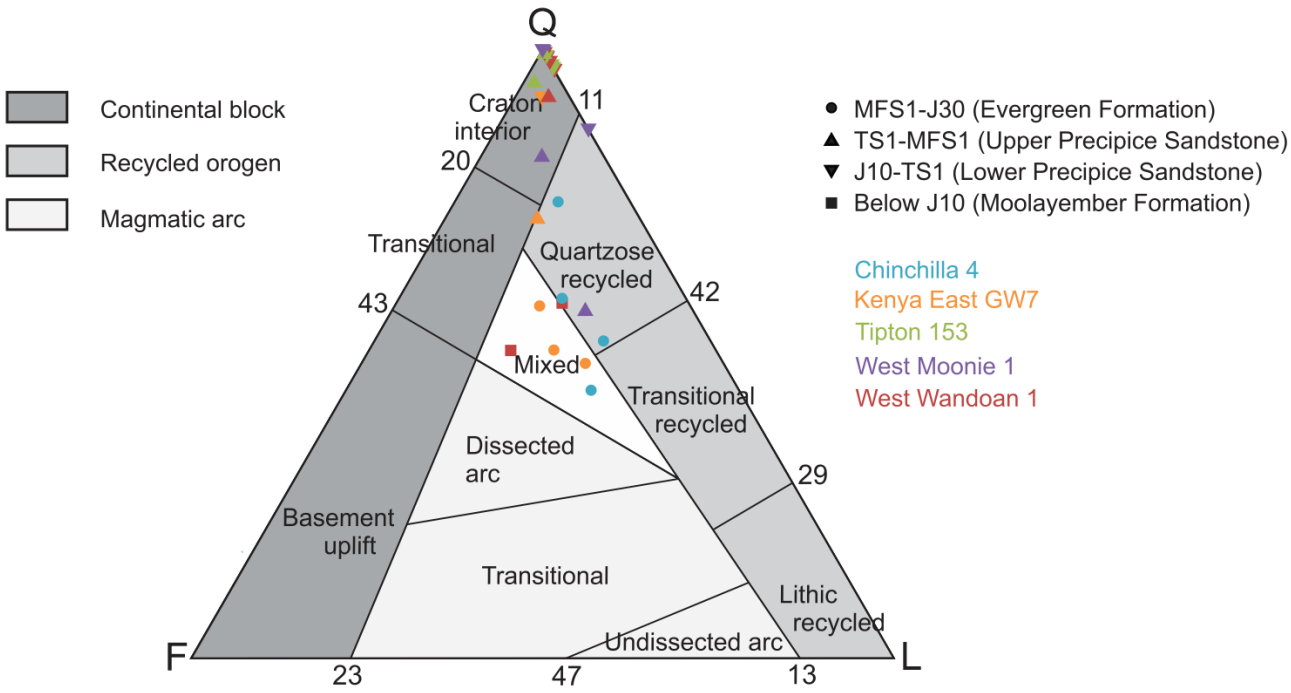

Figure 24. Provenance classification of samples in this study after Dickinson and Suczek (1979) and Dickinson et al. (1983). The Q field contains monocrystalline quartz only, polycrystalline quartz and chert are grouped with lithic fragments.

A variety of lithic grain types were identified in sandstones from the TS1-J30 interval that provide valuable information on the character of the sediment source terranes. The presence of volcanic and volcaniclastic rock fragments, many of which were identified as andesitic, unaltered plagioclase, as well as volcanic quartz (based on clear grains with straight extinction; Krynine, 1946; Basu, 1985), likely indicates sourcing from a hypothesized volcanic arc on the eastern Gondwana margin (e.g., Foley et al., 2020a). Such arc-related volcanic detritus might represent products of contemporaneous volcanism, or alternatively represents eroded material from older volcanic rocks. The abundance of metasedimentary rock fragments likely reflects significant sediment input from low-grade metamorphic basement rocks. Quartzites and metasedimentary rocks form the bulk of the Thomson Orogen basement, which underlies the NW parts of the Surat Basin and the Palaeo- and

Mesozoic basins NW of the Surat Basin (Wade et al., 2005; Raimondo et al., 2010; Walsh et al., 2013; Purdy et al., 2016a), and are likely an important source terrane. Feldspatho-lithic sandstone compositions in eastern Australia have been previously linked to New England Orogen provenance (Green, 1997; Craven and Daczko, 2017; Korsch 1984; Korsch et al., 2009a). The abundance of chert clasts in the Precipice-Evergreen succession likely represents sourcing from the older, inland areas of the New England Orogen, as the presence of chert is typically associated with thrust belt provenance on the outer parts of continental margins (Garzanti et al., 2002; 2013). The variable sandstone compositions are consistent with mixed sediment derivation from both the Thomson and New England orogens.

The presence of glauconite in the upper Precipice Sandstone and the Evergreen Formation (Figure 11C), also previously reported by Farquhar et al. (2013), suggests marine influence on sedimentation following the deposition of the blocky sandstone facies of the lower Precipice Sandstone. This corroborates the recent interpretations of tidal and shallow marine sedimentary facies based on outcrop and core observations (Bianchi et. al., 2018; Martin et al., 2018; La Croix et al., 2019a; 2020).

4.3.2 Detrital zircon geochronology and sediment source types

Detrital zircon geochronology revealed a complex age pattern consisting of multiple distinct age populations (Figure 15, Figure 16), indicating mixed sedimentary provenance for the Precipice-Evergreen succession that cannot be assigned to a single source terrane. This is supported by the wide range of morphologies and degrees of rounding observed in the dated zircon grains (Figure 17). The degree of grain rounding increases with age. Well-rounded grains, which predominate in this dataset, typically have multi-cycle source-to-sink histories and are associated with recycled sources, while angular grains more likely represent first-cycle sedimentary input (e.g., Shaanan and Rosenbaum, 2016). Zircon shape depends on crystallisation velocity, where rapid crystallisation usually results in acicular zircon morphologies (i.e., length-to-width ratio >>2) and slowly cooling magmas typically produce equant grains (length-to-width ratio <2; e.g., Corfu et al., 2003). Elongated zircons were, therefore, interpreted as volcanic, while equant grains indicate plutonic origin. Acicular grains were rare within the studied dataset and almost exclusively associated with young ages (<265 Ma). Based on the zircon age populations and grain morphologies, supported by petrographic characteristics of the sandstones, three broad types of sediment sourcing can be distinguished:

1. Recycled sedimentary and metasedimentary basement rocks (Pacific-Gondwana, Grenvillian, Meso- and Palaeoproterozoic populations). The older (>500 Ma) part of the Surat Basin age spectra likely represents material that has undergone multiple cycles of erosion, transport and redeposition. The multi-cycle character of these age populations is consistent with predominantly well-rounded zircon grains and indicates sourcing from recycled sedimentary or metasedimentary basement rocks, rather than directly from plutonic or volcanic source terranes. The abundance of metasedimentary rock fragments in many sandstone samples is consistent with low-grade metamorphic basement sourcing. This is the dominant source type for the Precipice-Evergreen succession (55% of the overall dataset).

2. Plutonic and volcanic basement rocks (Permian-Triassic, Carboniferous, Middle Devonian and Late Ordovician populations). The Ordovician to Triassic zircons are believed to represent material sourced mostly from igneous terranes. The Tasmanides, which form the basement of the eastern Australian Mesozoic sedimentary basins, underwent multiple extensional periods accompanied by widespread magmatism. As a result, the Tasmanides basement is intruded by abundant granites and granodiorites, as well as interlayered with volcanic rocks of various compositions and ages (e.g., Bryan et al., 2003; 2004; Draper, 2006; Fergusson et al., 2007; Glen et al., 2011; Brown et al., 2012; Li et al., 2012; Donchak et al., 2013; Fergusson and Henderson, 2013; Fraser et al., 2014; Purdy et al., 2016a; 2018; Fergusson, 2017; Cross et al., 2018; Shaanan et al., 2017;

Rosenbaum, 2018; Siégel et al., 2018; Jessop et al., 2019). Sensitive high-resolution ion microprobe (SHRIMP) ages of many of these igneous suites are publicly available and include multiple Palaeozoic to early Mesozoic rock associations that are likely sources for the respective age populations in the upper Bowen Basin to lower Surat Basin sedimentary succession. Variable rounding of the Palaeozoic and Triassic zircon grains reflects various degrees of reworking of this igneous material prior to the deposition in the Surat Basin. The Palaeozoic to Early Triassic ages represent approximately 10% of the overall dataset.

3. Contemporaneous volcanism (<201 Ma ages). The youngest Early Jurassic population, mainly present in the TS1-J30 interval, becomes progressively younger up-section and reflects input from syn-depositional or close to syn-depositional volcanism. This is consistent with the abundance of volcanic and volcaniclastic rock fragments in the TS1-J30 interval, as well as a high proportion of angular, volcanic zircon grains. Although the young ages form a prominent peak in the detrital age spectra, this source type represents only 3% of the overall dataset.

4.3.3 The Tasmanides as a source region for the Precipice Sandstone-Evergreen Formation succession: tectonic implications

The Surat Basin formed at the junction of the Thomson, Lachlan, and New England orogens (Figure 2). Metamorphic, granitic, and volcanic suites within these basement blocks are potential sediment sources for the age populations recorded in the Precipice-Evergreen Formation succession. Typical detrital age signatures for all five blocks of the Tasmanides, plotted from a compiled large published dataset (Shaanan et al., 2017), are shown in Figure 25. The Thomson Orogen is dominated by low-grade metasedimentary rocks and extends from the northeast of the Mimosa Syncline across a large portion of eastern Australia (e.g., Brown et al., 2012; Fergusson and Henderson, 2013; Purdy et al., 2016a; Cross et al., 2018). The Thomson Orogen metasediments are intruded by abundant granites and granodiorites, as well as interlayered with volcanic rocks of various compositions and ages (e.g., Draper, 2006; Fergusson et al., 2007; Brown et al., 2012; Fergusson and Henderson, 2013; Purdy et al., 2016a; 2018; Cross et al., 2018; Siégel et al., 2018). Age signatures of many of these basement metamorphic and igneous suites have been recognised in overlying Palaeozoic basins, such as the Adavale and Drummond basins (e.g., Purdy et al., 2016a; Asmussen et al., 2018; Sobczak, 2019). Except for minor outcrops in the Anakie, Charters Towers and Greenvale blocks (Figure 2), the Thomson Orogen is largely confined to the subsurface. The detrital age signature compiled for the orogen is characterised by two major age populations, Pacific-Gondwanan and Grenvillian (Figure 25; Purdy et al., 2016a; Shaanan et al., 2017). The proportions of the two populations vary across the metasedimentary suites. The age pattern dominated by the 560-600 Ma ages with a smaller proportion of Grenvillian ages has been recognised throughout the Thomson Orogen, as well as other parts of eastern Australia, central Australia and Antarctica, and has been termed the ‘Pacific-Gondwana detrital zircon signature’ (Purdy et al., 2016a). The age pattern dominated by the Grenvillian population, with far lesser or no Pacific Gondwanan ages, is referred to as the ‘Syn-Petermann’ signature. This pattern has been recognised from several scattered locations across the Thomson Orogen and has been interpreted to represent a central Australian proto-source that was uplifted during the Petermann Orogeny (570-530 Ma; Camacho et al., 2002; Fergusson et al., 2007; Maidment et al., 2007) and shed sedimentary material towards eastern Australia (Purdy et al., 2016a). The Thomson and Delamerian fold belts are often considered to be part of the same tectonic domain. The boundary between the two fold belts is poorly defined, and they are characterised by a remarkable similarity of lithologies and detrital age signatures (Figure 25; Shaanan et al., 2017; 2019; Rosenbaum, 2018).

The Lachlan Orogen to the south and southwest of the Surat Basin is also largely covered by younger sedimentary basins and outcrop is spatially limited. Sedimentation within and deformation of the orogen occurred between the Cambrian and Carboniferous (e.g., Glen et al., 2011; 2013; Fergusson, 2017). The detrital age spectra compiled for the Lachlan Fold Belt show a dominant population at 490-530 Ma and a

smaller Grenvillian population. The Grenvillian ages in the Lachlan Orogen peak at approximately 1050 Ma, which is younger than the Grenvillian population of the Thomson Orogen (Figure 25).

The New England Orogen represents the youngest and most complex building block of the Tasmanides and comprises multiply deformed, Silurian to Upper Triassic igneous, metamorphic, and sedimentary rocks (Aitchison, 1990; Donchak et al., 2013). The history of the New England Orogen and its structural elements is related to the convergent margin tectonics on the eastern Gondwana margin, particularly during the Permian-Triassic Hunter-Bowen Orogeny (e.g., Donchak et al., 2013; Rosenbaum, 2018). The dated clastic sedimentary rocks of the New England Orogen display a simple, unimodal age distribution peaking in the middle Carboniferous, with very few older ages (e.g., Shaanan et al., 2017; Korsch et al., 2009a; Figure 25).

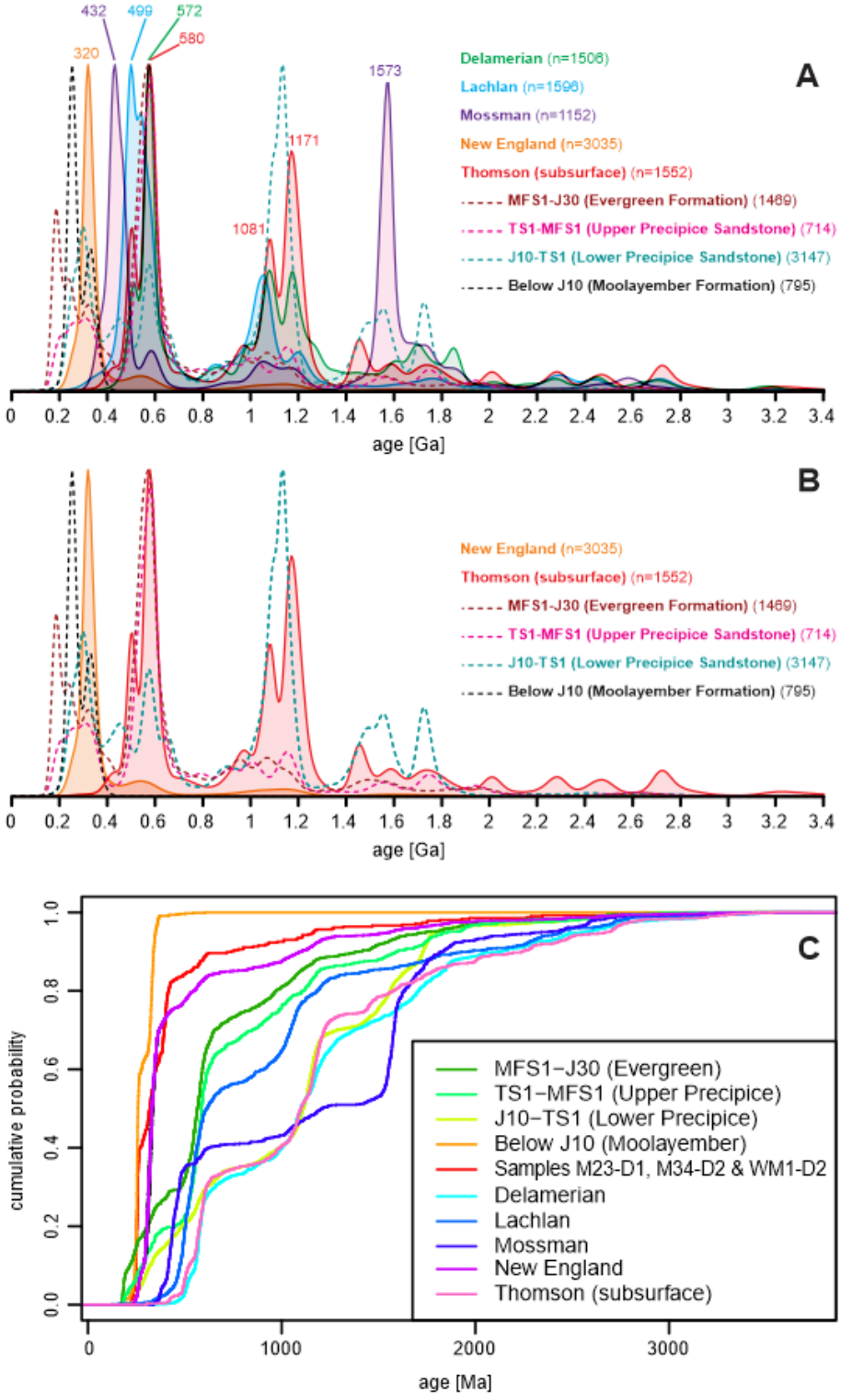

Figure 25. Typical detrital age signatures of the Tasmanides overlaid on the age spectra from this study. Notes: A) KDEs for each of the five building blocks of the Tasmanides. B) For clarity, only the two orogens believed to be the main source terranes for the analysed Bowen and Surat Basin formations are shown. C) Same dataset shown as CAD. Based on detrital zircon U-Pb dataset compiled by Shaanan et al. (2017). Individual data sources are referenced therein.

The diversity of zircon populations, the sandstone compositions, as well as the variations in palaeocurrent directions, point to an extensive and diverse source region within the Tasmanides. All datasets are integrated to provide constraints on the location and extent of the source region, as well as the specific component sources for the provenance groupings identified in Section 4.3.2.

Based on the prominent Pacific Gondwanan and Grenvillian populations throughout the J10-J30 interval of the Precipice Sandstone (Figure 25), the Precambrian part of the age spectra is interpreted to have been sourced predominantly from the Thomson Orogen basement. The age profile of the J10-TS1 interval resembles the Syn-Petermann signature characteristic of several metasedimentary and metavolcanic suites within the Anakie and Charters Towers provinces (such as the Cape River, Argentine, Running River and Bathampton Metamorphics), as well as the Nebine Metamorphics within the Nebine Ridge (Fergusson et al., 2001; 2007; Kositcin et al., 2015; Purdy et al., 2016a). Figure 26 shows that the proportions of the Grenvillian, Pacific-Gondwanan and Palaeo-Mesoproterozoic age peaks in the lower Precipice Sandstone (J10-TS1 interval) closely match the age distributions of the Nebine Metamorphics and combined units of the Anakie Inlier. These source terranes are located to the north and northwest of the Surat Basin (Figure 2) and are consistent with the southerly and south-easterly palaeocurrent directions for the lowest section of the Precipice Sandstone reported here and in previous studies (Martin, 1980; Bianchi et al., 2017; 2018; La Croix et al., 2020). This suggests that all or some of these basement blocks were elevated and eroded at the time of the deposition in the Surat Basin, contrary to previous views that the Nebine Ridge was not exposed during the Early Jurassic (Exon, 1976; Martin, 1980). A Thomson Orogen sediment source has also been suggested by Ciesiolka (2019).

The age spectra of the TS1-J30 interval display a strong Pacific Gondwanan signature, which most closely resembles the Thomson Beds (Figure 26, Figure 2) – a metasedimentary unit widely distributed throughout the central Thomson Orogen, as well as in the Roma Shelf (Purdy et al., 2016a). Erosion and substantial sediment input from the Thomson Beds are probable, as this basement unit directly underlies the western part of the Surat Basin as well as the areas directly west, northwest, and southwest of the basin. At the time of the deposition of the Precipice Sandstone, these areas were likely exposed as they had not yet been covered by the Jurassic-Cretaceous Eromanga Basin and only partly covered by the Palaeozoic Adavale and Drummond basins. Other rock units characterised by the Pacific Gondwanan ages include the Timbury Hills Formation of the Roma Shelf, the Seventy Mile Range Group in the Charters Towers Province, and Les Jumelles Beds and Wynyard Metamorphics of the Anakie Province (Fergusson et al., 2007; Kositcin et al., 2015; Purdy et al., 2016a; Siégel et al., 2017). Overall, however, the Charters Towers and Anakie blocks are dominated by the Syn-Petermann age signature. The decrease of the proportion of Grenvillian and Palaeo-Mesoproterozoic ages up-section in the Precipice-Evergreen succession, and the simultaneous increase of the Pacific-Gondwana population, might indicate decreasing influence of the Charters Towers and Anakie Block sourcing over time, while relatively more proximal sourcing from the Roma Shelf and central Thomson Orogen intensified.

The age signature of the Delamerian Orogen further to the west also largely overlaps with the older part of the Surat Basin age spectra (Figure 25). However, the Delamerian Orogen age signature is indistinguishable from the Thomson Orogen. Since the Thomson Orogen lies directly underneath the basin, it is a more likely source terrane than the far-field Delamerian Orogen (Figure 2).

The small 450-455 Ma population from the J10-TS1 interval likely represents material derived from younger igneous rocks intruding the Thomson Orogen metasedimentary basement. Upper Ordovician granites with available SHRIMP U-Pb ages that were likely exposed at the time and contributed to the sedimentation in the Surat Basin are the Granite Springs Granite of the Eulo Ridge (Cross et al., 2018; Purdy et al., 2016b; 2018), Fat Hen Creek Complex of the Charters Towers Province (Cross et al., 2018), and an unnamed granite suite north of the Nebine Ridge (Siégel et al., 2018; Table 4).

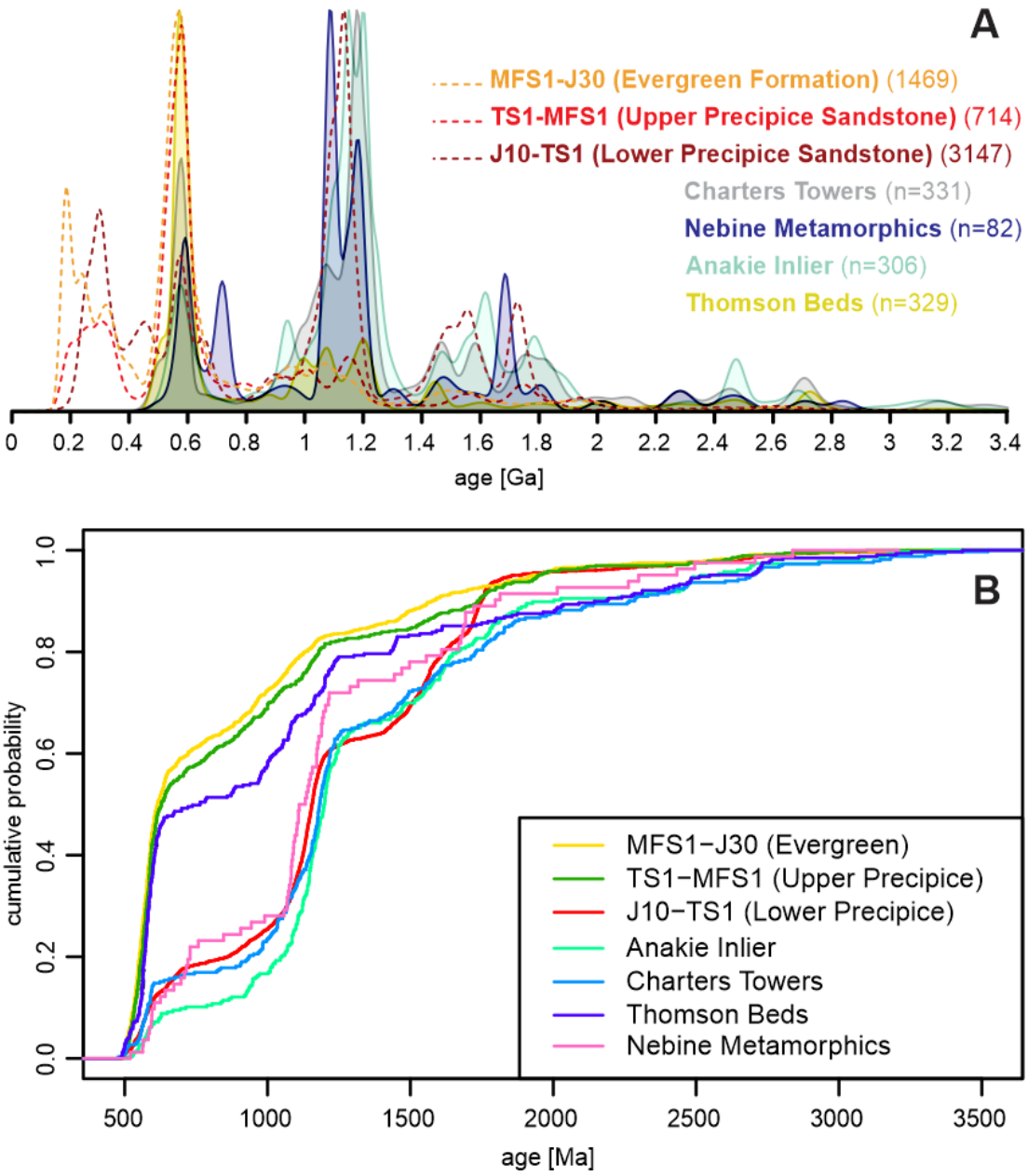

Figure 26. Typical detrital age signatures (A – KDE, B – CAD) of selected units within the Thomson Orogen overlaid on the age spectra from this study. Based on detrital zircon U-Pb data from Purdy et al. (2016a) and Shaanan et al. (2017).

The southerly palaeocurrent directions for the lower part of the J10-TS1 interval are inconsistent with sourcing from either the Delamerian or Lachlan orogens. While a northerly palaeoflow component appears higher in the stratigraphic section, especially along the outcrop belt in the north (Martin, 1980; Bianchi et al., 2017; 2018; Figure 13), indicating some sediment input from the south, the detrital zircon ages are incompatible with any substantial sourcing from the Lachlan Orogen. The Lachlan Orogen detrital age profile is dominated by a 490-530 Ma population (Shaanan et al., 2017), while zircons of this age are sparse in the Precipice Sandstone-Evergreen Formation succession (Figure 25). The exact range of Grenvillian ages in the Surat Basin succession (~1070-1190 Ma) is also more consistent with the Thomson Orogen age signature than with the Lachlan Orogen. The younger igneous rocks intruding the Lachlan Orogen basement are predominantly

Ordovician to Early Devonian (e.g., Rosenbaum, 2018) and this period is also underrepresented in the Surat Basin age spectra.

The dispersion of palaeocurrent directions and appearance of the northerly component in the upper part of the blocky sandstone was triggered either by syn-depositional tectonism or changes in the depositional environment. Any tectonic triggers would have involved tilting of the area towards the north, yet no significant erosion and sediment transport from the Lachlan Orogen to the south is evident. The southern sediment source indicated by the palaeoflow directions must have been located closer to the basin, either in the proximal New England Orogen or recycled locally from the Bowen Basin and/or Surat Basin itself. Moreover, syn-depositional tectonic uplift would typically have been accompanied by a provenance change and a shift to coarser-grained, proximal sedimentary facies due to rejuvenation of the source terrain. The J10-J30 succession, however, shows an overall fining-upward trend and a transition to a lower-energy environment. A provenance shift is indeed observed in West Moonie 1 in the south, but not in any of the wells in the north (Figure 15 and Figure 18). This implies that the shift in palaeocurrent, at least in the northern part of the basin, was more likely a function of the depositional environment and supports the notion of a braided and meandering fluvial setting being influenced by a base level rise and marine processes, as recently suggested by Bianchi et al. (2018) and Martin et al., (2018). An important implication of this multi-method study for sedimentary provenance analysis is that in some cases, shifts in palaeocurrent directions are not indicative of a provenance change and can be independent of variations in detrital age patterns and sandstone compositions.

No Thomson Orogen provenance is evident for the underlying Moolayember Formation, given the lack of zircon ages older than Carboniferous (Figure 25). The Moolayember Formation, deposited in a fast-subsiding foreland setting, is believed to be derived entirely from the New England Orogen to the east of the Bowen Basin (Green, 1997; Fielding et al., 2000). The influx of sediment sourced from the Thomson Orogen began abruptly with the deposition of the Precipice Sandstone, marking a major provenance change in the area. The provenance shift was triggered by the Middle-Late Triassic Goondiwindi Event. This complex contractional event at the climax of the Hunter-Bowen Orogeny terminated the deposition in the Bowen Basin, causing inversion and uplift in many areas across the basin and resulting in a significant unconformity between the Bowen and Surat Basin successions (Korsch et al., 1998; 2009b).

Sediment input from the New England Orogen is believed to have continued during the deposition of the Precipice-Evergreen succession, in addition to the dominant Thomson Orogen sourcing. The middle to late Carboniferous age population in the J10-J30 interval matches closely with the main age peak in the compiled detrital dataset for the New England Orogen (Figure 25). Additionally, numerous Carboniferous to Triassic granitic intrusions and volcanic suites, as indicated by SHRIMP U-Pb dating, are known from various locations across the New England Orogen (e.g., Bryan et al., 2003; 2004; Li et al., 2012; Donchak et al., 2013; Shaanan et al., 2017; Rosenbaum, 2018; Jessop et al., 2019). Potential igneous source terranes and their ages are listed in Table 4. Granitic and volcanic rocks whose ages correspond to the Carboniferous detrital population in the Surat Basin are located in the north of the orogen, while terranes represented by the Permian-Triassic population are mainly in the southern part of the orogen. Based on the changing proportions of these two age populations over time in the J10-J30 succession (Figure 16), the southern New England Orogen source increased as sedimentation progressed, while the northern New England Orogen source decreased. This is consistent with the shifting palaeocurrent patterns and the notion of the northerly palaeoflow component representing local sourcing from the southern New England Orogen directly south and southeast of the basin, rather than from the Lachlan Orogen further south. Many of the northern New England Orogen Carboniferous igneous complexes are located within the Auburn Province (Table 4). The presence of a strong Late Carboniferous peak in the Surat Basin succession suggests that, contrary to previous views (Martin, 1980), the Auburn Block was elevated and eroded at the time.

Table 4. Selected isotopic ages from Ordovician-Triassic igneous units in the New England and Thomson orogens.

Igneous unit	Area	Age (Ma)	Reference	Corresponding detrital age population in this study
Rawbelle Batholith	Connors–Auburn Province	~240-265	Fanning et al., 2009; Withnall et al., 2009	240-266 Ma
Bookookoorara Monzogranite	Southern NEO	240.1±2.4	Li et al., 2012	240-266 Ma
Dumboy-Gragin Granite	Southern NEO	243±3.7	Vickery et al., 1997	240-266 Ma
New England Batholith	Southern NEO	244-298	Shaw and Flood, 1981; Li et al., 2012; Rosenbaum and Rubatto., 2012; Donchak et al., 2013	240-266 Ma
Boonoo Granite	Southern NEO	245.6±2.5	Li et al., 2012	240-266 Ma
Stanthrope Granite	Southern NEO	246.9±2.0	Donchak et al., 2007	240-266 Ma
Walcha Road Monzogranite	Southern NEO	249±3-253.8±1.8	Jackson et al., 2004; Li et al., 2012	240-266 Ma
Duncans Creek Trondhjemite	Southern NEO	249-252	Cawood et al., 2011	240-266 Ma
Inlet Monzonite	Southern NEO	249-255	Li et al., 2012	240-266 Ma
Gilgai Granite	Southern NEO	250-254	Cross et al., 2010	240-266 Ma
Eidsvold Complex	Connors–Auburn Province	~250-258	Donchak et al., 2013	240-266 Ma
Ridgelands Granodiorite	Northern NEO	~251	Gust et al., 1993; Purdy, 2013	240-266 Ma
Tingha Monzogranite	Southern NEO	251.3±1.7	Cross et al., 2010	240-266 Ma
Redshirt Granite	Yarrol Province	251±4	Fanning, 2012	240-266 Ma
Mackenzie Monzogranite	Southern NEO	251.7±2.1	Li et al., 2012	240-266 Ma
Herries Granite	Southern NEO	251.8±2.5	Li et al., 2012	240-266 Ma
Clare Hills Granite	Southern NEO	252.0±2.5	Li et al., 2012	240-266 Ma
Wallangarra Volcanics	Southern NEO	253±2.4	Cross et al., 2009	240-266 Ma
Fairleigh Granite	Southern NEO	253.3±2.5	Li et al., 2012	240-266 Ma
Dundee Rhyodacite	Southern NEO	254.34±0.34	Brownlow and Cross, 2010	240-266 Ma
Parlour Mountain Granite	Southern NEO	254.7±1.6	Cross et al., 2010	240-266 Ma
Palgrave Granite	Southern NEO	256±1.8	Donchak et al., 2007	240-266 Ma
Boxwell Granite	Southern NEO	256.6±1.7	Cross et al., 2010	240-266 Ma
Craiglands Quartz Monzodiorite	Yarrol Province	256.8±2.6	Fanning, 2012	240-266 Ma
Tenningering Granodiorite	Gayndah–Gladstone belt (N)	259±2	Carson et al., 2006	240-266 Ma
Captain Osborne Granite	Northern NEO	~260	Gust et al., 1993; Purdy, 2013	240-266 Ma
Mingimarny Granite	Southern NEO	260.1±2.4	Cross et al., 2009	240-266 Ma
Gaeta Diorite	Gayndah–Gladstone belt (N)	262.6±2.5	Carson et al., 2006	240-266 Ma
Wolca Granite	Gayndah–Gladstone belt (N)	263±1.6	Carson et al., 2006	240-266 Ma
Gerringong Volcanics	Northern NEO	263.4±2.4	Carr et al., 2003; Metcalfe et al., 2015	240-266 Ma
Drake Volcanics	Southern NEO	264.4±2.5	Cross et al., 2010	240-266 Ma

Barrington Tops Granodiorite	Southern NEO	~267	Cawood et al., 2011	240-266 Ma
Many Peaks Granite	Northern NEO	~268	Gust et al., 1993	240-266 Ma
Tartrus Rhyolite	Connors–Auburn Province	300.8±4.1	Fanning et al., 2009	300-329 Ma
Doreen Granite	Connors–Auburn Province	300.9±3.4	Fanning et al., 2009	300-329 Ma
Macksford Volcanics	Northern NEO	>304	Withnall et al., 2013	300-329 Ma
Amelia Creek Tonalite	Connors–Auburn Province	304.3±5.8	Allen et al., 1998	300-329 Ma
Kennedy Igneous Association	Currabubula-Connors Arc	306-344	Gunther and Withnall, 1995; Garrad and Bultitude, 1999; Cross et al., 2012; Murgulov et al., 2013; Kositcin et al., 2015	300-329 Ma
Broadsound Range Volcanics	Northern NEO	308-313	Day et al., 1978; Holcombe et al., 1997	300-329 Ma
Mount Crompton Granodiorite	Connors–Auburn Province	308.1±1.9	Cross et al., 2012	300-329 Ma
Menilden Creek Tonalite	Connors–Auburn Province	308.2±7.1	Allen et al., 1998	300-329 Ma
Multiple volcanic suites	Connors–Auburn Province	310-315	Black, 1994; Bryan et al., 2004; Withnall et al., 2009; Murray et al., 2012; Cross et al., 2016	300-329 Ma
Multiple granites	Connors–Auburn Province	310-325	Allen et al., 1998; Withnall et al., 2009; Cross et al., 2012; 2015; 2016	300-329 Ma
Dacey granite	Connors–Auburn Province	313.0±4.0	Fanning et al., 2009	300-329 Ma
Broadsound Range Volcanics	Connors–Auburn Province	313.8±3.2	Fanning et al., 2009	300-329 Ma
Whelan Creek Volcanics	Connors–Auburn Province	314.1±5	Fanning et al., 2009	300-329 Ma
Whelan Creek Volcanics	Northern NEO	314.1±5.0	Day et al., 1978; Holcombe et al., 1997	300-329 Ma
Sambo Granite	Connors–Auburn Province	314.3±3.8	Fanning et al., 2009	300-329 Ma
Bora Creek Quartz Monzodiorite	Connors–Auburn Province	316.4±3.4	Fanning et al., 2009	300-329 Ma
Milwarra Quartz Diorite	Connors–Auburn Province	322.3±2.1	Cross et al., 2012	300-329 Ma
Tommy Roundback Granodiorite	Connors–Auburn Province	323.1±2.2	Cross et al., 2012	300-329 Ma
Mountain View Volcanics	Connors–Auburn Province	~325	Withnall et al., 2009	300-329 Ma
Torsdale Volcanics	Northern NEO	~325-300	Withnall et al., 2013	300-329 Ma
Birds Nest Granodiorite	Connors–Auburn Province	327.9±2.4	Cross et al., 2012	300-329 Ma
Unnamed granite	Northern Thomson Orogen	453.8±8.4	Siégel et al., 2018	450-455 Ma
Fat Hen Creek Complex	Western Charters Towers Province	~455-495	Cross et al., 2018	450-455 Ma
Granite Springs Granite	Eulo Ridge	455.6±5.4-456.3±3.9	Cross et al., 2018; Purdy et al., 2016b; 2018	450-455 Ma
Unnamed granite	Eastern Thomson Orogen	458.6±8.4	Siégel et al., 2018	450-455 Ma

Alternatively, to the Carboniferous and Permian-Triassic populations in the Surat Basin being sourced directly from igneous source terranes, they may represent material recycled from the underlying Moolayember Formation. The presence of similar Permian-Triassic and Carboniferous peaks in both the Moolayember Formation and the Precipice-Evergreen succession likely results from erosional incision of the Precipice Sandstone into the Bowen Basin succession and incorporation of the eroded material into the younger strata.

Given the complex provenance and source-to-sink history of the Surat Basin, as well as the limitations of U-Pb detrital zircon dating as a provenance tool, it is difficult to distinguish between first-cycle sourcing from igneous terranes and multiply recycled sedimentary material (e.g., McLennan et al., 2001). Both types of sourcing likely contributed to sedimentation in the basin. Low-temperature detrital thermochronology, such as $^{40}Ar/^{39}Ar$ mica dating and fission track or (U-Th)/He dating of detrital zircon or apatite, may add resolution to the multi-cycle sediment history, provided that the individual source terranes are characterised by distinct thermal histories (e.g., Reiners et al., 2000; 2002; Haines et al., 2004; Carrapa et al., 2009; Carrapa, 2010). In the case of sedimentary rocks of the Bowen Basin and igneous suites of the New England Orogen, different thermal signatures are likely.

Besides the three orogens proximal to the Surat Basin, other potential source terranes, although much more far-field, include the Mossman Orogen of the Tasmanides, the Mount Isa and Georgetown provinces of the North Australian Craton (Figure 2), central Australian Arunta and Musgrave provinces, as well as the Gawler Craton in South Australia. Any sediment input from central Australia (e.g., Camacho et al., 2002; Maidment et al., 2007) or the Gawler Craton (e.g., Reid and Payne, 2017) is unlikely given the sparsity of Palaeoproterozoic ages and the virtual absence of Archean ages in the Surat Basin age spectra. Silurian ages are also sparse, ruling out the Mossman Orogen as a significant sediment source terrane (Figure 25). Although the minor Mesoproterozoic population in the J10-TS1 interval partially overlaps with the second major age peak of the Mossman Orogen, the relative proportion of this age population, as well as the distance to the basin (Figure 2), renders the Mossman Orogen unlikely as a major source terrane. Similarly, the Mount Isa and Georgetown provinces are characterised by prominent Meso- and Palaeoproterozoic detrital populations (e.g., Page and Sun, 1998; Black et al., 2005; Withnall, 2019) but are located >1000 km from the Surat Basin. While minor sediment sourcing directly from the North Australian Craton cannot be excluded, the Anakie Province and Nebine Metamorphics of the Thomson Orogen, which also contain a small proportion of Meso- and Palaeoproterozoic ages (Figure 26), are more likely sources given their proximity to the basin.

The youngest component of the Precipice-Evergreen age spectra, the Early Jurassic population, reflects input from syn-depositional or close to syn-depositional volcanism either located on the active continental margin to the east or other locations within the New England Orogen more proximal to the Surat Basin. Sourcing from the distal Gondwana margin is considered more likely than intrabasinal volcanism (which implies intraplate, rift-related magmatism; Fielding, 1996; Yago and Fielding, 1996) given the presence of andesitic rock fragments in the sandstones, as well as the paucity, limited thickness, and fine-grained character of the interbedded tuffs. This interpretation is consistent with recently growing evidence of continued late Palaeozoic to mid-Cretaceous magmatic detritus recorded in eastern Australian sedimentary record, indicating long-lived continental magmatic arc on the eastern Gondwana margin (Tucker et al., 2016; Wainman et al., 2019; Foley et al., 2021a). The syn-depositional volcanic input is nearly absent below the TS1 surface and increases over time (Figure 15 and Figure 16). This could reflect a period of quiescence at the magmatic arc in the Sinemurian-Pliensbachian, followed by a period of intensified magmatism around the Toarcian, as magmatic pulses are often well preserved in detrital record (e.g., Paterson and Ducea, 2015). Hafnium isotope analysis of the young zircon population in the Surat Basin could further test the continental arc sourcing, as zircons from the New England Orogen arc are characterised by strongly positive εHf(t) values (Foley et al., 2021a).

The section just below the TS1 surface in the southern hypothesised depocentre that is characterised by contrasting provenance (Figure 15, Figure 16 and Figure 23) likely represents sediment derivation from a unique local source. The age signature in this section strongly resembles the Moolayember Formation rather than the typical Precipice Sandstone age signature, which is well illustrated on the MDS plot (Figure 19). In addition to the two age peaks characteristic of the Moolayember Formation, samples from this section contain an Early-Middle Devonian population (peaking at 394 Ma) that is absent anywhere else in the succession. This suggests sediment recycling from locally exposed Moolayember Formation and isolation from the Thomson Orogen sources further to the north and west, based on the absence of Pacific-Gondwanan and Grenvillian

populations. This isolation, however, must have been only temporary since the age signatures below and above this section in West Moonie 1 are similar to the rest of the basin. The Middle Devonian age population likely represents partial sourcing from the relatively proximal Texas and Silverwood provinces southeast of the Surat Basin. The Texas and Silverwood provinces are some of the oldest building blocks of the New England Orogen and contain volcanic and sedimentary rocks of Devonian age (e.g., Ormoral Volcanics and Bromley Hills Formation; Van Noord, 1999; Donchak et al., 2007; 2013). One potential explanation of the ~394 Ma population appearing higher in the J10-TS1 interval is reactivation of fault zones, exposing new source terranes within the Texas and Silverwood blocks.

4.3.4 The two depocentre hypothesis

This study tested the hypothesis of the northern and southern parts of the Surat Basin, where the EPQ7 and EPQ10 CTSCo tenements are located, representing two separate depocentres during the deposition of the Precipice Sandstone. Findings presented in this study, based on the rigorous comparison of the new West Moonie 1 data with several wells in the north, do not equivocally support the hypothesis. Sandstone compositions, sedimentary provenance and palaeocurrent patterns are relatively uniform across the area. The minor differences in detrital age distributions among individual wells are not unexpected and can be attributed to the unique distance of each well to the source, as well as to natural variations commonly observed within the same stratigraphic unit, (e.g., Shaanan et al., 2017; 2019). One notable difference that has been observed is the provenance change in the section below TS1 in the southern area (West Moonie 1), accompanied by a shift in palaeocurrent directions (Figure 18). In contrast, the correlative section in the north area (West Wandoan 1) shows uniform provenance throughout the J10-TS1 interval, despite changing palaeocurrent patterns up-section. While this difference does suggest different sediment sourcing for this part of the succession in the south, the change in sedimentation pattern is interpreted to be temporary and potentially localised. Hence, a basin model with two isolated depocentres, separated by a topographic barrier, does not need to be invoked. On the contrary, the uniform southward palaeocurrent trend in the lowermost Precipice Sandstone and the overall similar detrital age patterns across the whole area, indicate that any topographic high inferred from the isopach maps did not form an efficient barrier to sediment transport (Figure 27).

This project addressed the knowledge gap on the mineral composition and sediment provenance of the Precipice Sandstone and Evergreen Formation. It advanced the understanding of the formation in the Moonie area where there was little data previously, providing the context of the regional depositional setting of the Precipice-Evergreen succession in both the north and south of the basin. The overall similarity of sandstone petrography, detrital ages, and palaeocurrent patterns in the lowermost Precipice Sandstone across the study area suggests that the known reservoir properties derived from the north of the basin may be applicable in the EPQ10 tenement, which is now a CCS target.

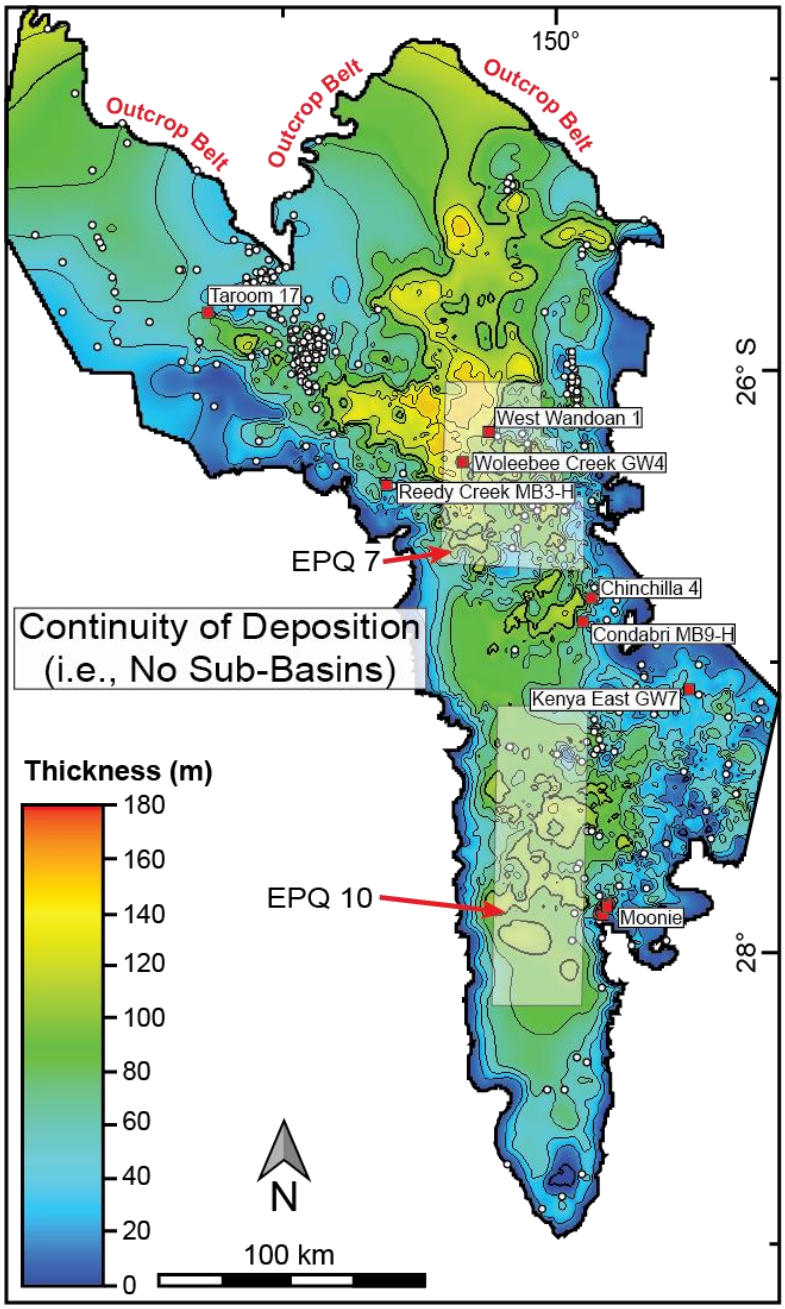

Figure 27. Revised model of the lower Precipice Sandstone (J10-TS1) representing continuous sedimentation across the northern and southern areas of the formation extent.

5. Conclusions

The study is one part ('Part A') of a two-part investigation aimed at assessing the applicability of previous work to understand the reservoir and sealing characteristics of EPQ7 tenement to the newly developing EPQ10 area. Part A directly tested the two depocentres hypothesis for the Precipice Sandstone and Evergreen Formation in the Surat Basin, Australia, by applying palaeocurrent analysis (8 wells), mineralogical point counting (10 samples from 5 wells), CA-TIMS dating (2 samples from 2 wells), and detrital zircon geochronology (29 samples from 7 wells). The results were discussed in the context of our current state of knowledge regarding the Precipice-Evergreen and the broader palaeogeography and tectonics of eastern Australia during the Early Jurassic. This knowledge base was furnished by many workers across several decades, with the most recent studies undertaken by the UQ Centre for Natural Gas (UQ-SDAAP Project) and the UQ School of Earth and Environmental Sciences (Esterle Group). The second part ('Part B'; ANLEC R&D Project 7-0320-C330) focused on evaluating potential correlations between quartz overgrowth geochemistry and the diagenetic conditions during quartz precipitation.

At the most fundamental level, the study found **little evidence to support the hypothesis of two distinct depocentres for the Precipice-Evergreen interval in the Surat Basin**. However, there may have been different sediment sources for wells on the southern portion of the basin during deposition of the upper part of the J10-TS1 interval, despite these potential changes in sediment source being localized and geological short-lived. This means that from a sediment provenance perspective the data previously collected and analysed from the EPQ7 tenement may be a partial analogue for the West Moonie 1 well, except for the top of the J10-TS1 interval where some differences were noted in the sandstone compositions and detrital zircon age spectra.

The other major conclusions that were drawn from the analysis and results are:

- Palaeoflow during deposition of the Precipice Sandstone and Evergreen succession did not differ significantly between the northern and southern parts of the basin, and flow directions corroborate previous work. The main blocky sandstone facies exhibited the general southerly flow, but this transitioned upwards to dispersed but northerly flow directions as the TS1 boundary was approached. The stratigraphic position of this transition varied between wells; its causes are, as yet, unresolved.
- No significant difference in sandstone composition was noted between the northern and southern regions of the Surat Basin, except for an interval in the upper part of the J10-TS1 interval in the wells in the south (Moonie 34 and West Moonie 1) that showed less quartzose sandstone composition than the equivalent stratigraphic interval in the north, indicating different provenance.
- Mineralogical provenance plots showed that the J10-TS1 interval is sourced by material from the craton interior, whereas sediments in the TS1-MFS1 interval are characterised by mixed continental block to quartzose recycled orogen provenance.
- Detrital zircon geochronology revealed a complex age pattern with multiple distinct age populations that cannot be assigned to a single source terrane; more than one source terrane contributed sediment into the basin through the depositional history – recycled sedimentary and metasedimentary basement rocks (indicated by Pacific-Gondwana, Grenvillian, Meso- and Palaeoproterozoic zircon age populations), plutonic and volcanic basement rocks (Permian-Triassic, Carboniferous, Middle Devonian and Late Ordovician populations), and contemporaneous volcanic rocks (<201 Ma ages).
- The zircon age profile of the Precipice-Evergreen succession suggests that the Thomson Orogen was the main source of sediment. In the J10-TS1 interval, the main Thomson Orogen basement units that contributed sediment to the Surat Basin were the Nebine Metamorphics and combined units of the Anakie Inlier and Charters Towers Province to the northwest. The zircon age spectra of the TS1-J30

interval indicates that contribution from these blocks decreased and sediment was mostly sourced from the central Thomson Orogen and Roma Shelf. At the time of the deposition of the Precipice Sandstone, these areas had not yet been covered by the Jurassic-Cretaceous Eromanga Basin and were only partly covered by the Palaeozoic Adavale and Drummond basins. Significant sediment input from the New England Orogen to the east and south of the Surat Basin is also evident from the detrital zircon age spectra, as well as material recycled from the underlying Bowen Basin succession. No substantial sediment was contributed from the Lachlan Orogen.

- Absolute age dating combined with existing palynostratigraphy places the Evergreen Formation in the middle Pliensbachian to the topmost Toarcian, and by relation the Precipice Sandstone into the Lower Jurassic Sinemurian to Pliensbachian. The new precise depositional age data also hint at a diachronicity across the northwest-northeast section of the basin, but this requires additional dating to corroborate.

The main conclusions of Part B, which are compatible with these results are (Delle Piane and Bourdet, 2022):

- The main reservoir interval in West Wandoan 1 which is situated in the northern part of the Surat Basin has a similar mineralogy to that intersected in West Moonie 1 in the southern part of the basin. Both are quartzarenites, with an overwhelming dominance of monocrystalline quartz.
- The diagenesis of both wells was similar, resulting in widespread quartz overgrowths with minor kaolinite and siderite cements.
- The amount of diagenetic quartz varies little between the two wells, on average ca. 10%. This and the temperature of homogenization derived from fluid inclusion analysis suggest similar maximum burial depths at the two well locations.
- A common crystalline source of the sediment is inferred based on the striking similarity in trace element concentrations in detrital quartz grains.
- During diagenesis, quartz cement precipitated in a temperature range of ca. 60 – 115°C from fluids with low solute content, low salinity (< 30000 ppm NaCl equivalent) and with strong contribution of meteoric water.

6. References

Ainsworth, R. B., Vonk, A. J., Wellington, P., & Paumard, V. (2020). Out-of-phase cyclical sediment supply: A potential causal mechanism for generating stratigraphic asymmetry and explaining sequence stratigraphic spatial variability. Journal of Sedimentary Research, 90(12), 1706-1733.

Aitchison. (1990). Significance of Devonian-Carboniferous radiolarians from accretionary terranes of the New England Orogen, eastern Australia. Marine Micropaleontology, 15(3-4), 365–378. https://doi.org/10.1016/0377-8398(90)90020-M

Allen, C. M., Williams, I. S., Stephens, C. J. & Fielding, C. R. (1998). Granite genesis and basin formation in an extensional setting: the magmatic history of the northernmost New England Orogen. Australian Journal of Earth Sciences, 45, 875–88.

Asmussen, P., Bryan, S. E., Allen, C. M., & Purdy, D. J. (2018). Geochronology and geochemistry of the Devonian Gumbardo Formation (Adavale Basin): evidence for cratonisation of the Central Thomson Orogen by the Early Devonian. Australian Journal of Earth Sciences, 65(7-8), 1133-1159.

Basu, A. (1985). Reading Provenance from Detrital Quartz. In G. G. Zuffa (Ed.), Provenance of Arenites (pp. 231-247). Dordrecht: Springer Netherlands.

Bianchi, V., Zhou, F., Sliwa, R., & Esterle, J. (2016). Re-adjusting the paleodrainage in the Surat Basin infill: dynamic platform tilting wanted. Paper presented at the 40th Sydney Basin Symposium, New South Wales.

Bianchi, V., Pistellato, D., Zhou, F., Boccardo, S., & Esterle, J. (2017). Outcrop analogue models of the Precipice Sandstone. ANLEC 07-0314-0228 Final Report of Outcrop Analogues and Preliminary Models. Brisbane: University of Queensland.

Bianchi, V., Zhou, F., Pistellato, D., Martin, M., Boccardo, S., & Esterle, J. (2018). Mapping a coastal transition in braided systems: an example from the Precipice Sandstone, Surat Basin. Australian Journal of Earth Sciences, 65:4, 483-502.

Bianchi, V., Pistellato, D., Job, A., & Esterle, J. (2019). Regional geological study of the Hutton Sandstone. ANLEC 7-1116-0294 Final Report.

Black, L. P. (1994). Appendix 2: U–Pb zircon geochronology, record no. 1994/21. Australian Geological Survey Organisation, Canberra, 163-8.

Black, L. P., Withnall, I. W., Gregory, P., Oversby, B. S., & Bain, J. H. C. (2005). U-Pb zircon ages from leucogneiss in the Etheridge Group and their significance for the early history of the Georgetown region, north Queensland. Australian Journal of Earth Sciences, 52(3), 385-401.

Bradshaw, B. E., Spencer, L. K., Lahtinen, A. L., Khider, K., Ryan, D. J., Colwell, J. B., . . . Hodgkinson, J. (2011). An assessment of Queensland's CO_2 geological storage prospectivity—the Queensland CO_2 Geological Storage Atlas. Energy Procedia, 4, 4583-4590.

Bradshaw, M., & Yeung, M. (1990). The Jurassic Palaeogeography of Australia. Bureau of Mineral Resources. Geology and Geophysics, 60.

Brown, D. D., Carr, P. A., & Purdy, D. J. (2012). Database of basement drill holes in the Thomson Orogen and Roma Shelf regions, Queensland (Record No: 2012/06). Brisbane: Geological Survey of Queensland, Department of Natural Resource and Mines.

Brownlow, J. & Cross, A. (2010). TIMS U-Pb and SHRIMP U-Pb zircon dating of the Dundee Rhyodacite, northern New England, NSW. In S Buckman & PL Blevin (eds), Proceedings of the New England Orogen 2010

conference held at the University of New England, Armidale, New South Wales, Australia, November 2010, University of New England, Armidale, pp. 69–74.

Bryan, S. E., Allen, C. M., Holcombe, R. J., & Fielding, C. R. (2004). U-Pb zircon geochronology of Late Devonian to Early Carboniferous extension-related silicic volcanism in the northern New England Fold Belt. Australian Journal of Earth Sciences, 51(5), 645-664.

Bryan, S. E., Fielding, C. R., Holcombe, R. J., Cook, A., & Moffitt, C. A. (2003). Stratigraphy, facies architecture and tectonic implications of the Upper Devonian to Lower Carboniferous Campwyn volcanics of the northern New England Fold Belt. Australian Journal of Earth Sciences, 50(3), 377-401.

Camacho, A., Hensen, B. J., & Armstrong, R. A. (2002). Isotopic test of a thermally driven intraplate orogenic model, Australia. Geology, 30(10), 887-890.

Carr, P. F., Fanning, M., Jones, B. G., & Hutton, A. C. (2003). Geochronology of coal measures in the Sydney Basin from U-Pb SHRIMP dating of airfall tuffs. 35th Sydney Basin Symposium on Advances in the Study of the Sydney Basin, School of Geosciences, University of Wollongong, pp. 303–305.

Carrapa, B., DeCelles, P. G., Reiners, P. W., Gehrels, G. E., & Sudo, M. (2009). Apatite triple dating and white mica40Ar/39Ar thermochronology of syntectonic detritus in the Central Andes: A multiphase tectonothermal history. Geology, 37(5), 407-410.

Carrapa, B. (2010). Resolving tectonic problems by dating detrital minerals. Geology, 38(2), 191-192.

Carson, C. J., von Gnielinski, F. E., & Bultitude, R. J. (2006). Results of the joint GSQ-GA geochronology project New England Orogen. Rosedale, Mount Perry and Gladstone 1:100 000 sheet areas March 2006-October 2006, record no. 2006/1, Geological Survey of Queensland, Brisbane.

Cawood, P. A., Pisarevsky, S. A., & Leitch, E. C. (2011). Unravelling the New England orocline, east Gondwana accretionary margin. Tectonics, 30(TC5002).

Cook, A. G., & Draper, J. J. (2013). Surat Basin. In P. A. Jell (Ed.), Geology of Queensland (pp. 533-539): Geological Survey of Queensland.

Copeland, P. (2020). On the use of geochronology of detrital grains in determining the time of deposition of clastic sedimentary strata. Basin Research 32(6), 1532-1546.

Corfu, F., Hanchar, J. M., Hoskin, P. W. O., & Kinny, P. (2003). Atlas of zircon textures. Reviews in Mineralogy and Geochemistry, 53(1), 469-500.

Coutts, D. l. S., Matthews, W. A., & Hubbard, S. M. (2019). Assessment of widely used methods to derive depositional ages from detrital zircon populations. Geoscience Frontiers, 10(4), 1421-1435.

Craven, S. J., & Daczko, N. R. (2017). The Keepit arc: Provenance of sedimentary rocks in the central Tablelands Complex, southern New England Orogen, Australia, as recorded by detrital zircon. Australian Journal of Earth Sciences, 64(3), 401-418.

Cross, A. J., Purdy, D. J., & Bultitude, Dhnaram, C. R., & von Gnielinski, F. E. (2009). Joint GSQ-GA NGA geochronology project, New England Orogen and Drummond Basin, 2008, record no. 2009/03, Geological Survey of Queensland, Brisbane.

Cross, A. J., Bultitude, R. J., & Purdy, D. J. (2010). New SHRIMP geochronology for the Connors Arch, northern New England Orogen, record no. 2010/04, Geological Survey of Queensland, Brisbane, pp. 35–7.

Cross, A. J., Bultitude, R. J., & Purdy, D. J. (2012). Summary of results for the joint GSQ-GA geochronology project: Ayr, Bowen, Eulo, Mount Coolon, Proserpine and Warwick 1:250 000 sheet areas, record no. 2012/19, Geological Survey of Queensland, Brisbane.

Cross, A. J., Purdy, D. J., & Bultitude (2012). Summary of results of the joint GSQ-GA geochronology project: Monto and Maryborough 1:250 000 sheet areas, record no. 2012/2, Geological Survey of Queensland, Brisbane.

Cross, A. J., Purdy, D. J., Bultitude, R. J., Brown, D. D., & Carr, P. A. (2016). Summary of results – Joint GSQ-GA geochronology project: Thomson Orogen, New England Orogen, Mossman Orogen and Mount Isa Region, 2011-2013. Brisbane Qld: Queensland Geological Record 2016/03.

Cross, A. J., Purdy, D. J., Champion, D. C., Brown, D. D., Siégel, C., & Armstrong, R. A. (2018). Insights into the evolution of the Thomson Orogen from geochronology, geochemistry, and zircon isotopic studies of magmatic rocks. Australian Journal of Earth Sciences, 65(7-8), 987-1008.

Day, R. W., Murray, C. G., & Whitaker, W. G. (1978). The eastern part of the Tasman Orogenic Zone. Tectonophysics, 48, 327-64.

Delle Piane, C., & Bourdet, J., (2022) Testing the Surat Basin two deposition centres hypotheses: Part B diagenetic mechanism. ANLEC R&D project 7-0320-C330 Milestone report # 3.

Dickinson, W. R. (1970). Interpreting detrital modes of graywacke and arkose. Journal of Sedimentary Research, 40(2), 695-707.

Dickinson, W. R., & Suczek, C. A. (1979). Plate tectonics and sandstone compositions. The American Association of Petroleum Geologists Bulletin, 63(12), 2164-2182.

Dickinson, W. R., Beard, L. S., Brakenridge, G. R., Erjavec, J. L., Ferguson, R. C., Inman, K. F., . . . Ryberg, P. T. (1983). Provenance of North American Phanerozoic sandstones in relation to tectonic setting. Geological Society of America Bulletin, 94(2), 222-235.

Dickinson, W. R. (1985). Interpreting provenance relations from detrital modes of sandstones. Provenance of arenites. Proc. Cetraro, Cosenza, 1984, 333-361.

Dickinson, W. R., & Gehrels, G. E. (2009). Use of U–Pb ages of detrital zircons to infer maximum depositional ages of strata: a test against a Colorado Plateau Mesozoic database. Earth and Planetary Science Letters, 288(1-2), 115-125.

Donchak, P. J. T., Bultitude, R. J., Purdy, D. J., & Denaro, T. J. (2007). Geology and mineralisation of the Texas region, south-eastern Queensland. Queensland Geology, 11, 1-95.

Donchak, P. J. T., Purdy, D., Withnall, I. W., Blake, P. R., & Jell, P. A. (2013). New England Orogen. In P. A. Jell (Ed.), Geology of Queensland (pp. 305-472): Geological Survey of Queensland.

Dodson, M. H. (1973). Closure temperature in cooling geochronological and petrological systems. Contributions to Mineralogy and Petrology, 40(3), 259-274.Exon, N. F. (1976). Geology of the Surat Basin in Queensland Bureau of Mineral Resources, Geology and Geophysics. Canberra, Australia, pp. 160.

Dokuz A. & Tanyolu E. (2006). Geochemical constraints on the provenance, mineral sorting and subaerial weathering of Lower Jurassic and Upper Cretaceous clastic rocks of the Eastern Pontides, Yusufeli (Artvin), NE Turkey, Turkish Journal of Earth Sciences, 15, 181-209.

Draper, J. J. (2006). The Thomson fold belt in Queensland revisited. ASEG Extended Abstracts, 2006(1), 1-6.

Dwyer, R. C., Collins, W. J., Hack, A. C., Hegarty, R., & Huang, H.-Q. (2018). Age and tectonic significance of the Louth Volcanics: implications for the evolution of the Tasmanides of eastern Australia. Australian Journal of Earth Sciences, 65(7-8), 1049-1069.

Embry, A. F., & Johannessen, E. P. (1993). T–R sequence stratigraphy, facies analysis and reservoir distribution in the uppermost Triassic–Lower Jurassic succession, western Sverdrup Basin, Arctic Canada. In

T. O. Vorren, E. Bergsager, Ø. A. Dahl-Stamnes, E. Holter, B. Johansen, E. Lie, & T. B. Lund (Eds.), Arctic Geology and Petroleum Potential: Proceedings of the Norwegian Petroleum Society Conference (Vol. 2, pp. 121-146). Tromso, Norway: Elsevier.

Evans, P. R. (1965). Recent advances in Mesozoic stratigraphic palynology in Australia. Bureau of Mineral Resources, Australia, Record, 192, 26.

Evans, P. R. (1966). Mesozoic stratigraphic palynology in Australia. Australian Oil and Gas Journal, 12(6), 58-63.

Exon, N. F. (1976). Geology of the Surat Basin in Queensland. Bureau of Mineral Resources, Geology, and Geophysics Bulletin 166.

Exon, N. F., & Burger, D. (1981). Sedimentary cycles in the Surat Basin and global changes of sea level. Bureau of Mineral Resources Journal of Australian Geology and Geophysics, 6, 153-159.

Fanning, C. M., Withnall, I. W., Hutton, L. J., Bultitude, R. J., von Gnielinski, F. E., & Rienks, I. P. (2009). Appendix – SHRIMP U-Pb zircon ages from central Queensland. Queensland Geology, 12, 463–573.

Fanning, C.M. (2012). U-Pb zircon dating (SHRIMP). Queensland Geology, 13, 525–65.

Farquhar, S. M., Dawson, G. K. W., Esterle, J. S., & Golding, S. D. (2013). Mineralogical characterisation of a potential reservoir system for CO_2 sequestration in the Surat Basin. Australian Journal of Earth Sciences, 60(1), 91-110.

Fergusson, C. L., Carr, P. F., Fanning, C. M., & Green, T. J. (2001). Proterozoic-Cambrian detrital zircon and monazite ages from the Anakie Inlier, central Queensland: Grenville and Pacific-Gondwana signatures. Australian Journal of Earth Sciences, 48(6), 857-866.

Fergusson, C. L., Henderson, R. A., Fanning, C. M., & Withnall, I. W. (2007). Detrital zircon ages in Neoproterozoic to Ordovician siliciclastic rocks, northeastern Australia: Implications for the tectonic history of the East Gondwana continental margin. Journal of the Geological Society, 164(1), 215-225.

Fergusson, C. L., & Henderson, R. A. (2013). Thompson Orogen. In P. A. Jell (Ed.), Geology of Queensland (pp. 113-224): Geological Survey of Queensland.

Fergusson, C. L. (2017). Mid to late Paleozoic shortening pulses in the Lachlan Orogen, southeastern Australia: a review. Australian Journal of Earth Sciences, 64(1), 1-39.

Fielding, C. R. (1996). Mesozoic sedimentary basins and resources in eastern Australia—a review of current understanding. Paper presented at the Mesozoic 96. Proceedings of the Mesozoic Geology of the Eastern Australia Plate Conference, Brisbane, Queensland.

Fielding, C. R., Sliwa, R., Holcombe, R. J., & Kassan, J. (2000). A new palaeogeographic synthesis of the Bowen Basin of central Queensland. Paper presented at the Bowen Basin Symposium.

Foley, E. K., Henderson, R. A., Roberts, E. M., Kemp, A. I. S., Todd, C. N., Knutsen, E. M., Fisher, C., Wainman, C. C., & Spandler, C. (2021a). Jurassic Arc: Reconstructing the Lost World of eastern Gondwana. Geology, 49(11), 1391-1396.

Foley, E. K., Roberts, E. M., & Knutsen, E. M. (2021b). Deciphering Late Cretaceous palaeo-river catchments in eastern Australia: recognition of distinct northern and southern drainage basins. Basin Research, 00, 1-28.

Fraser, G. L., Gilmore, P. J., Fitzherbert, J. A., Trigg, S. J., Campbell, L. M., Deyssing, L., . . . Blevin, P. L. (2014). New SHRIMP U–Pb zircon ages from the Lachlan, southern Thomson and New England orogens. New South Wales: February 2011-June 2013. Geoscience Australia.

Gani, M. R. (2017). Mismatch between time surface and stratal surface in stratigraphy. Journal of Sedimentary Research, 87(11), 1226-1234.

Garrad, P. D., & Bultitude, R. J. (1999). Geology, mining history and mineralisation of the Hodgkinson and Kennedy provinces, Cairns region, north Queensland. Queensland Minerals and Energy Review Series, Department of Mines and Energy, Brisbane, pp. 1-306.

Garzanti, E., Canclini, S., Foggia, F. M., & Petrella, N. (2002). Unravelling magmatic and orogenic provenance in modern sand: the back-arc side of the Apennine thrust belt, Italy. Journal of Sedimentary Research, 72(1), 2-17.

Garzanti, E., Limonta, M., Resentini, A., Bandopadhyay, P. C., Najman, Y., Andò, S., & Vezzoli, G. (2013). Sediment recycling at convergent plate margins (Indo-Burman ranges and Andaman–Nicobar Ridge). Earth-Science Reviews, 123, 113-132.

Garzanti, E. (2016). From static to dynamic provenance analysis—Sedimentary petrology upgraded. Sedimentary Geology, 336, 3-13.

Garzanti, E. (2019). Petrographic classification of sand and sandstone. Earth-Science Reviews, 192, 545-563.

Glen, R. A. (2005). The Tasmanides of eastern Australia. Special Publication-Geological Society of London, 246, 23.

Glen, R. A., Korsch, R. J., Hegarty, R., Saeed, A., Djomani, Y. P., Costelloe, R. D., & Belousova, E. A. (2013). Geodynamic significance of the boundary between the Thomson Orogen and the Lachlan Orogen, northwestern New South Wales and implications for Tasmanide tectonics. Australian Journal of Earth Sciences, 60(3), 371-412.

Glen, R. A., Saeed, A., Quinn, C. D., & Griffin, W. L. (2011). U–Pb and Hf isotope data from zircons in the Macquarie Arc, Lachlan Orogen: Implications for arc evolution and Ordovician palaeogeography along part of the east Gondwana margin. Gondwana Research, 19(3), 670-685.

Gray, A. R. G. (1968). Stratigraphic drilling the Surat and Bowen basins, 1965-1966 (No. 22). Queensland Department of Mines.

Green, P. M. (1997). The Surat and Bowen Basins, South-east Queensland. Minerals and Energy Review Series, Queensland Department of Mines and Energy.

Gunther, M. C., & Withnall, I. W. (1995). New and revised igneous rock units of the Rollingstone and Ewan 1:100 000 sheet areas. Queensland Government Mining Journal, 96, 16-25.

Gust, D. A., Stephens, C. J., & Grenfell, A. T. 1993. Granitoids of the northern NEO: their distribution in time and space and their tectonic implications. In New England Orogen, eastern Australia. ed. PG Flood and J Aitchison, pp. 565–71. Armidale: University of New England.

Haines, P. W., Turner, S. P., Kelley, S. P., Wartho, J., & Sherlock, S. C. (2004). ^{40}Ar–^{39}Ar dating of detrital muscovite in provenance investigations: a case study from the Adelaide Rift Complex, South Australia. Earth and Planetary Science Letters, 227(3-4), 297-311.

Helby, R., Morgan, R., & Partridge, A. D. (1987). A palynological zonation of the Australian Mesozoic. Memoir of the Association of Australasian Palaeontologists, 4, 1-94.

Hodgkinson, J., Hortle, A., & McKillop, M. (2010). The application of hydrodynamic analysis in the assessment of regional aquifers for carbon geostorage: preliminary results for the Surat Basin, Queensland. The APPEA Journal, 50(1), 445-462.

Hodgkinson, J., & Grigorescu, M. (2013). Background research for selection of potential geostorage targets—case studies from the Surat Basin, Queensland. Australian Journal of Earth Sciences, 60(1), 71-89.

Hoffmann, K. L., Totterdell, J. M., Dixon, O., Simpson, G. A., Brakel, A. T., Wells, A. T., & Mckellar, J. L. (2009). Sequence stratigraphy of Jurassic strata in the lower Surat Basin succession, Queensland. Australian Journal of Earth Sciences, 56, 461-476.

Holcombe R. J., Stephens C. J., Fielding C. R., Gust D. A., Little T. A., Sliwa, R., Kassan, J., McPhie, J., & Ewart, A. (1997). Tectonic evolution of the northern New England Fold Belt: Carboniferous to Early Permian transition from active accretion to extension. In Tectonics and metallogenesis of the New England Orogen, ed. PM Ashley, PG Flood, pp. 66-79: Geological Society of Australia Special Publication.

Ingersoll, R. V., Bullard, T. F., Ford, R. L., Grimm, J. P., Pickle, J. D., & Sares, S. W. (1984). The effect of grain size on detrital modes: a test of the Gazzi- Dickinson point-counting method (Holocene, sand, New Mexico, USA). Journal of Sedimentary Petrology, 54(1), 103-116.

Ireland, T. R., Bradshaw, J. D., Muir, R., Weaver, S. D., & Adams, C. J. (1994). Zircon age distributions in granites, greywackes, and gneisses from the Southwest Pacific-Gondwana region. US Geological Survey Circular, 1107, 151.

Ireland, T. R., Flottmann, T., Fanning, C. M., Gibson, G. M., & Preiss, W. V. (1998). Development of the early Paleozoic Pacific margin of Gondwana from detrital-zircon ages across the Delamerian orogen. Geology, 26(3), 243-246.

Jackson, S.E., Pearson, N. J., Griffin, W. L., & Belousova, E. A. (2004). The application of laser ablation-inductively coupled plasma-mass spectrometry (LA-ICP-MS) to in situ U-Pb zircon geochronology. Chemical Geology, 211, 47–69.

Jessop, K., Daczko, N. R., & Piazolo, S. (2019). Tectonic cycles of the New England Orogen, eastern Australia: A Review. Australian Journal of Earth Sciences, 66(4), 459-496.

Jones, G. D., & Patrick, R. B. (1981). Stratigraphy and coal exploration geology of the northeastern Surat Basin. Coal Geology, 1(4), 153-163.

Kay, S. M., Orrell, S., & Abbruzzi, J. M. (1996). Zircon and whole rock Nd-Pb isotopic evidence for a Grenville age and a Laurentian origin for the basement of the Precordillera in Argentina. The Journal of Geology, 104(6), 637-648.

Korsch, R. J. (1984). Sandstone compositions from the New England Orogen, eastern Australia; implications for tectonic setting. Journal of Sedimentary Research, 54(1), 192-211.

Korsch, R. J., Boreham, C. J., Totterdell, J. M., Shaw, R. D., & Nicoll, M. G. (1998). Development and petroleum resource evaluation of the Bowen, Gunnedah and Surat Basins, Eastern Australia. The APPEA Journal, 38(1), 199-237.

Korsch, R. J., Adams, C. J., Black, L. P., Foster, D. A., Fraser, G. L., Murray, C. G., . . . Griffin, W. L. (2009a). Geochronology and provenance of the Late Paleozoic accretionary wedge and Gympie Terrane, New England Orogen, eastern Australia. Australian Journal of Earth Sciences, 56(5), 655-685.

Korsch, R. J., Totterdell, J. M., Fomin, T., & Nicoll, M. G. (2009b). Contractional structures and deformational events in the Bowen, Gunnedah and Surat Basins, eastern Australia. Australian Journal of Earth Sciences, 56(3), 477-499.

Kositcin, N., Purdy, D. J., Brown, D. D., Bultitude, R. J., & Carr, P. A. (2015). Summary of results—Joint GSQ–GA Geochronology Project: Thomson Orogen and Hodgkinson Province, 2012–2013 (pp. 68). Brisbane Qld: Queensland Geological Record.

Krynine, P. D. (1946). Microscopic morphology of quartz types. Paper presented at the Annual 2nd Congress Panamas Ing Minas Geology.

La Croix, A. D., Wang, J., He, J., Hannaford, C., Bianchi, V., Esterle, J., & Undershultz, J. R. (2019a). Widespread nearshore and shallow marine deposition within the Lower Jurassic Precipice Sandstone and Evergreen Formation in the Surat Basin, Australia. Marine and Petroleum Geology, 109, 760-790.

La Croix A. D., Wang, J., & Underschultz, J. R. (2019b). Integrated facies analysis of the Precipice Sandstone and Evergreen Formation in the Surat Basin. The University of Queensland Surat Deep Aquifer Appraisal Project – Supplementary Detailed Report. Brisbane Qld: University of Queensland.

La Croix A, Hannaford C & Underschultz J (2019c), Palynological analysis of the Precipice Sandstone and Evergreen Formation in the Surat Basin. The University of Queensland Surat Deep Aquifer Appraisal Project – Supplementary Detailed Report, The University of Queensland.

La Croix A. D., He, J., Bianchi, V., Wang, J., Gonzalez, S., & Undershultz, J. R. (2020). Early Jurassic palaeoenvironments in the Surat Basin, Australia – marine incursion into eastern Gondwana. Sedimentology 67:457–485.

Li, P. F., Rosenbaum, G., & Rubatto, D. (2012). Triassic asymmetric subduction rollback in the southern New England Orogen (eastern Australia): the end of the Hunter-Bowen Orogeny. Australian Journal of Earth Sciences, 59(6), 965-981.

Maidment, D. W., Williams, I. S., & Hand, M. (2007). Testing long-term patterns of basin sedimentation by detrital zircon geochronology, Centralian Superbasin, Australia. Basin Research, 19(3), 335-360.

Martin, K. R. (1977). Sedimentology of the precipice sandstone, Surat Basin, Queensland. Unpublished PhD thesis, University of Queensland.

Martin, K. R. (1980). Deposition of the Precipice Sandstone and the evolution of the Surat Basin in the Early Jurassic. The APPEA Journal 21(1): 16-23.

Martin, M., Wakefield, M., Bianchi, V., Esterle, J., & Zhou, F. (2018). Evidence for marine influence in the Lower Jurassic Precipice Sandstone, Surat Basin, eastern Australia. Australian Journal of Earth Sciences, 65(1), 75-91.

McKellar, J. L. (1992). Jurassic palynostratigraphy in the Surat Basin - a review. In D. Burger, C. B. Foster, & J. L. McKellar (Eds.), A Review of Permian to Cretaceous Palynostratigraphy in Eastern Australia (Vol. Record 1992/5, pp. 17-22): Bureau of Mineral Resources, Geology and Geophysics.

McKellar, J. L. (1998). Late Early to Late Jurassic palynology, biostratigraphy and palaeogeography of the Roma Shelf area, northwestern Surat Basin, Queensland, Australia. Unpublished PhD thesis. University of Queensland.

McLennan, S. M., Bock, B., Compston, W., Hemming, S. R., & McDaniel, D. K. (2001). Detrital zircon geochronology of Taconian and Acadian foreland sedimentary rocks in New England. Journal of Sedimentary Research, 71(2), 305-317.

Metcalfe, I., Crowley, J. L., Nicoll, R. S., & Schmitz, M. (2015). High-precision U–Pb CA-TIMS calibration of middle Permian to lower Triassic sequences, mass extinction and extreme climate-change in eastern Australian Gondwana. Gondwana Research, 28(1), 61–81.

Mollan, R. G., Forbes, V. R., Jensen, A. R., Exon, N. F., & Gregory, C. M. (1972). Geology of the Eddystone, Taroom, and western part of the Mundubbera Sheet areas, Queensland. Bureau of Mineral Resources, Geology, and Geophysics. Report 142.

Murgulov, V., Griffin, W. L., & O'Reilly, S. Y. (2013). Carboniferous and Permian granites of the northern Tasman orogenic belt, Queensland, Australia: Insights into petrogenesis and crustal evolution from an in situ zircon study. International Journal of Earth Sciences, 102(3), 647–669.

Murray, C. G., Blake, P. R., Crouch, S. B. S., Hayward, M. A., Robertson, A. D. C., & Simpson, G. A. (2012). Geology of the Yarrol Province central coastal Queensland. Queensland Geology, 13, 674. Brisbane Qld: Geological Survey of Queensland.

Page, R. W., & Sun, S. S. (1998). Aspects of geochronology and crustal evolution in the Eastern Fold Belt, Mt Isa Inlier. Australian Journal of Earth Sciences, 45(3), 343-361.

Paterson, S. R., & Ducea, M. N. (2015). Arc magmatic tempos: Gathering the evidence. Elements, 11(2), 91-98.

Paton, C., Hellstrom, J., Paul, B., Woodhead, J., & Hergt, J. (2011). Iolite: Freeware for the visualisation and processing of mass spectrometric data. Journal of Analytical Atomic Spectrometry, 26(12), 2508-2518.

Pearce, J., Kirste, D. M., Dawson, G. K. W., Farquhar, S. M., Biddle, D., Golding, S. D., & Rudolph, V. (2015). SO_2 impurity impacts on experimental and simulated CO_2–water–reservoir rock reactions at carbon storage conditions. Chemical Geology, 399, 65-86.

Price, P. L., Wood, G. R., Pickering, S. A., Williams, A. J., & Filatoff, J. (1985). Late Palaeozoic and Mesozoic Palynostratigraphical Units: Report No. 274/25. CSR Oil & Gas Division, Palynology Facility.

Price, P. L. (1997). Permian to Jurassic palynostratigraphic nomenclature of the Bowen and Surat basins. In P. M. Green (Ed.), The Surat and Bowen Basins, southeast Queensland (pp. 137-178). Brisbane, Queensland: Queensland Department of Mines and Energy.

Purdy, D. J. (2013). Granitoids of the New England Orogen. In P. A. Jell (Ed.), Geology of Queensland (pp. 399-444). Brisbane Qld: Geological Survey of Queensland.

Purdy, D. J., Cross, A. J., Brown, D. D., Carr, P. A., & Armstrong, R. A. (2016a). New constraints on the origin and evolution of the Thomson Orogen and links with central Australia from isotopic studies of detrital zircons. Gondwana Research, 39, 41-56.

Purdy, D. J., Carr, P. A., Brown, D. D., Cross, A. J., Bultitude, R. J., Lee, M. S., & Verdel, C. (2016b). The Granite Springs Granite. Queensland Geological Record 2016/02.

Purdy, D. J., Hegarty, R., & Doublier, M. P. (2018). Basement geology of the southern Thomson Orogen. Australian Journal of Earth Sciences, 65(7-8), 893-916.

Raimondo, T., Collins, A. S., Hand, M., Walker-Hallam, A., Smithies, R. H., Evins, P. M., & Howard, H. M. (2010). The anatomy of a deep intracontinental orogen. Tectonics, 29(4), 1-31.

Rainbird, R. H., Hamilton, M. A., & Young, G. M. (2001). Detrital zircon geochronology and provenance of the Torridonian, NW Scotland. Journal of the Geological Society, 158(1), 15-27.

Reid, A. J., & Payne, J. L. (2017). Magmatic zircon Lu-Hf isotopic record of juvenile addition and crustal reworking in the Gawler Craton, Australia. Lithos, 292, 294-306.

Reiners, P. W., Brady, R., Farley, K. A., Fryxell, J. E., Wernicke, B. P., & Lux, D. (2000). Helium and argon thermochronometry of the Gold Butte block, south Virgin Mountains, Nevada. Earth and Planetary Science Letters, 178(3), 315-326.

Reiners, P. W., Farley, K. A., & Hickes, H. J. (2002). He diffusion and (U–Th)/He thermochronometry of zircon: initial results from Fish Canyon Tuff and Gold Butte. Tectonophysics, 349(1), 297-308.

Reiser, R. F., & Williams, A. J. (1969). Palynology of the Lower Jurassic sediments of the northern Surat Basin, Queensland. SG Reid, Government Printer, 1969.

Rigby, S. M., & Kanstler, A. J. (1987). Murilla Creek - an untested stratigraphic play in the Surat Basin. APPEA Journal, 27, 230-244.

Rosenbaum, G. (2018). The Tasmanides: Phanerozoic tectonic evolution of eastern Australia. Annual Review of Earth and Planetary Sciences(46), 291–325.

Rosenbaum, G., Li, P. F., & Rubatto, D. (2012). The contorted New England Orogen (eastern Australia): New evidence from U-Pb geochronology of early Permian granitoids. Tectonics, 31(1).

Schultz, S. K., MacEachern, J. A., Catuneanu, O., & Dashtgard, S. E. (2020). Coeval deposition of transgressive and normal regressive stratal packages in a structurally controlled area of the Viking Formation, central Alberta, Canada. Sedimentology, 67, 2974-3002.

Sell, B. H., Brown, L. N., & Groves, R. D. (1972). Basal Jurassic sands of the Roma area. Queensland Government Mining Journal, 73:850, 309-321.

Shaanan, U., & Rosenbaum, G. (2016). Detrital zircons as palaeodrainage indicators: insights into southeastern Gondwana from Permian basins in eastern Australia. Basin Research.

Shaanan, U., Rosenbaum, G., & Sihombing, F. M. H. (2017). Continuation of the Ross–Delamerian Orogen: insights from eastern Australian detrital-zircon data. Australian Journal of Earth Sciences, 1-9.

Shaanan, U., Rosenbaum, G., & Campbell, M. J. (2019). Detrital fingerprint: The use of early Precambrian zircon age spectra as unique identifiers of Phanerozoic terranes. Earth and Planetary Science Letters, 506, 97-103.

Sharman, G. R., & Malkowski, M. A. (2020). Needles in a haystack: Detrital zircon U-Pb ages and the maximum depositional age of modern global sediment. Earth-Science Reviews, 203.

Shaw, S. E., & Flood, R. H. (1981). The New England Batholith, eastern Australia: geochemical variations in time and space. Journal of Geophysical Research: Solid Earth, 86(B11), 10530-10544.

Siégel, C. (2015). Heat-producing element enrichment in granitic rocks, the role of crustal composition and evolution. Unpublished PhD thesis, Queensland University of Technology.

Siégel, C., Bryan, S. E., & Allen, C. M. (2017). Detrital rutile geochemistry and geochronology from metasedimentary rocks of the Thomson Orogen, Australia. Paper presented at the Goldschmidt, Paris.

Siégel, C., Bryan, S. E., Allen, C. M., Purdy, D. J., Cross, A. J., Uysal, I. T., & Gust, D. A. (2018). Crustal and thermal structure of the Thomson Orogen: constraints from the geochemistry, zircon U–Pb age, and Hf and O isotopes of subsurface granitic rocks. Australian Journal of Earth Sciences, 65(7-8), 967-986.

Sircombe, K. N. (1999). Tracing provenance through the isotope ages of littoral and sedimentary detrital zircon, eastern Australia. Sedimentary Geology, 124(1-4), 47-67.

Sobczak, K. (2019). Investigating far-field tectonic events as drivers of provenance change in sedimentary basins. Unpublished PhD thesis, Queensland University of Technology.

Strong, N., & Paola, C. (2008). Valleys that never were: time surfaces versus stratigraphic surfaces. Journal of Sedimentary Research, 78(8), 579-593.

Todd, C. N., Roberts, E. M., Knutsen, E. M., Rozefelds, A. C., Huang, H. Q., & Spandler, C. (2019). Refined age and geological context of two of Australia's most important Jurassic vertebrate taxa (Rhoetosaurus brownei and Siderops kehli), Queensland. Gondwana Research 76, 19-25.

Totterdell, J. M., Wells, A. T., Brakel, A. T., Korsch, R. J., & Nicoll, M. G. (1991). Sequence stratigraphic interpretation of seismic data in the Taroom region, Bowen and Surat Basins, Queensland. Bureau of Mineral Resources, Geology and Geophysics. Record 1991/102: 1-61.

Totterdell, J. M., & Krassay, A. A. (1995). Sequence evolution and structural history of the Bowen and Surat basins in northern New South Wales. Paper presented at the 1995 NSW Petroleum Symposium Proceedings: Petroleum Exploration Society of Australia, New South Wales Branch.

Totterdell, J. M., Moloney, J., Korsch, R. J., & Krassay, A. A. (2009). Sequence stratigraphy of the Bowen–Gunnedah and Surat Basins in New South Wales. Australian Journal of Earth Sciences, 56(3), 433-459.

Tucker, R. T., Roberts, E. M., Hu, Y., Kemp, A. I. S., & Salisbury, S. W. (2013). Detrital zircon age constraints for the Winton Formation, Queensland: Contextualizing Australia's Late Cretaceous dinosaur faunas. Gondwana Research, 24(2), 767-779.

Tucker, R. T., Roberts, E. M., Henderson, R. A., & Kemp, A. I. S. (2016). Large igneous province or long-lived magmatic arc along the eastern margin of Australia during the Cretaceous? Insights from the sedimentary record. Geological Society of America Bulletin 128(9-10), 1461-1480.

van Noord, K. A. A. (1999). Deep-marine sedimentation and volcanism in the Silverwood Group, New England Fold Belt, Australia. Unpublished PhD thesis, Queensland University of Technology.

Veevers, J. J. (2001). Atlas of Billion-year earth history of Australia and neighbours in Gondwanaland. Sydney, N.S.W: GEMOC Press.

Veevers, J. J., Belousova, E. A., Saeed, A., Sircombe, K., Cooper, A. F., & Read, S. E. (2006). Pan-Gondwanaland detrital zircons from Australia analysed for Hf-isotopes and trace elements reflect an ice-covered Antarctic provenance of 700–500 Ma age, TDM of 2.0–1.0 Ga, and alkaline affinity. Earth-Science Reviews, 76(3-4), 135-174.

Veevers, J. J., Saeed, A., Pearson, N., Belousova, E. A., & Kinny, P. D. (2008). Zircons and clay from morainal Permian siltstone at Mt Rymill (73 S, 66 E), Prince Charles Mountains, Antarctica, reflect the ancestral Gamburtsev Subglacial Mountains–Vostok Subglacial Highlands complex. Gondwana Research, 14(3), 343-354.

Vermeesch, P. (2012). On the visualisation of detrital age distributions. Chemical Geology, 312-313, 190-194.

Vermeesch, P. (2013). Multi-sample comparison of detrital age distributions. Chemical Geology, 341,140-146.

Vermeesch, P., Resentini, A. and Garzanti, E., (2016). An R package for statistical provenance analysis, Sedimentary Geology, 336, 14-25.

Vermeesch, P. (2018). IsoplotR: a free and open toolbox for geochronology. Geoscience Frontiers, 9, 1479-1493.

Vermeesch, P. (2021). Maximum depositional age estimation revisited. Geoscience Frontiers, 12(2), 843-850.

Vernon, R. H. (1969). The Willyama Complex, Broken Hill area. In Packham GH (Ed.), The Geology of New South Wales. Journal of the Geological Society of Australia, 16, 20-54.

Vickery, N. M., Ashley, P. M., & Fanning, C. M. (1997). Dumboy-Gragin Granite, northeastern New South Wales: Age and compositional affinities. In P.M. Ashley & P. G. Flood (Eds.), Tectonics and metallogenesis of the New England Orogen – Alan H. Voisey Memorial Volume (pp. 266–271). Sydney NSW: Geological Society of Australia Special Publication 19.

von Eynatten, H., Barceló-Vidal, C., & Pawlowsky-Glahn, V. (2003). Composition and discrimination of sandstones: A statistical evaluation of different analytical methods. Journal of Sedimentary Research, 73(1), 47-57.

Wade, B. P., Hand, M., & Barovich, K. M. (2005). Nd isotopic and geochemical constraints on provenance of sedimentary rocks in the eastern Officer Basin, Australia: implications for the duration of the intracratonic Petermann Orogeny. Journal of the Geological Society, 162(3), 513-530.

Wainman, C. C., McCabe, P. J., & Crowley, J. L. (2018). Solving a tuff problem: Defining a chronostratigraphic framework for Middle to Upper Jurassic nonmarine strata in eastern Australia using uranium-lead chemical abrasion–thermal ionization mass spectrometry zircon dates. AAPG Bulletin, 102(6), 1141-1168.

Wainman, C. C., Reynolds, P. H., Hall, T., McCabe, P. J. & Holford, S. P. (2019). Nature and origin of tuff beds in Jurassic strata of the Surat Basin, Australia: implications on the evolution of the eastern margin of Gondwana during the Mesozoic. Journal of Volcanology and Geothermal Research 377, 103-116.

Walsh, A. K., Raimondo, T., Kelsey, D. E., Hand, M., Pfitzner, H. L., & Clark, C. (2013). Duration of high-pressure metamorphism and cooling during the intraplate Petermann Orogeny. Gondwana Research, 24(3-4), 969-983.

Wang, J., La Croix, A. D., Gonzalez, S., He, J., & Underschultz, J. R. (2019). Sequence stratigraphic analysis of the Lower Jurassic Precipice and Evergreen Formations in the Surat Basin, Australia: implications for the architecture of reservoirs and seals for CO_2 storage. Marine and Petroleum Geology, 102, 829-843.

Weltje, G. J. (2006). Ternary sandstone composition and provenance: An evaluation of the 'Dickinson model'. In Vol. 264. Geological Society Special Publication (pp. 79-99).

Wiltshire, M. J. (1989). Mesozoic stratigraphy and palaeogeography, eastern Australia. In The Cooper and Eromanga Basins, Australia, edited by O'Neil B. J. Adelaide: Proceedings of Petroleum Exploration Society of Australia, Society of Petroleum Engineers, Australian Society of Exploration Geophysicists (SA Branches). pp. 279–291

Withnall, I. W., Hutton, L. J., Bultitude, R. J., von Gnielinski, F. E., & Rienks, I. P. (2009). Geology of the Auburn Arch, southern Connors Arch and adjacent parts of the Bowen Basin and Yarrol Province, central Queensland. Queensland Geology, 12, 1-461.

Withnall, I. W. (2013). New England Orogen-Yarrol Province. In P. A. Jell (Ed.), Geology of Queensland (pp. 336-351). Brisbane Qld: Geological Survey of Queensland.

Withnall, I. W. (2019). Review of SHRIMP zircon ages for the Eastern Succession of the Mount Isa Province and magmatic events in its provenance. Queensland Minerals and Energy Review Series, Department of Natural Resources, Mines and Energy, Queensland.

Yago, J. V. R., & Fielding, C. R. (1996). Sedimentology of the Middle Jurassic Walloon Coal Measures in the Great Artesian Basin, eastern Australia. Paper presented at the Mesozoic 96. Proceedings of the Mesozoic Geology of the Eastern Australia Plate Conference, Brisbane, Queensland.

Ziolkowski, V., Hodgkinson, J., McKillop, M., Grigorescu, M., & McKellar, J. L. (2014). Sequence stratigraphic analysis of the Lower Jurassic succession in the Surat Basin, Queensland — preliminary findings. Queensland Minerals and Energy Review Series, Department of Natural Resources and Mines, Queensland.

Appendix A Summary of data from Ciesiolka (2019)

Sample ID	Lab	Well	Depth, m	Stratigraphic unit	LA-ICP-MS results					CA-TIMS results		
					MDA [Ma]	± (1σ) [Ma]	n=	Youngest single grain	± (1σ) [Ma]	Weighted mean [Ma]	± (2σ) [Ma]	n=
PR_11	QUT-CARF	West Wandoan 1	~952	Hutton Sst	183.2	1.9	2	182.6	1.6			
EVG-01	Boise State University	West Wandoan 1	1046.83	Evergreen Fm						184.71	0.21	3
PR_05	QUT-CARF	West Wandoan 1	~1159	Precipice Sst	194.12	1.7	2	193.3	1.7			
372	QUT-CARF	West Wandoan 1	~1169	Precipice Sst	240.95	1.8	2	239.9	1.3			
373	QUT-CARF	West Wandoan 1	~1178	Precipice Sst	287.95	1.2	3	231.8	0.7			
375	QUT-CARF	West Wandoan 1	~1199	Precipice Sst	244.6	4.1	2	232	2.4			
376	QUT-CARF	West Wandoan 1	~1238	Precipice Sst	270.35	1.5	2	229.1	1			
TP-1000	QUT-CARF	Tipton 153	1000?	Evergreen Fm	183.06	6.5	3	181	6.5			
TP-1027	QUT-CARF	Tipton 153	1027?	Precipice Sst	319.4	7	2	242	7			
TP-1037	QUT-CARF	Tipton 153	1037?	Precipice Sst	263.6	12	5	237.5	9.5			
TP-1059	QUT-CARF	Tipton 153	1059?	Precipice Sst	227	7.5	2	195.7	6			
TP-1093	QUT-CARF	Tipton 153	1093?	Precipice Sst	246.75	7.5	2	225	6.5			

Appendix B Detrital zircon LA-ICP-MS dating methodology details

Heavy mineral (>2.95 g/cm^3) separation of all samples was performed by Geotrack International Pty Ltd, Melbourne. Approximately 1 kg of rock per sample was used to yield mineral concentrates.

Mineral grains, were hand-picked using a binocular microscope, avoiding bias towards size or shape, and then mounted in epoxy resin, ground down to expose the grain interiors and polished. The target number of grains for laser ablation was 170 per sample. The polished mounts were carbon-coated and imaged using scanning electron microscopy (SEM) with a VPSE G3 detector (Zeiss Sigma FESEM) to obtain cathodoluminescence (CL) response, to help locate ablation sites away from cracks, inclusions and other grain imperfections. An effort was made to avoid ablating inherited cores but rather zones with the most homogeneous CL response where possible, as well as to avoid ablating multiple age zones in one analysis, which can result in mixed ages (e.g., Zimmermann et al., 2018). In many cases, however, the zircon grains were not significantly larger than the ablation spot size, and potentially ablation of different age domains within grains was unavoidable.

U-Pb Isotopic dating was performed using a LA-ICP-MS Teledyne Analyte Excite laser and Agilent 7900 ICP-MS at the Central Analytical Research Facility at QUT. The samples were analysed during 8 sessions with the following instrument settings:

Session	Samples	Fluence	Repetition rate	Dwell time	Spot size
1	C4-D6 C4-D7 KEGW7-D1 WM1-D3	1.73J/cm²	9hz	30 sec	40 µm
2	KEGW7-D3 KEGW7-D7 T17-D2 WM1-D1 WM1-D5	1.73J/cm²	9hz	30 sec	40 µm
3	KEGW7-D5 T17-D3 T17-D6 T17-D7	1.73J/cm²	9hz	30 sec	40 µm
4	C4-D2 KEGW7-D6 M34-D1 WM1-D4	1.73J/cm²	9hz	30 sec	40 µm
5	C4-D1 C4-D5 KEGW7-D4 WM1-D2	2.51J/cm²	9hz	30 sec	40 µm
6	C4-D3 KEGW7-D2 T17-D5 WM1-D6	2.51J/cm²	9hz	30 sec	40 µm
7	T17-D1	2.51J/cm²	9hz	30 sec	25 µm*
8	C4-D4 M34-D2 T17-D4	2.51J/cm²	9hz	30 sec	40 µm

* Due to the smaller size of the zircons in this sample T17-D1.

Temora-2 (416.78±0.33 Ma; Black et al., 2004) was used as a primary standard. Plešovice zircon (337.13±0.37 Ma; Sláma et al., 2008) and 91500 (1050.1 ± 7.1 Ma; Wiedenbeck, et al., 2004) were used as age control

standards. The synthetic silicate glass NIST 610 (Jochum et al., 2011) was used as a trace element standard. Concentrations of the following major and trace elements were measured in all sessions except session 7: Si, P, Ti, Y, La, Ce, Pr, Nd, Sm, Eu, Gd, Dy, Er, Yb, Lu, Hf, ^{206}Pb, ^{207}Pb, ^{208}Pb, Th and U. Element concentrations measured during session 7 were: Si, P, ^{206}Pb, ^{207}Pb, ^{208}Pb, Th and U. The element concentrations, especially P and La, were used as one of the analytical criteria for individual analyses to be included or excluded from the final dataset. For zircon grains older than 950 Ma, the ^{207}Pb/^{206}Pb ages were used, which have the advantage of not being affected by any later Pb loss events. The ^{206}Pb/^{238}U ages were used for zircon grains younger than 950 Ma because of improved statistical constraints for the ^{206}Pb/^{238}U ages in younger grains compared to ^{207}Pb/^{206}Pb ages. A ^{208}Pb-based common Pb correction was calculated and applied to grains <950 Ma to check for improved concordance. The Pb model used is Cumming and Richards (1975).

References

Black, L. P., Kamo, S. L., Allen, C. M., Davis, D. W., Aleinikoff, J. N., Valley, J. W., . . . Williams, I. S. (2004). Improved 206Pb/238U microprobe geochronology by the monitoring of a trace-element-related matrix effect; SHRIMP, ID–TIMS, ELA–ICP–MS and oxygen isotope documentation for a series of zircon standards. Chemical Geology, 205(1-2), 115-140.

Cumming, G. L., & Richards, J. R. (1975). Ore lead isotope ratios in a continuously changing Earth. Earth and Planetary Science Letters, 28(2), 155-171.

Jochum, K. P., Weis, U., Stoll, B., Kuzmin, D., Yang, Q., Raczek, I., . . . Frick, D. A. (2011). Determination of reference values for NIST SRM 610–617 glasses following ISO guidelines. Geostandards and Geoanalytical Research, 35(4), 397-429.

Sláma, J., Košler, J., Condon, D. J., Crowley, J. L., Gerdes, A., Hanchar, J. M., . . . Norberg, N. (2008). Plešovice zircon—a new natural reference material for U–Pb and Hf isotopic microanalysis. Chemical Geology, 249(1-2), 1-35.

Wiedenbeck, M., Hanchar, J. M., Peck, W. H., Sylvester, P. J., Valley, J. W., Whitehouse, M. J., . . . Fiebig, J. (2004). Further characterisation of the 91500 zircon crystal. Geostandards and Geoanalytical Research, 28(1), 9-39.

Zimmermann, S., Mark, C., Chew, D., & Voice, P. J. (2018). Maximising data and precision from detrital zircon U-Pb analysis by LA-ICPMS: The use of core-rim ages and the single-analysis concordia age. Sedimentary Geology, 375, 5-13.

Appendix C CA-TIMS dating methodology details

Preliminary LA-ICP-MS dating methods

Zircon grains were separated from rocks using standard techniques, annealed at 900ºC for 60 hours in a muffle furnace, and mounted in epoxy and polished until their centres were exposed. Cathodoluminescence (CL) images were obtained with a JEOL JSM-300 scanning electron microscope and Gatan MiniCL. Zircon was analysed by laser ablation inductively coupled plasma mass spectrometry (LA-ICPMS) using an iCAP RQ Quadrupole ICP-MS and Teledyne Photon Machines Analyte Excite+ 193 nm excimer laser ablation system with HelEx II Active two-volume ablation cell. In-house analytical protocols, standard materials, and data reduction software were used for acquisition and calibration of U-Pb dates and a suite of high field strength elements (HFSE) and rare earth elements (REE). Zircon was ablated with a laser spot of 20 µm wide using fluence and pulse rates of 3 J/cm^2 and 10 Hz, respectively, during a 35-second analysis (15-sec gas blank, 20-sec ablation) that excavated a pit ~8 µm deep. Ablated material was carried by a 0.5 L/min He gas stream in the inner cell and a 1.1 L/min He gas stream in the outer cell. Dwell times were 10 ms for Si, 1 ms for Zr, 5 ms for Hf, 200 ms for ^{49}Ti and ^{207}Pb, 100 ms for ^{206}Pb, 20 ms for ^{202}Hg and ^{204}Pb, 10 ms for ^{238}U, and 10 ms for all other HFSE and REE. Background count rates for each analyte were obtained prior to each spot analysis and subtracted from the raw count rate for each analyte. Ablations pits that appear to have intersected glass or mineral inclusions were identified based on Ti and P. U-Pb dates from these analyses are considered valid if the U-Pb ratios appear to have been unaffected by the inclusions. Analyses that appear contaminated by common Pb were rejected based on mass 204 being above baseline. For concentration calculations, background-subtracted count rates for each analyte were internally normalized to ^{29}Si and calibrated with respect to NIST SRM-610 and -612 glasses as the primary standards. Temperature was calculated from the Ti-in-zircon thermometer (Watson et al., 2006). Because there are no constraints on the activity of TiO_2, an average value in crustal rocks of 0.6 was used.

Data were obtained in two experiments in September 2021. For U-Pb and ^{207}Pb/^{206}Pb dates, instrumental fractionation of the background-subtracted ratios was corrected and dates were calibrated with respect to interspersed measurements of zircon standards and reference materials. The primary standard Plešovice zircon (Sláma et al., 2008) was used to monitor time-dependent instrumental fractionation based on two analyses for every 12 analyses of unknown zircon. A secondary correction to the ^{206}Pb/^{238}U dates was made based on results from the zircon standards Seiland (531 Ma, unpublished data, Boise State University) and 91500 (1065 Ma, Wiedenbeck et al., 1995), which were treated as unknowns and measured, which were treated as unknowns and measured once for every 12 analyses of unknown zircon. These results showed a linear age bias of several per cent that is related to the ^{206}Pb count rate. The secondary correction is thought to mitigate matrix-dependent variations due to contrasting compositions and ablation characteristics between the Plešovice zircon and other standards (and unknowns).

Radiogenic isotope ratio and age error propagation for all analyses include uncertainty contributions from counting statistics and background subtraction. Errors without and with the standard calibration uncertainty are shown in the data table. Errors on single analyses without the standard calibration uncertainty are given below. This uncertainty is the local standard deviation of the polynomial fit to the interspersed primary standard measurements versus time for the time-dependent, relatively larger U/Pb fractionation factor, and the standard error of the mean of the consistently time-invariant and smaller ^{207}Pb/^{206}Pb fractionation factor. These uncertainties are 1.3-1.4% (2σ) for ^{206}Pb/^{238}U and 0.3% (2σ) for ^{207}Pb/^{206}Pb. Age interpretations are based on ^{206}Pb/^{238}U dates. Errors are at 2σ.

CA-TIMS geochronology methods

U-Pb dates were obtained by the chemical abrasion isotope dilution thermal ionization mass spectrometry (CA-TIMS) method from analyses composed of single zircon grains (Table 1), modified after Mattinson (2005). Zircon was removed from the epoxy mounts for dating based on CL images and LA-ICPMS data.

Zircon was put into 3 ml Teflon PFA beakers and loaded into 300 µl Teflon PFA microcapsules. Fifteen microcapsules were placed in a large-capacity Parr vessel and the zircon partially dissolved in 120 µl of 29 M HF for 12 hours at 190°C. Zircon was returned to 3 ml Teflon PFA beakers, HF was removed, and zircon was immersed in 3.5 M HNO_3, ultrasonically cleaned for an hour, and fluxed on a hotplate at 80°C for an hour. The HNO_3 was removed and zircon was rinsed twice in ultrapure H_2O before being reloaded into the 300 µl Teflon PFA microcapsules (rinsed and fluxed in 6 M HCl during sonication and washing of the zircon) and spiked with the EARTHTIME mixed ^{233}U-^{235}U-^{205}Pb tracer solution (ET535). Zircon was dissolved in Parr vessels in 120 µl of 29 M HF with a trace of 3.5 M HNO_3 at 220°C for 48 hours, dried to fluorides, and re-dissolved in 6 M HCl at 180°C overnight. U and Pb were separated from the zircon matrix using an HCl-based anion-exchange chromatographic procedure (Krogh, 1973), eluted together and dried with 2 µl of 0.05 M H_3PO_4.

Pb and U were loaded on a single outgassed Re filament in 5 µl of a silica-gel/phosphoric acid mixture (Gerstenberger and Haase, 1997), and U and Pb isotopic measurements made on a GV Isoprobe-T multicollector thermal ionization mass spectrometer equipped with an ion-counting Daly detector. Pb isotopes were measured by peak-jumping all isotopes on the Daly detector for 160 cycles, and corrected for 0.16 ± 0.03%/a.m.u. (1σ) mass fractionation. Transitory isobaric interferences due to high-molecular weight organics, particularly on ^{204}Pb and ^{207}Pb, disappeared within approximately 30 cycles, while ionization efficiency averaged 10^4 cps/pg of each Pb isotope. Linearity (to ≥1.4 x 10^6 cps) and the associated deadtime correction of the Daly detector were determined by analysis of NBS982. Uranium was analyzed as UO_2^+ ions in static Faraday mode on 10^{12} ohm resistors for 300 cycles, and corrected for isobaric interference of $^{233}U^{18}O^{16}O$ on $^{235}U^{16}O^{16}O$ with an $^{18}O/^{16}O$ of 0.00206. Ionization efficiency averaged 20 mV/ng of each U isotope. U mass fractionation was corrected using the known $^{233}U/^{235}U$ ratio of the ET535 tracer solution.

CA-TIMS U-Pb dates and uncertainties were calculated using the algorithms of Schmitz and Schoene (2007), ET535 tracer solution (Condon et al., 2015) with calibration of $^{235}U/^{205}Pb$ = 100.233, $^{233}U/^{235}U$ = 0.99506, and $^{205}Pb/^{204}Pb$ = 11268, and U decay constants recommended by Jaffey et al. (1971) and $^{238}U/^{235}U$ of 137.818 (Hiess et al., 2012). $^{206}Pb/^{238}U$ ratios and dates were corrected for initial ^{230}Th disequilibrium using $D_{Th/U}$ = 0.2 ± 0.1 (2σ) and the algorithms of Crowley et al. (2007), resulting in an increase in the $^{206}Pb/^{238}U$ dates of ~0.09 Ma. All common Pb in analyses was attributed to laboratory blank and subtracted based on the measured laboratory Pb isotopic composition and associated uncertainty. U blanks are estimated at 0.013 pg. Errors are at 2σ. Age interpretations are based on $^{206}Pb/^{238}U$ dates.

CA-IMS geochronology results

Fifty-eight grains from MCCYU-01 analysed by LA-ICPMS yield dates from 192 ± 9 to 172 ± 8 Ma. Seven grains were analysed by CA-TIMS. The six youngest dates yield a weighted mean of 179.90 ± 0.05 / 0.07 / 0.20 Ma (Mean Square Weighted Deviation = 1.4, probability of fit = 0.20). This is the interpreted depositional age. One other date is 180.25 ± 0.12 Ma.

Sixty-one grains from WM1-T1 analysed by LA-ICPMS yield dates from 573 ± 22 to 188 ± 8 Ma.

References for CA-TIMS dating methodology

Condon D.J., Schoene B., McLean N.M., Bowring S.A., Parrish R, 2015, Metrology and traceability of U-Pb isotope dilution geochronology (EARTHTIME Tracer Calibration Part I): Geochimica et Cosmochimica Acta 164: 464-480.

Crowley, J.L., Schoene, B., Bowring, S.A., 2007, U-Pb dating of zircon in the Bishop Tuff at the millennial scale: Geology 35: 1123-1126.

Gerstenberger, H., Haase, G., 1997, A highly effective emitter substance for mass spectrometric Pb isotope ratio determinations: Chemical Geology 136: 309-312.

Hiess, J., Condon, D.J., McLean, N., Noble, S. R., 2012, 238U/235U systematics in terrestrial uranium-bearing minerals: Science 335: 1610-1614.

Jaffey, A.H., Flynn, K.F., Glendenin, L.E., Bentley, W.C., Essling, A.M., 1971, Precision measurements of half-lives and specific activities of ^{235}U and ^{238}U: Physical Review C, 4: 1889-1906.

Krogh, T.E., 1973, A low contamination method for hydrothermal decomposition of zircon and extraction of U and Pb for isotopic age determination: Geochimica et Cosmochimica Acta 37: 485-494.

Ludwig, K.R., 2003, User's Manual for Isoplot 3.00. Berkeley Geochronology Center: Berkeley, CA, 70 p.

Mattinson, J.M., 2005, Zircon U-Pb chemical abrasion ("CA-TIMS") method: combined annealing and multi-step partial dissolution analysis for improved precision and accuracy of zircon ages: Chemical Geology 220:47-66.

Schmitz, M.D., Schoene, B., 2007, Derivation of isotope ratios, errors and error correlations for U-Pb geochronology using ^{205}Pb-^{235}U-(^{233}U)-spiked isotope dilution thermal ionization mass spectrometric data: Geochemistry, Geophysics, Geosystems (G^3) 8, Q08006, doi:10.1029/2006GC001492.

Sláma, J., Košler, J, Condon, D.J., Crowley, J.L., Gerdes, A., Hanchar, J.M., Horstwood, M.S.A., Morris, G.A., Nasdala, L., Norberg, N., Schaltegger, U., Schoene, B. Tubrett, M.N, Whitehouse, M.J., 2008, Plešovice zircon — A new natural reference material for U–Pb and Hf isotopic microanalysis. Chemical Geology, 249: 1-35.

Watson, E.B., Wark, D.A., Thomas, J.B., 2006, Crystallization themometers for zircon and rutile. Contributions to Mineralogy and Petrology, 151: 413-433.

Wiedenbeck, M., Alle, P., Corfu, F., Griffin, W., Meier, M., Oberli, F., Quadt, A.V., Roddick, J., Spiegel, W. 1995, Three natural zircon standards for U-Th-Pb, Lu-Hf, trace element and REE Analyses. Geostandards Newsletter, 19: 1-23.

Appendix D Sandstone petrography – point counting results

Point counting for Chinchilla 4 and Kenya East GW7 was carried out as part of this study, data for West Moonie 1 are from unpublished petrography report by CTSCo, and data for West Wandoan 1 and Tipton 153 are from Ciesiolka (2019). The differences in individual grain framework components selected for counting result from different approaches taken in these three studies. However, the final QFL percentages are normalised for the whole dataset. Note that results from the CTSCo petrography report are given in percentages only, and the absolute numbers of counts are unknown.

Sample ID	Well	Quartz (Mono)	Quartz (poly)	Feldspar	Metamorphic rock fragments	Sedimentary rock fragments	Volcanic rock fragments	Plutonic rock fragments	Unidentified rock fragments	Mica	Quartz overgrowths	Authigenic kaolinite	Authigenic illite	Siderite	Matrix	Total counts	Q	F	L
WM1_PET01	West Moonie 1	40.6%	3.3%	11.7%	4%	12%	5%			0%	0.7%	16.5%	1.3%	4.3%		Unknown	**57.3%**	**15.3%**	**27.4%**
WM1_PET04	West Moonie 1	59.6%	3.3%	6.7%	0.3%	4%	2.3%			0%	5.4%	5.3%	0%	0%		Unknown	**83.5%**	**8.8%**	**7.7%**
WM1_PET05	West Moonie 1	61.3%	7.3%	0%	4.3%	4.4%	1.7%			0.3%	4.7%	9.4%	0.3%	0%		Unknown	**87.7%**	**0.0%**	**12.3%**
WM1_PET03	West Moonie 1	71.3%	4.7%	0%	0%	0%	0%			0%	5.7%	3.3%	0%	0.3%		Unknown	**100.0%**	**0.0%**	**0.0%**
WM1_PET02	West Moonie 1	67.3%	6.4%	0%	0%	0.3%	0%				5%	0.7%	0%	0%		Unknown	**100.0%**	**0.0%**	**0.0%**
C4-P1	Chinchilla 4	400	1	55	7	2	16	0	54						46	581	**401**	**55**	**79**
																	75.0%	**10.3%**	**14.8%**
C4-D2	Chinchilla 4	263	2	78	7	3	33	0	123						31	540	**265**	**78**	**166**
																	52.1%	**15.3%**	**32.6%**
C4-D3	Chinchilla 4	220	4	108	7	0	70	0	100						83	592	**224**	**108**	**177**
																	44.0%	**21.2%**	**34.8%**
C4-D4	Chinchilla 4	300	3	91	12	1	35	2	69						48	561	**303**	**91**	**119**
																	59.1%	**17.7%**	**23.2%**
KEGW7-P2	Kenya East GW7	287	14	112	14	7	18	3	66						79	600	**301**	**112**	**108**
																	57.8%	**21.5%**	**20.7%**
KEGW7-D2	Kenya East GW7	228	14	99	27	25	61	0	47						57	558	**242**	**99**	**160**
																	48.3%	**19.8%**	**31.9%**
KEGW7-D3	Kenya East GW7	255	7	120	12	12	39	0	74						67	586	**262**	**120**	**137**
																	50.5%	**23.1%**	**26.4%**
KEGW7-D4	Kenya East GW7	362	14	76	19	5	9	1	35						22	543	**376**	**76**	**69**
																	72.2%	**14.6%**	**13.2%**
KEGW7-D5	Kenya East GW7	469	7	20	7	8	1	0	4						6	522	**476**	**20**	**20**
																	92.2%	**3.9%**	**3.9%**
PR_05	West Wandoan 1								11							302	**279**	**9**	**14**
																	92.4%	**3.0%**	**4.6%**
372	West Wandoan 1								0							301	**295**	**0**	**6**
																	98.0%	**0.0%**	**2.0%**
373	West Wandoan 1								0							302	**298**	**0**	**4**
																	98.7%	**0.0%**	**1.3%**
375	West Wandoan 1								0							300	**290**	**0**	**10**
																	96.7%	**0.0%**	**3.3%**
376	West Wandoan 1								0							302	**295**	**0**	**7**
																	97.7%	**0.0%**	**2.3%**
363	West Wandoan 1								68							356	**180**	**104**	**72**
																	50.6%	**29.2%**	**20.2%**
364	West Wandoan 1								41							356	**208**	**64**	**84**
																	58.4%	**18.0%**	**23.6%**
TP01000	Tipton 153								10							311	**294**	**12**	**5**
																	94.5%	**3.9%**	**1.6%**
TP01027	Tipton 153								0							301	**297**	**0**	**4**
																	98.7%	**0.0%**	**1.3%**
TP01037	Tipton 153								0							306	**298**	**0**	**8**
																	97.4%	**0.0%**	**2.6%**
TP01059	Tipton 153								0							304	**298**	**0**	**6**
																	98.0%	**0.0%**	**2.0%**
TP01093	Tipton 153								0							305	**296**	**0**	**9**
																	97.1%	**0.0%**	**3.0%**

Appendix E Radial plots

Radial plots used to visualise detrital age distributions and calculate maximum depositional ages using the Maximum Likelihood Algorithm (Vermeesch, 2021). Plots were generated in IsoplotR (Vermeesch, 2018). Uncertainties are given at both 1σ and 2σ.

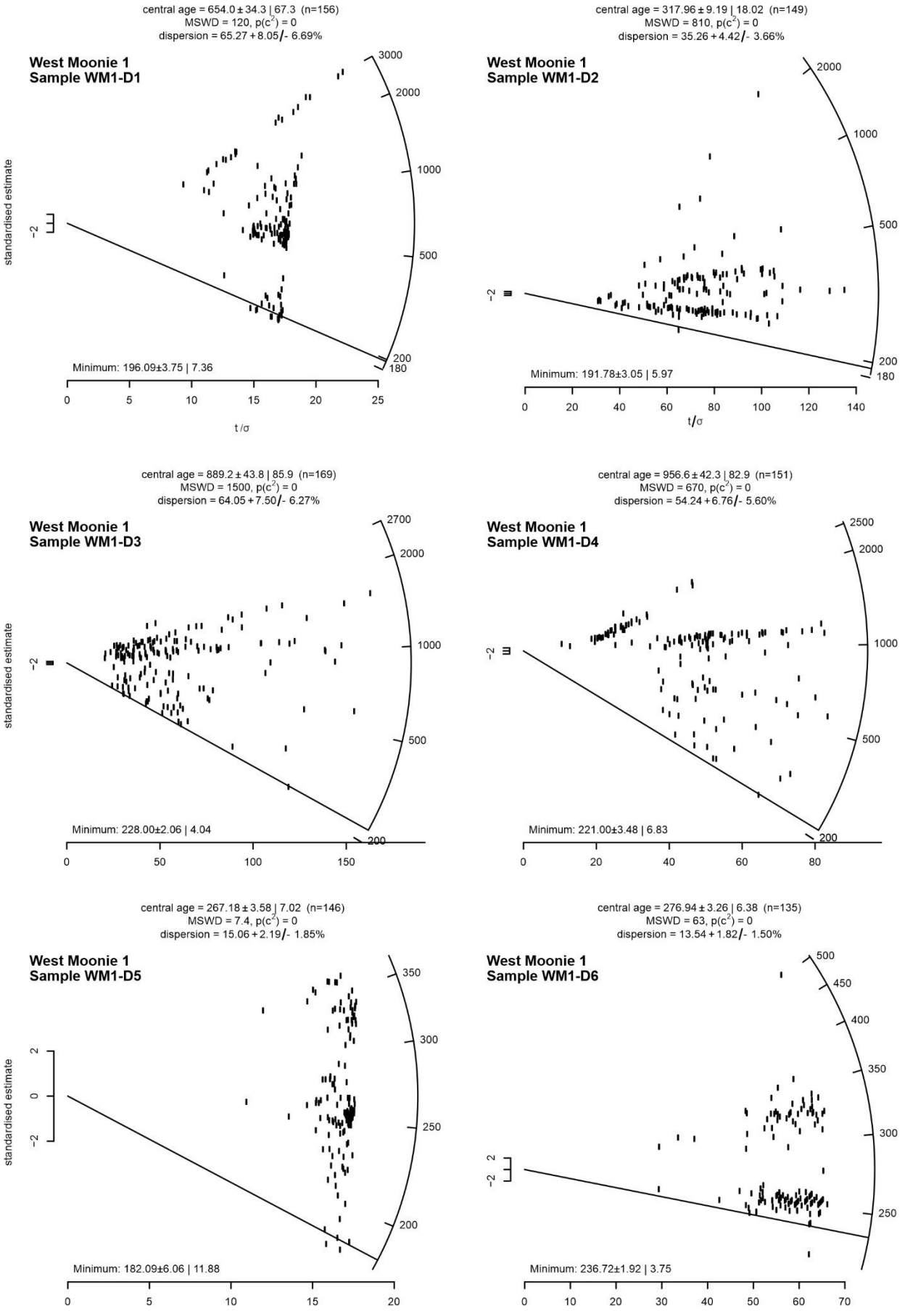
central age = 654.0 ± 34.3 | 67.3 (n=156)
MSWD = 120, p(c²) = 0
dispersion = 65.27 + 8.05/- 6.69%
West Moonie 1
Sample WM1-D1
standardised estimate
Minimum: 196.09±3.75 | 7.36
t/σ
central age = 317.96 ± 9.19 | 18.02 (n=149)
MSWD = 810, p(c²) = 0
dispersion = 35.26 + 4.42/- 3.66%
West Moonie 1
Sample WM1-D2
Minimum: 191.78±3.05 | 5.97
t/σ
central age = 889.2 ± 43.8 | 85.9 (n=169)
MSWD = 1500, p(c²) = 0
dispersion = 64.05 + 7.50/- 6.27%
West Moonie 1
Sample WM1-D3
standardised estimate
Minimum: 228.00±2.06 | 4.04
central age = 956.6 ± 42.3 | 82.9 (n=151)
MSWD = 670, p(c²) = 0
dispersion = 54.24 + 6.76/- 5.60%
West Moonie 1
Sample WM1-D4
Minimum: 221.00±3.48 | 6.83
central age = 267.18 ± 3.58 | 7.02 (n=146)
MSWD = 7.4, p(c²) = 0
dispersion = 15.06 + 2.19/- 1.85%
West Moonie 1
Sample WM1-D5
standardised estimate
Minimum: 182.09±6.06 | 11.88
central age = 276.94 ± 3.26 | 6.38 (n=135)
MSWD = 63, p(c²) = 0
dispersion = 13.54 + 1.82/- 1.50%
West Moonie 1
Sample WM1-D6
Minimum: 236.72±1.92 | 3.75

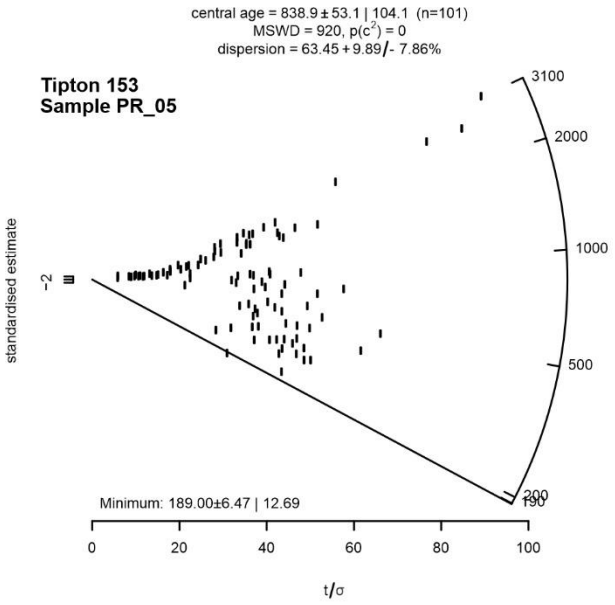
central age = 838.9 ± 53.1 | 104.1 (n=101)
MSWD = 920, p(c²) = 0
dispersion = 63.45 + 9.89 /- 7.86%
Tipton 153
Sample PR_05
standardised estimate
Minimum: 189.00±6.47 | 12.69
t/σ

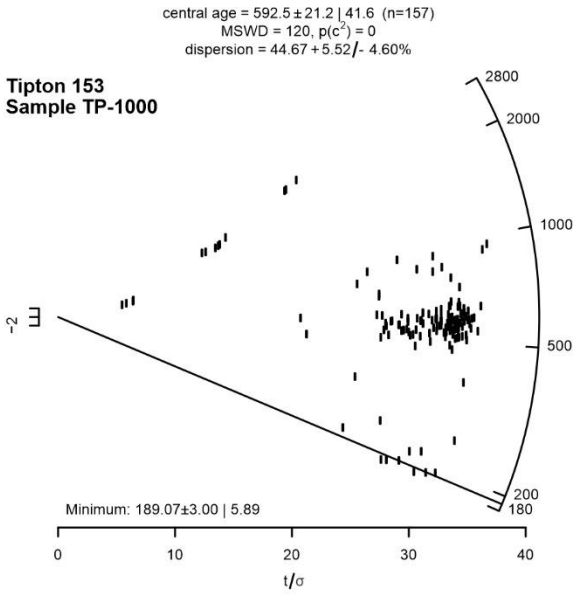
central age = 592.5 ± 21.2 | 41.6 (n=157)
MSWD = 120, p(c²) = 0
dispersion = 44.67 + 5.52 /- 4.60%
Tipton 153
Sample TP-1000
Minimum: 189.07±3.00 | 5.89
t/σ

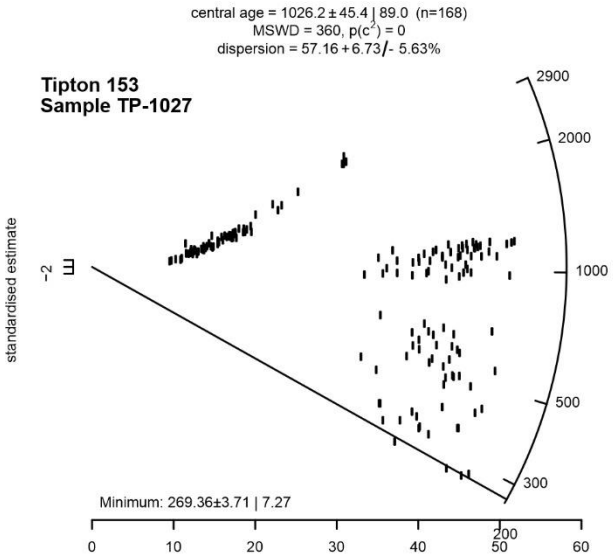
central age = 1026.2 ± 45.4 | 89.0 (n=168)
MSWD = 360, p(c²) = 0
dispersion = 57.16 + 6.73 /- 5.63%
Tipton 153
Sample TP-1027
standardised estimate
Minimum: 269.36±3.71 | 7.27

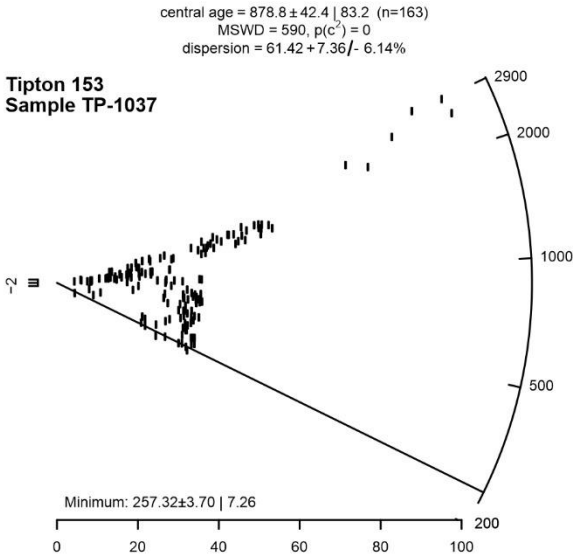
central age = 878.8 ± 42.4 | 83.2 (n=163)
MSWD = 590, p(c²) = 0
dispersion = 61.42 + 7.36 /- 6.14%
Tipton 153
Sample TP-1037
Minimum: 257.32±3.70 | 7.26

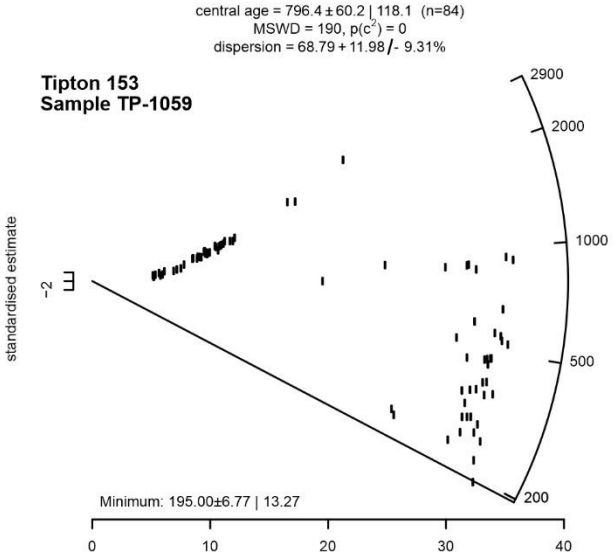
central age = 796.4 ± 60.2 | 118.1 (n=84)
MSWD = 190, p(c²) = 0
dispersion = 68.79 + 11.98 /- 9.31%
Tipton 153
Sample TP-1059
standardised estimate
Minimum: 195.00±6.77 | 13.27

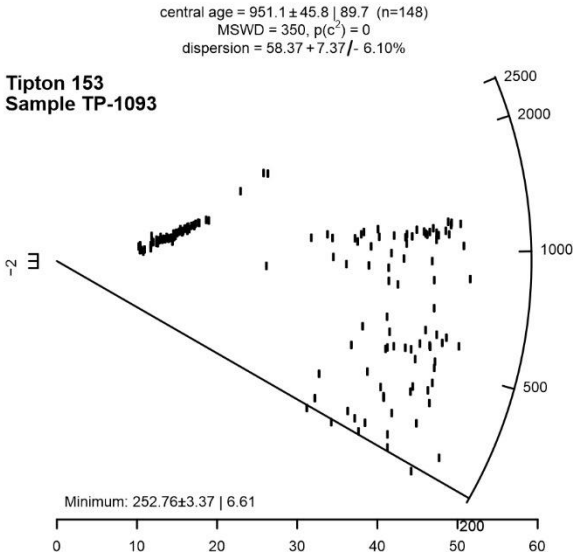
central age = 951.1 ± 45.8 | 89.7 (n=148)
MSWD = 350, p(c²) = 0
dispersion = 58.37 + 7.37 /- 6.10%
Tipton 153
Sample TP-1093
Minimum: 252.76±3.37 | 6.61

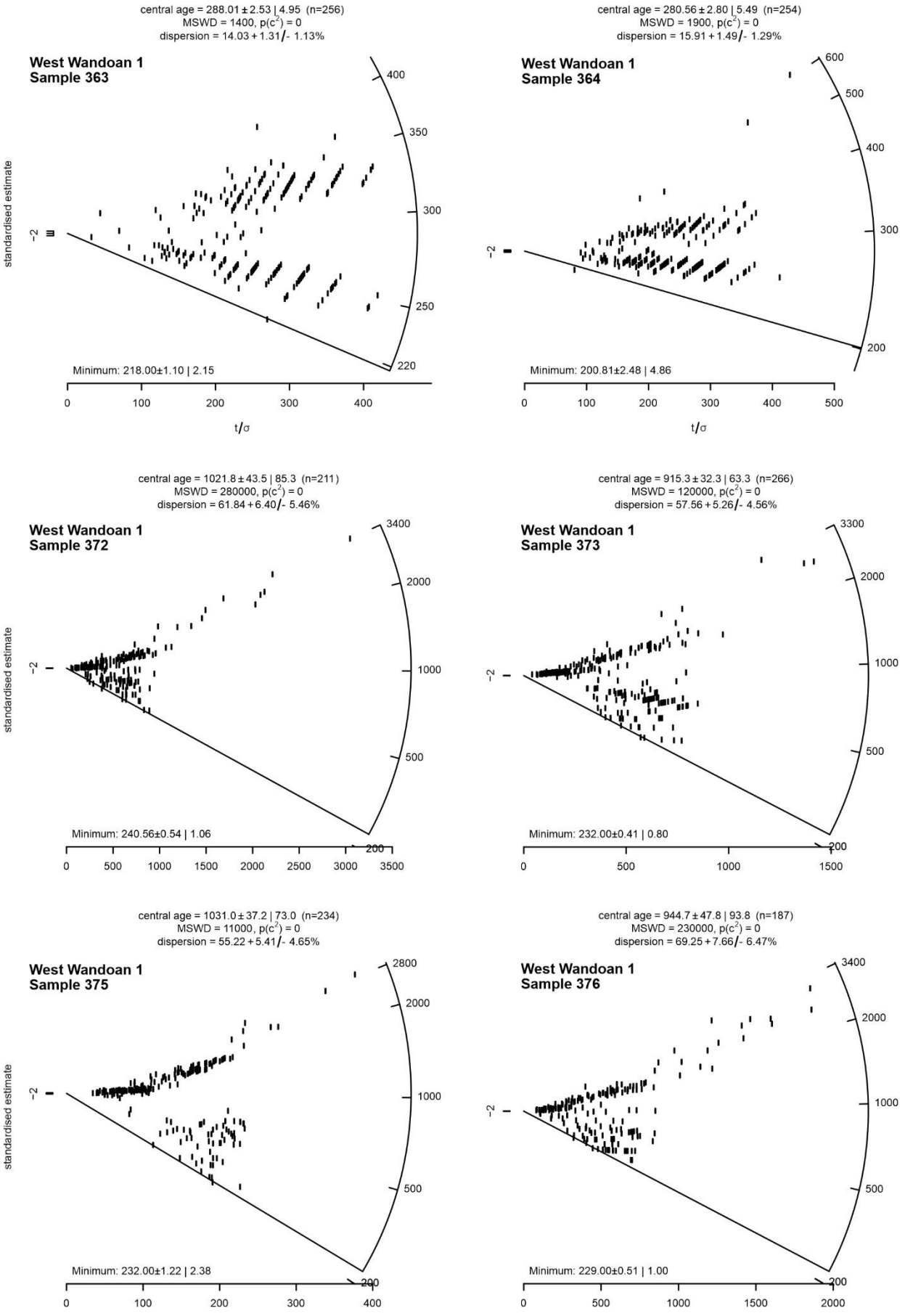
central age = 288.01 ± 2.53 | 4.95 (n=256)
MSWD = 1400, p(c²) = 0
dispersion = 14.03 + 1.31/- 1.13%
West Wandoan 1
Sample 363
standardised estimate
Minimum: 218.00±1.10 | 2.15
t/σ
central age = 280.56 ± 2.80 | 5.49 (n=254)
MSWD = 1900, p(c²) = 0
dispersion = 15.91 + 1.49/- 1.29%
West Wandoan 1
Sample 364
Minimum: 200.81±2.48 | 4.86
t/σ
central age = 1021.8 ± 43.5 | 85.3 (n=211)
MSWD = 280000, p(c²) = 0
dispersion = 61.84 + 6.40/- 5.46%
West Wandoan 1
Sample 372
standardised estimate
Minimum: 240.56±0.54 | 1.06
central age = 915.3 ± 32.3 | 63.3 (n=266)
MSWD = 120000, p(c²) = 0
dispersion = 57.56 + 5.26/- 4.56%
West Wandoan 1
Sample 373
Minimum: 232.00±0.41 | 0.80
central age = 1031.0 ± 37.2 | 73.0 (n=234)
MSWD = 11000, p(c²) = 0
dispersion = 55.22 + 5.41/- 4.65%
West Wandoan 1
Sample 375
standardised estimate
Minimum: 232.00±1.22 | 2.38
central age = 944.7 ± 47.8 | 93.8 (n=187)
MSWD = 230000, p(c²) = 0
dispersion = 69.25 + 7.66/- 6.47%
West Wandoan 1
Sample 376
Minimum: 229.00±0.51 | 1.00

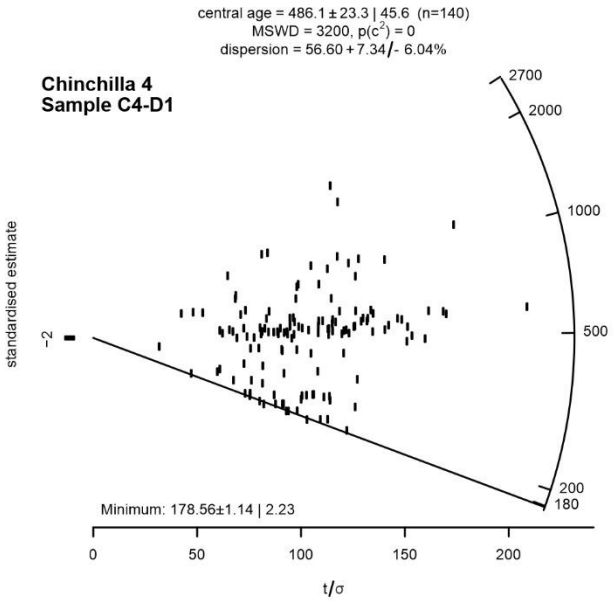
central age = 486.1 ± 23.3 | 45.6 (n=140)
MSWD = 3200, p(c²) = 0
dispersion = 56.60 + 7.34/- 6.04%
Chinchilla 4
Sample C4-D1
standardised estimate
Minimum: 178.56±1.14 | 2.23
t/σ

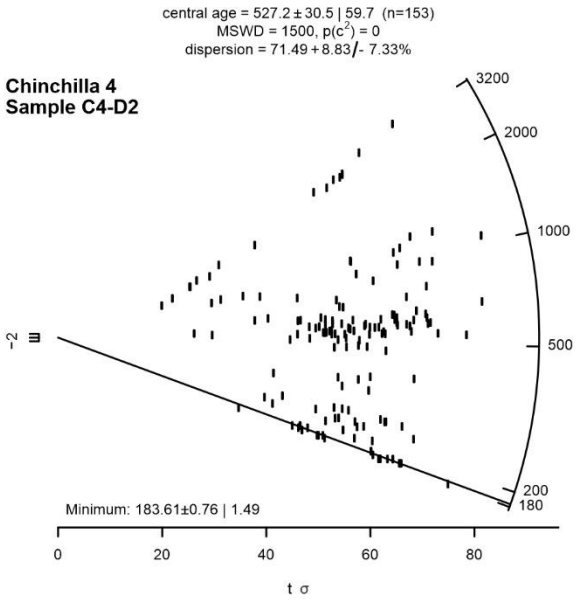
central age = 527.2 ± 30.5 | 59.7 (n=153)
MSWD = 1500, p(c²) = 0
dispersion = 71.49 + 8.83/- 7.33%
Chinchilla 4
Sample C4-D2
Minimum: 183.61±0.76 | 1.49
t σ

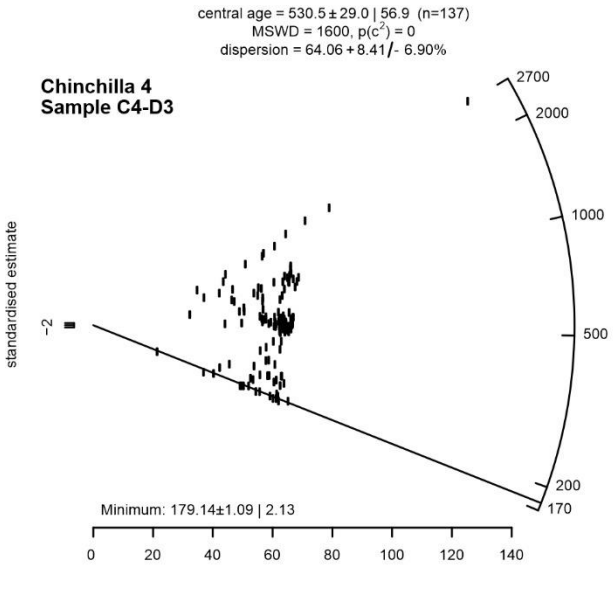
central age = 530.5 ± 29.0 | 56.9 (n=137)
MSWD = 1600, p(c²) = 0
dispersion = 64.06 + 8.41/- 6.90%
Chinchilla 4
Sample C4-D3
standardised estimate
Minimum: 179.14±1.09 | 2.13

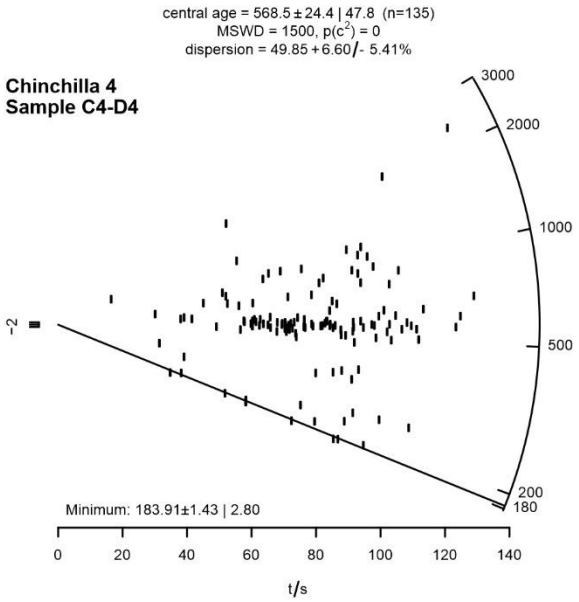
central age = 568.5 ± 24.4 | 47.8 (n=135)
MSWD = 1500, p(c²) = 0
dispersion = 49.85 + 6.60/- 5.41%
Chinchilla 4
Sample C4-D4
Minimum: 183.91±1.43 | 2.80
t/s

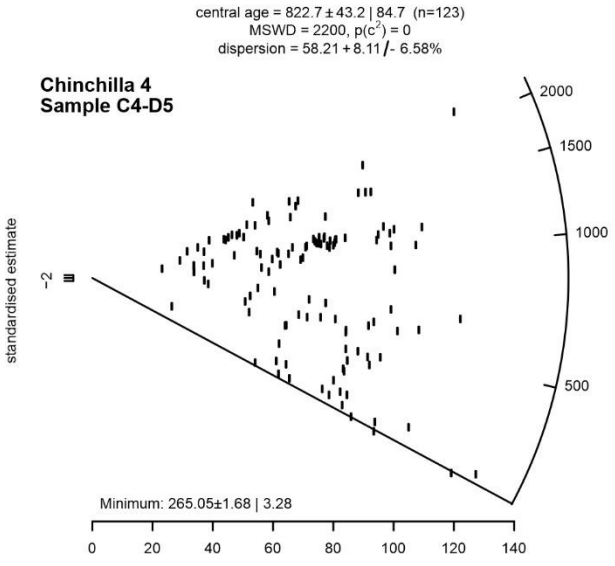
central age = 822.7 ± 43.2 | 84.7 (n=123)
MSWD = 2200, p(c²) = 0
dispersion = 58.21 + 8.11/- 6.58%
Chinchilla 4
Sample C4-D5
standardised estimate
Minimum: 265.05±1.68 | 3.28

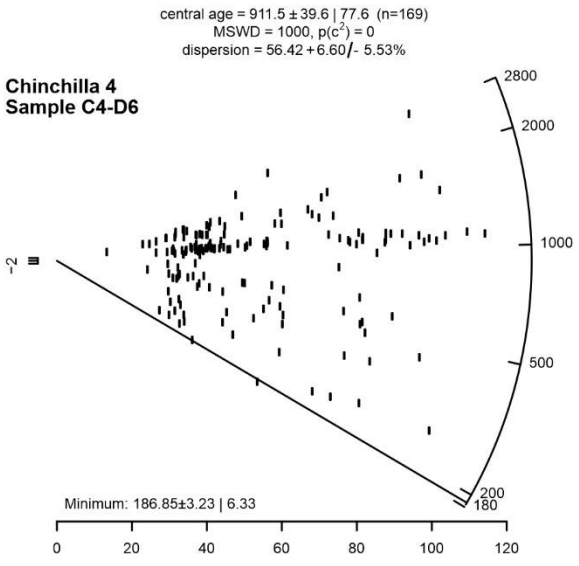
central age = 911.5 ± 39.6 | 77.6 (n=169)
MSWD = 1000, p(c²) = 0
dispersion = 56.42 + 6.60/- 5.53%
Chinchilla 4
Sample C4-D6
Minimum: 186.85±3.23 | 6.33

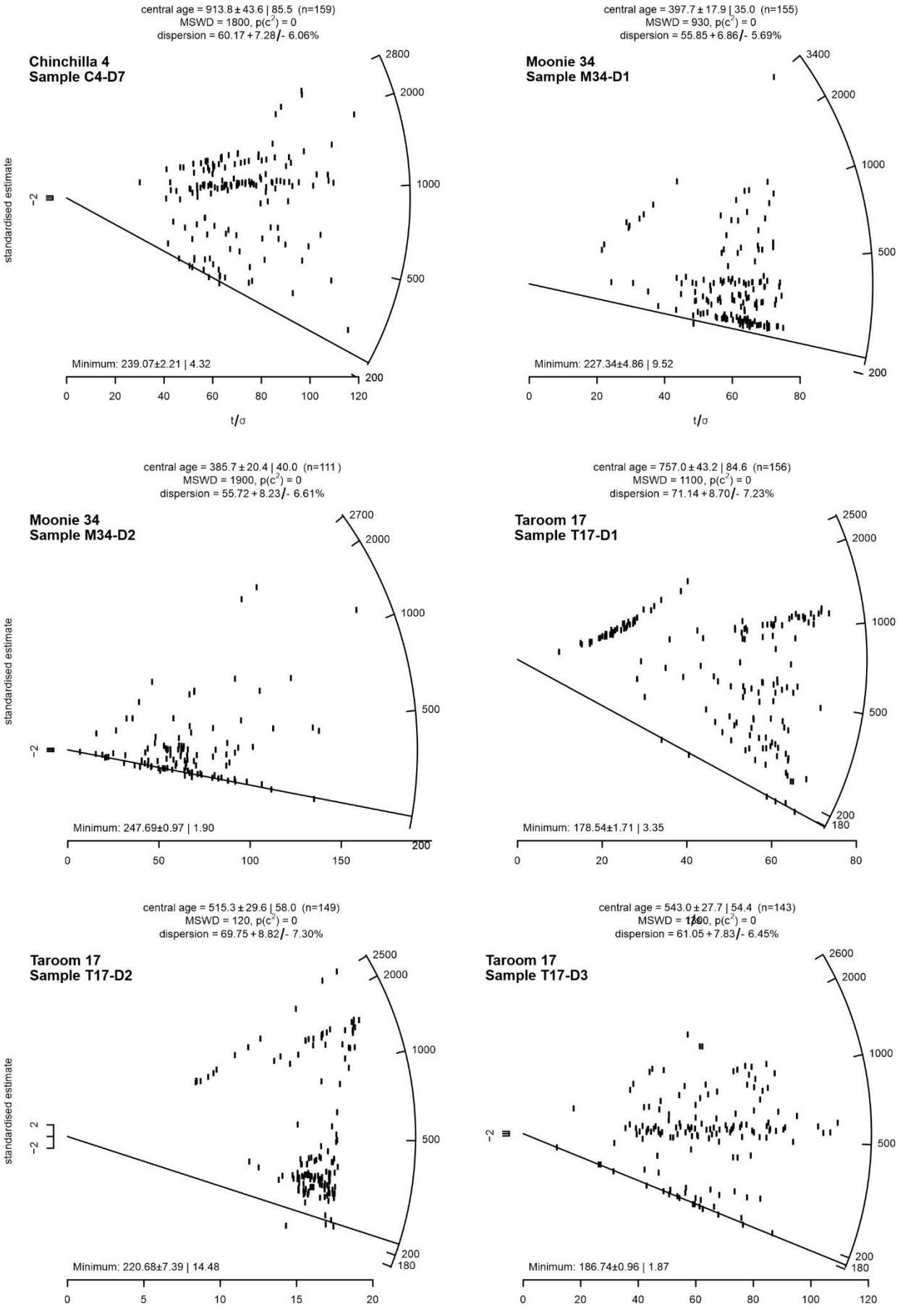
central age = 913.8 ± 43.6 | 85.5 (n=159)
MSWD = 1800, p(c²) = 0
dispersion = 60.17 + 7.28/- 6.06%
Chinchilla 4
Sample C4-D7
standardised estimate
Minimum: 239.07±2.21 | 4.32
t/σ
central age = 397.7 ± 17.9 | 35.0 (n=155)
MSWD = 930, p(c²) = 0
dispersion = 55.85 + 6.86/- 5.69%
Moonie 34
Sample M34-D1
Minimum: 227.34±4.86 | 9.52
t/σ
central age = 385.7 ± 20.4 | 40.0 (n=111)
MSWD = 1900, p(c²) = 0
dispersion = 55.72 + 8.23/- 6.61%
Moonie 34
Sample M34-D2
standardised estimate
Minimum: 247.69±0.97 | 1.90
central age = 757.0 ± 43.2 | 84.6 (n=156)
MSWD = 1100, p(c²) = 0
dispersion = 71.14 + 8.70/- 7.23%
Taroom 17
Sample T17-D1
Minimum: 178.54±1.71 | 3.35
central age = 515.3 ± 29.6 | 58.0 (n=149)
MSWD = 120, p(c²) = 0
dispersion = 69.75 + 8.82/- 7.30%
Taroom 17
Sample T17-D2
standardised estimate
Minimum: 220.68±7.39 | 14.48
central age = 543.0 ± 27.7 | 54.4 (n=143)
MSWD = 1200, p(c²) = 0
dispersion = 61.05 + 7.83/- 6.45%
Taroom 17
Sample T17-D3
Minimum: 186.74±0.96 | 1.87

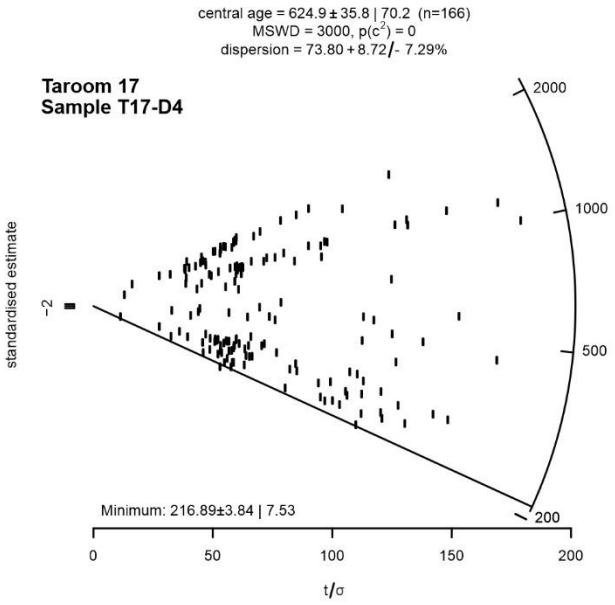
central age = 624.9 ± 35.8 | 70.2 (n=166)
MSWD = 3000, p(c²) = 0
dispersion = 73.80 + 8.72/- 7.29%
Taroom 17
Sample T17-D4
standardised estimate
Minimum: 216.89±3.84 | 7.53
t/σ

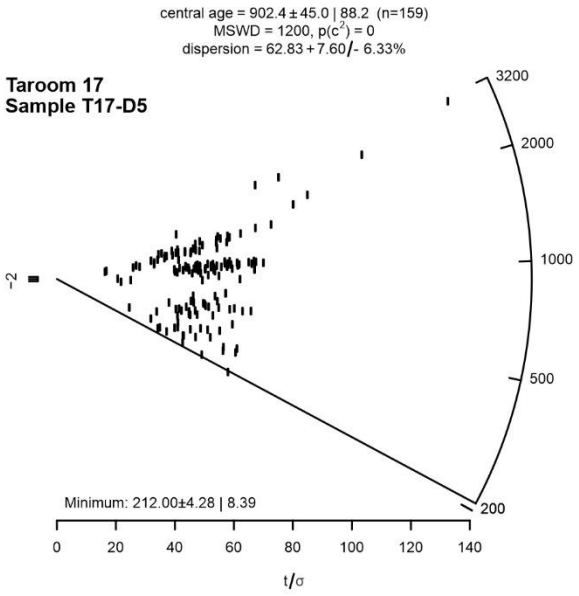
central age = 902.4 ± 45.0 | 88.2 (n=159)
MSWD = 1200, p(c²) = 0
dispersion = 62.83 + 7.60/- 6.33%
Taroom 17
Sample T17-D5
Minimum: 212.00±4.28 | 8.39
t/σ

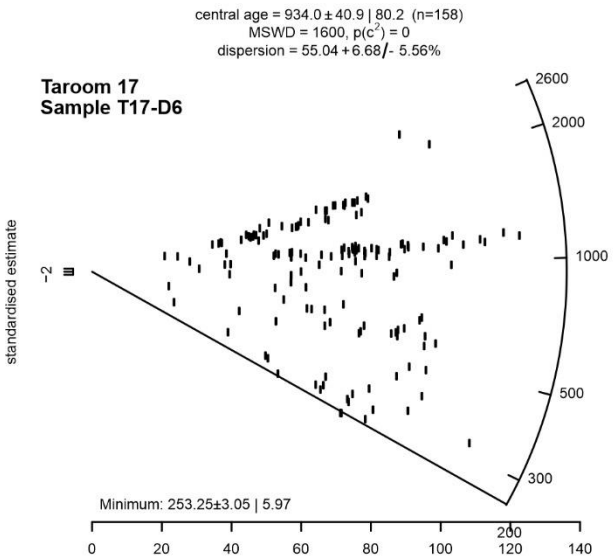
central age = 934.0 ± 40.9 | 80.2 (n=158)
MSWD = 1600, p(c²) = 0
dispersion = 55.04 + 6.68/- 5.56%
Taroom 17
Sample T17-D6
standardised estimate
Minimum: 253.25±3.05 | 5.97

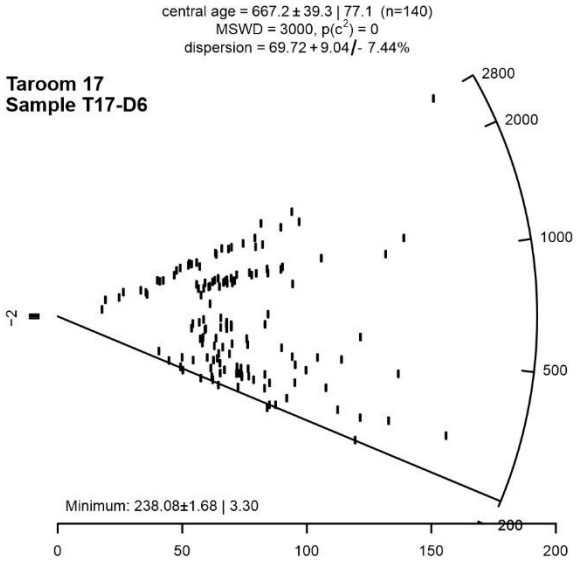
central age = 667.2 ± 39.3 | 77.1 (n=140)
MSWD = 3000, p(c²) = 0
dispersion = 69.72 + 9.04/- 7.44%
Taroom 17
Sample T17-D6
Minimum: 238.08±1.68 | 3.30

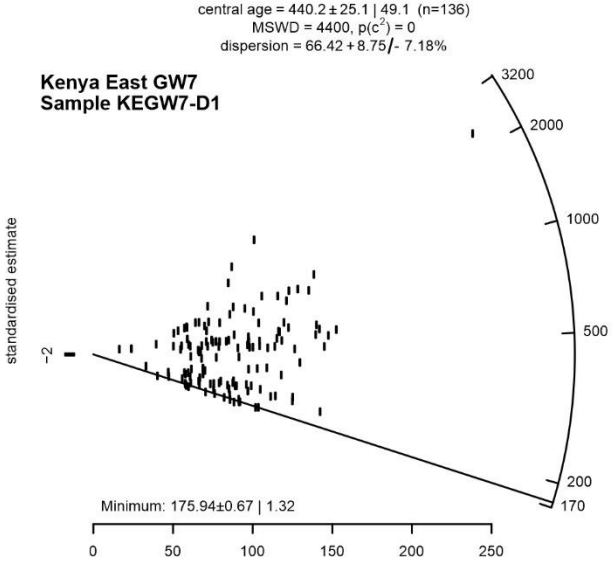
central age = 440.2 ± 25.1 | 49.1 (n=136)
MSWD = 4400, p(c²) = 0
dispersion = 66.42 + 8.75/- 7.18%
Kenya East GW7
Sample KEGW7-D1
standardised estimate
Minimum: 175.94±0.67 | 1.32

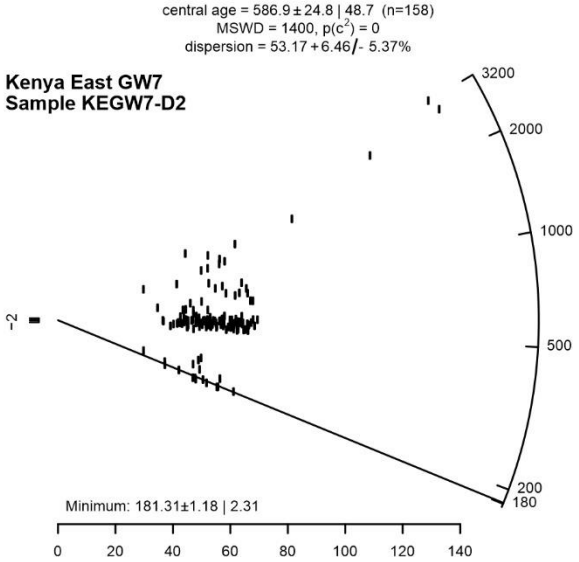
central age = 586.9 ± 24.8 | 48.7 (n=158)
MSWD = 1400, p(c²) = 0
dispersion = 53.17 + 6.46/- 5.37%
Kenya East GW7
Sample KEGW7-D2
Minimum: 181.31±1.18 | 2.31

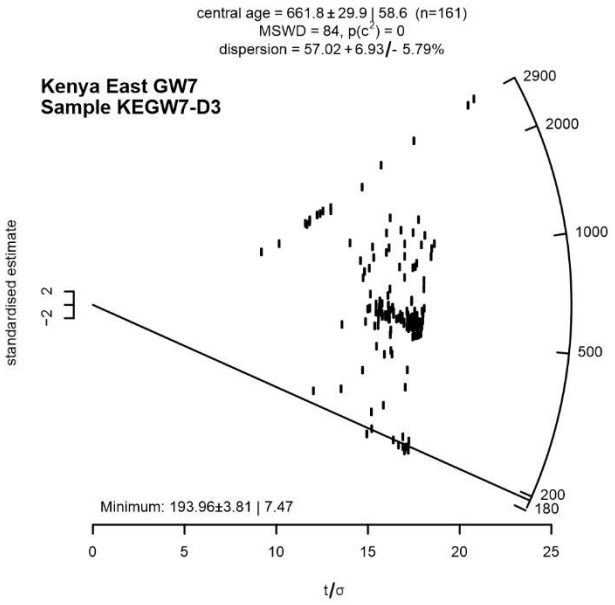
central age = 661.8 ± 29.9 | 58.6 (n=161)
MSWD = 84, p(c²) = 0
dispersion = 57.02 + 6.93/- 5.79%
Kenya East GW7
Sample KEGW7-D3
standardised estimate
Minimum: 193.96±3.81 | 7.47
t/σ

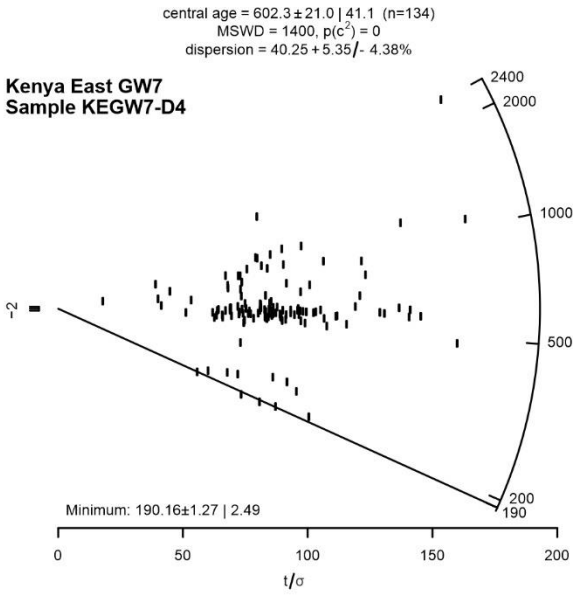
central age = 602.3 ± 21.0 | 41.1 (n=134)
MSWD = 1400, p(c²) = 0
dispersion = 40.25 + 5.35/- 4.38%
Kenya East GW7
Sample KEGW7-D4
Minimum: 190.16±1.27 | 2.49
t/σ

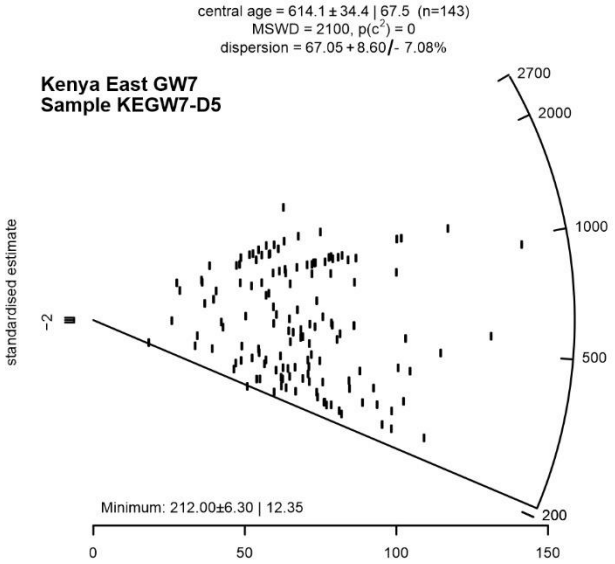
central age = 614.1 ± 34.4 | 67.5 (n=143)
MSWD = 2100, p(c²) = 0
dispersion = 67.05 + 8.60/- 7.08%
Kenya East GW7
Sample KEGW7-D5
standardised estimate
Minimum: 212.00±6.30 | 12.35

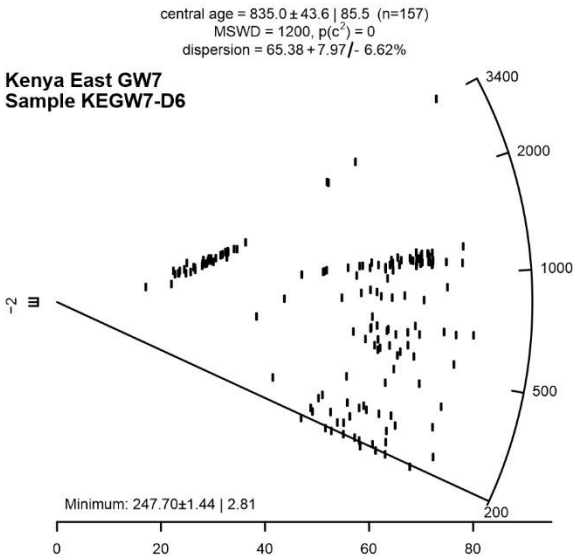
central age = 835.0 ± 43.6 | 85.5 (n=157)
MSWD = 1200, p(c²) = 0
dispersion = 65.38 + 7.97/- 6.62%
Kenya East GW7
Sample KEGW7-D6
Minimum: 247.70±1.44 | 2.81

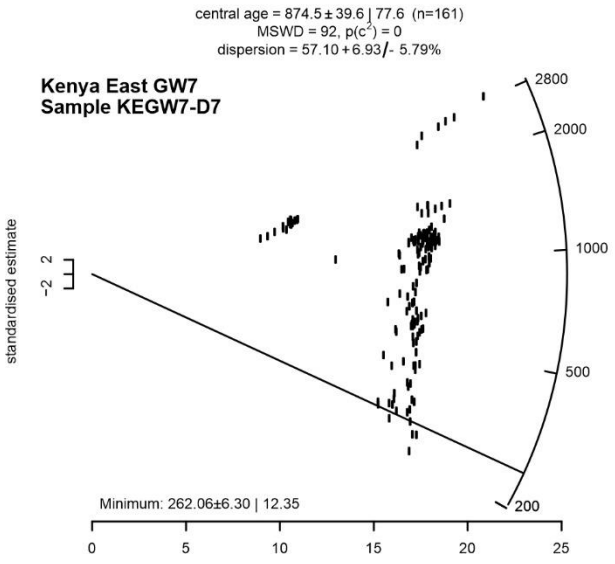
central age = 874.5 ± 39.6 | 77.6 (n=161)
MSWD = 92, p(c²) = 0
dispersion = 57.10 + 6.93/- 5.79%
Kenya East GW7
Sample KEGW7-D7
standardised estimate
Minimum: 262.06±6.30 | 12.35

Appendix F List of abbreviations

ANLEC R&D – Australian National Low Emissions Coal Research and Development

CAD – Cumulative age distribution

CA-TIMS – Chemical Abrasion Thermal Ionization Mass Spectrometry

CCS – Carbon Capture and Storage

CTSCo – Carbon Transport and Storage Company

FMI – Fullbore Formation Microimager

GSQ – Geological Survey of Queensland

KDE – Kernel density estimates

LA-ICP-MS – Laser Ablation Inductively Coupled Plasma Mass Spectrometry

LETA – Low Emission Technology Australia

Ma – Mega annum (million years)

MDS - Multidimensional Scaling plot

MFS – Maximum flooding surface

QFL – Quartz-feldspar-lithic

QUT-CARF – Queensland University of Technology, Central Analytical Research Facility

PDP – Probability density plot

SDAAP – Surat Deep Aquifer Appraisal Project

SEM-CL – Scanning electron microscopy with a cathodoluminescence detector

SHRIMP – Sensitive high-resolution ion microprobe

TS – Transgressive surface

UQ – University of Queensland

WM1 – West Moonie 1